



Natalia Ochocka-Lewicka

**Deciphering the diversity of glioma-infiltrating myeloid cells
with single-cell RNA and protein sequencing**

Ph.D. thesis completed at
the Laboratory of Molecular Neurobiology
of the Nencki Institute of Experimental Biology
Polish Academy of Sciences

SUPERVISOR:
Prof. dr hab. Bożena Kamińska-Kaczmarek

Warsaw 2021



This study was supported by following research grants:
NCN, OPUS 14 2017/27/B/NZ3/01605
NCN, PRELUDIUM 16 2018/31/N/NZ3/01696
FNP START 2021

Part of the work presented in this dissertation has been published in the following publications:

Ochocka N, Segit P, Walentynowicz KA, Wojnicki K, Cyranowski S, Swatler J, Mieczkowski J, Kaminska B. “Single-cell RNA sequencing reveals functional heterogeneity of glioma-associated brain macrophages” *Nature Communications* 12, 1151 (2021). <https://doi.org/10.1038/s41467-021-21407-w>

Ochocka N.; Kaminska B. “Microglia diversity in healthy and diseased brain: Insights from single-cell omics” *Int. J. Mol. Sci.* 22, 1–26 (2021). <https://doi.org/10.3390/ijms22063027>

Kaminska B.; **Ochocka N.**; Segit P “Single-cell omics in dissecting immune microenvironment of malignant gliomas – challenges and perspectives” *Cells* 10(9), 2264 (2021). <https://doi.org/10.3390/cells10092264>

I would like to express my thanks and appreciation to everyone who contributed to the research enclosed in the following dissertation

Prof. Bożena Kamińska-Kaczmarek for her supervision and support in the development of scientific ideas, and for creating a space to undertake new research directions that encourage me to grow into an independent researcher.

Jakub Mieczkowski, Ph.D. for his critical assessment of the applied statistical models and for directing the bioinformatical analysis of the first single-cell transcriptomic project that was performed entirely in Poland.

Paweł Segit for his tremendous contribution to the analysis of the tremendous amount of single-cell data.

Kamil Wojnicki for his enthusiasm and persistence in the optimization of the immunohistochemistry staining procedures.

Salvador Cyranowski and Julian Swatler for their contribution to the flow cytometric experiments.

Karol Jacek for his help with the analysis of the human datasets.

Bartosz Wojtaś, Bartłomiej Gielniewski and Paulina Szadkowska for performing sequencing of the CITE-seq libraries.

Beata Kaza for great management of all the technical issues that make the work go more smoothly, for being calm and helpful even during critical situations, and for handling orders at very short notice.

The whole team from Kaminska Lab

Laboratory of Cytometry, Nencki Institute of Experimental Biology, Warsaw for assistance in performing the flow cytometry and cell sorting procedures.

Genomics Core Facility, Centre of New Technologies, Warsaw for sequencing of the scRNA-seq libraries

Mamie oraz Tacie za wsparcie w nienaukowych obowiązkach, co okazało się bezcenne w osiągnięciu naukowych celów.

Pracę dedykuję mojemu Synowi w podziękowaniu za wszystkie przespane noce oraz Mężowi.

CONTENT

1. Summary	6
2. Streszczenie	7
3. Introduction	9
3.1. Overview of malignant gliomas	9
3.1.1. Classification and epidemiology	9
3.1.2. Molecular characterization of diffuse gliomas	10
3.2. The immune environment of malignant gliomas	13
3.2.1. Glioblastomas – immunologically “cold” tumors	13
3.2.2. The role of Glioma Associated Macrophages in supporting tumor growth	14
3.2.3. Dual origin of glioma-associated macrophages	15
3.2.4. Challenges in studying functions of microglia and macrophages in gliomas	16
3.3. Glioma immune microenvironment – Insights from single-cell studies	18
3.3.1. Heterogeneity of myeloid cells in gliomas	19
3.3.2. Cell identity vs localization and functional states	20
3.4. Sex-dependent view on malignant gliomas	23
3.4.1. Frequencies and therapeutic outcomes of malignant gliomas in males and females	23
3.4.2. Sex-related differences in immune responses	24
3.5. Overview of applied methodologies	25
3.5.1. Murine glioma model	25
3.5.5. Cell hashing procedure for sample multiplexing	30
4. Aims of the study	32
5. Materials and methods	33
5.1. Development of the GL261 tdT+ Luc+ GL261 murine glioma cell line	33
5.2. Animals	33
5.3. Implantation of the tdT+luc+ glioma cells to C57BL6 mice	33
5.4. Bioluminescent imaging of tumor growth	34
5.5. Tissue dissociation	34
5.6. Flow cytometry	35
5.7. Fluorescence activated sorting of CD11b ⁺ for scRNA-seq	35
5.8. Single-cell RNA sequencing	36
5.9. scRNA-seq data processing	37
5.10. Identification of myeloid cells in scRNA-seq	37

5.11. Identification of cell populations in scRNA-seq.....	38
5.12. Antibody-oligonucleotide tag conjugation for CITE-seq	39
5.13. Fluorescence activated sorting of CD11b ⁺ for CITE-seq	40
5.15. CITE-seq data processing	42
5.16. Analysis of the interferon-related gene signature	43
5.17. Analysis of GAM proportion in public human data sets.....	44
5.18. Immunohistochemistry on brain slices	44
5.19. Primary microglia and GL261 co-cultures.....	45
5.20. Quantitative gene expression analysis	45
5.21. Data visualization.....	46
6. Results	49
6.1. Kinetics of the tdT ⁺ Luc ⁺ GL261-implanted tumor growth	49
6.2. Optimization of dissociation and fluorescence-activated cell sorting procedures	49
6.3. Quality assessment of the scRNA-seq reads.....	51
6.4. Antibody-oligonucleotide conjugation	52
6.5. Quality assessment of the CITE-seq reads.....	53
6.6. Sample identification with the cell hashtag-oligo barcodes.....	55
6.7. Identification of immune cell types across the glioma-infiltrating myeloid cells with scRNA-seq	57
6.8. scRNA-seq expression profiles distinguish microglia and monocytes/macrophages	59
6.9. Tmem119 and Gal-3 separate microglia and monocyte/macrophages within the TME and show the distinct localization	62
6.10. Monocyte-To-Macrophage populations.....	63
6.11. Assessment of the previously proposed markers of glioma infiltrating monocytes/macrophages	65
6.12. Transcriptional networks expressed by GAMs are more pronounced in the infiltrating monocytes/macrophages	66
6.13. Verification of the myeloid cell populations in the glioma microenvironment with CITE-seq	69
6.14. The proportion of major GAM populations in different glioma stages	71
6.15. Separation of the major GAM populations by CITE-seq protein markers	72
6.16. Functional states of homeostatic and tumor-activated microglia.....	73
6.17. Functional states of macrophages in glioma TME.....	77
6.18. Monocyte-derived dendritic cells among CD11b ⁺ cells in glioma TME.....	79
6.19. Interferon-related vs tumor-supportive expression profiles.....	81
6.20. Sex differences in MHCII expression	83
6.21. MHCII and IFN-related signatures in male vs female.....	85
6.22. Sex-related differences in GAM proportions	87

7.	Discussion	90
7.1.	Dissecting the composition of myeloid infiltrates in glioma TME.....	90
7.2.	The unexpected heterogeneity of microglia in the healthy brain	91
7.3.	Myeloid cell heterogeneity in the glioma microenvironment	92
7.4.	Identification of subpopulations reflecting Monocyte-to-Macrophage transition	93
7.5.	Implications of the “interferon-related” gene expression	95
7.6.	The immunosuppressive role of differentiated macrophages	95
7.7.	Cell type versus cell state	96
7.8.	Sex differences in GAM responses	97
7.9.	Clinical implications of the myeloid cell diversity	99
8.	Summary and conclusions.....	101
	List of symbols and abbreviations.....	103
	References	110
	Supplementary figures.....	120
	Supplementary material.....	128

1. Summary

Malignant gliomas are highly lethal tumors of the central nervous system (CNS). The most common glioblastomas (GBM) are considered to be immunologically inert (“cold”) tumors, characterized by a highly immunosuppressive microenvironment and low potential for activation of the inflammatory and anti-tumor responses. Glioma-associated macrophages (GAMs) are myeloid cells accumulating in GBMs that comprise the major population of immune cells infiltrating gliomas. Multiple studies demonstrated that GAMs instigate tumor-induced immunosuppression, promote invasion, and support tumor growth.

Although the roles of GAMs in tumor progression have been widely investigated, the substantial heterogeneity of this population impeded its precise functional characterization. GAMs may originate from two cell lineages: specialized macrophages of the brain – microglia, and macrophages derived from the circulating monocytes that arrive at the tumor from the periphery – monocyte-derived macrophages (MDMs). Recent reports indicated that these two cell types can have different functions in glioma development, although studies on the specific roles were limited due to the lack of discriminating markers. Single-cell RNA sequencing (scRNA-seq) allows addressing the issue of cell heterogeneity, as it provides transcriptomic analysis of every single-cell in a mixture of thousands of different cells. Thus, information about diverse subpopulations is retained, in contrast to bulk methods where the gene expression is averaged over a total number of cells, and the information about the cell diversity is lost.

In this study, the myeloid (CD11b⁺) compartment of the glioma microenvironment was investigated with the scRNA-seq and Cellular Indexing of Transcriptomes and Epitopes by sequencing (CITE-seq). CITE-seq combines the scRNA-seq with a simultaneous protein profiling. Based on the single-cell expression profiles, novel markers for the separation of microglia and MDMs were identified and validated (*Tmem119* and *Gal-3*). Microglia and MDMs upregulated similar transcriptional networks in the glioma microenvironment. However, the response of MDMs was more pronounced. MDMs showed three monocyte-to-macrophage differentiation stages. The monocytic signature was associated with the highest expression of interferon-response genes, whereas differentiated macrophages upregulated factors involved in supporting tumor growth (e.g. *Trem2*, *Apoe*, *Cd9*, *Arg1* genes) and immunosuppression (PD-L1 protein, *IL18bp* and *Il1rn* genes). Additionally, this study demonstrated for the first time the sex-dependent differences in induction of MHCII complex and interferon-response genes in microglia and MDMs upon glioma-induced activation. An elevated level of MHCII in males and more pronounced upregulation of the interferon-response genes in females may constitute sex-dependent differences in incidence and outcomes of malignant gliomas found in humans.

2. Streszczenie

Glejaki złośliwe są guzami ośrodkowego układu nerwowego (OUN) powodującymi bardzo wysoką śmiertelność. Pomimo dużej liczby komórek układu odpornościowego gromadzących się w guzie, glejaki wykazują szereg mechanizmów tłumienia odpowiedzi przeciwnowotworowej i są powszechnie uznawane za immunologicznie „zimne” guzy. Makrofagi naciekające glejaki (*ang. Glioma Associated Macrophages - GAMs*) są komórkami mieloidalnymi, które stanowią najliczniejszą populację komórek odpornościowych gromadzących się w tych guzach. Wyniki wielu badań pokazały, że komórki te zamiast inicjować odpowiedź przeciwnowotworową, wspierają inwazyjność oraz uczestniczą w immunosupresji indukowanej przez guz przyczyniając się do wzrostu guza..

GAMs stanowią różnorodną populację komórkową, na którą składają się mikroglej oraz naciekające monocyty i makrofagi, co znacząco utrudnia funkcjonalną charakterystykę tych komórek. Mikroglej to wyspecjalizowane, rezydentne komórki mieloidalne zasiedlające mózg we wczesnej fazie rozwoju embrionalnego. Natomiast, makrofagi różnicują z monocytów (*ang. Monocyte-Derived Macrophages, MDMs*), napływających do guza z obwodu, a warunkach homeostazy występują w OUN w śladowej liczbie. Ostatnie badania wykazały, że te dwie populacje mogą pełnić odmienne funkcje w procesie wzrostu guza.

Sekwencjonowanie transkryptomu pojedynczej komórki (*ang. single-cell RNA sequencing – scRNA-seq*) pozwala dogłębnie zbadać różnorodność komórek w populacji GAMs, gdyż umożliwia analizę transkryptomu każdej pojedynczej komórki w mieszaninie tysięcy różnych komórek. Dzięki temu, informacja na temat poszczególnych subpopulacji zostaje zachowana, w przeciwieństwie do standardowych metod RNA-seq, w których profil ekspresji różnych komórek jest uśredniany, a informacja na temat różnic pomiędzy podgrupami komórek zostaje stracona.

W niniejszej pracy, komórki mieloidalne naciekające doświadczalne mysie glejaki zostały scharakteryzowane przy użyciu metody scRNA-seq. Dodatkowo, wykorzystana została metoda łącząca scRNA-seq z jednoczesnym oznaczeniem panelu białek powierzchniowych (*ang. Cellular Indexing of Transcriptomes and Epitopes by sequencing – CITE-seq*). Dzięki uzyskanym profilom ekspresji pojedynczych komórek, zidentyfikowane zostały nowe markery komórkowe (Tmem119 i Gal-3) pozwalające rozdzielić populację mikrogleju oraz pochodzące ze szpiku populacje MDMs. Wykazano, że mikroglej i MDMs aktywują ekspresję podobnych grup funkcjonalnych genów w mikrośrodowisku glejaka, jednakże w MDMs ekspresja indukowanych genów była silniejsza. Wśród populacji MDMs wykryto obecność subpopulacji o różnym stopniu zróżnicowania: monocyty, stadium przejściowe pomiędzy monocytami

i makrofagami oraz zróżnicowane makrofagi. Monocyty charakteryzowały się najwyższą ekspresją genów odpowiedzi na interferon (co sugeruje funkcje zapalne i przeciwnowotworowe), natomiast zróżnicowane makrofagi wykazały podwyższoną ekspresję czynników biorących udział we wspieraniu nowotworzenia (np. geny *Trem2*, *ApoE*, *Cd9*, *Arg1*) oraz immunosupresji (białko PD-L1 i geny *IL18bp*, *Il1rn*). Dodatkowo, wyniki niniejszej pracy po raz pierwszy wykazały zależne od płci różnice w poziomie kompleksu MHCII oraz ekspresji genów indukowanych przez interferon podczas aktywacji komórek mieloidalnych w mikrośrodowisku guza. Komórki męskie miały wyższy poziom kompleksu MHCII, natomiast komórki żeńskie wykazały zwiększoną ekspresję genów odpowiedzi na interferon. Stwierdzone różnice (potwierdzone także na materiale od pacjentów z glejakami) mogą mieć wpływ na obserwowane różnice w częstości występowania glejaków oraz w odpowiedzi na terapię pacjentów różnej płci.

3. Introduction

3.1. OVERVIEW OF MALIGNANT GLIOMAS

3.1.1. Classification and epidemiology

The primary brain tumors originate from the neural stem cells or progenitor cells of the central nervous system (CNS). Malignant tumors constitute one-third of all primary brain tumors and occur at the yearly incidence rate of 7 per 100 000¹. It translates to 1 in 160 people developing a malignant brain tumor in a lifetime (lifetime risk 0.62%)¹.

The most abundant type of malignant primary brain tumor is glioma accounting for 80% of malignant tumors (**Figure 3.1**). Gliomas encompass a broad category of diverse tumors originally classified based on their microscopic similarity to the precursor cells of glial lineages - the putative cells of glioma origin. The histopathological glioma classification relied on the morphological resemblance of the neoplastic cells to healthy brain cells, assigning tumors with astrocytic features as astrocytomas and of oligodendroglial features as oligodendrogliomas². The classification of CNS tumors by the World Health Organization (WHO) published in 2016, revised this approach and included molecular markers in addition to the histological characterization³. Based on the growth pattern and genotype diffuse gliomas have been grouped together and further defined with both histological and molecular characteristics. The diffuse gliomas are characterized by a highly infiltrative growth pattern resulting in the migration of neoplastic cells within the brain parenchyma. In adults, the diffuse gliomas

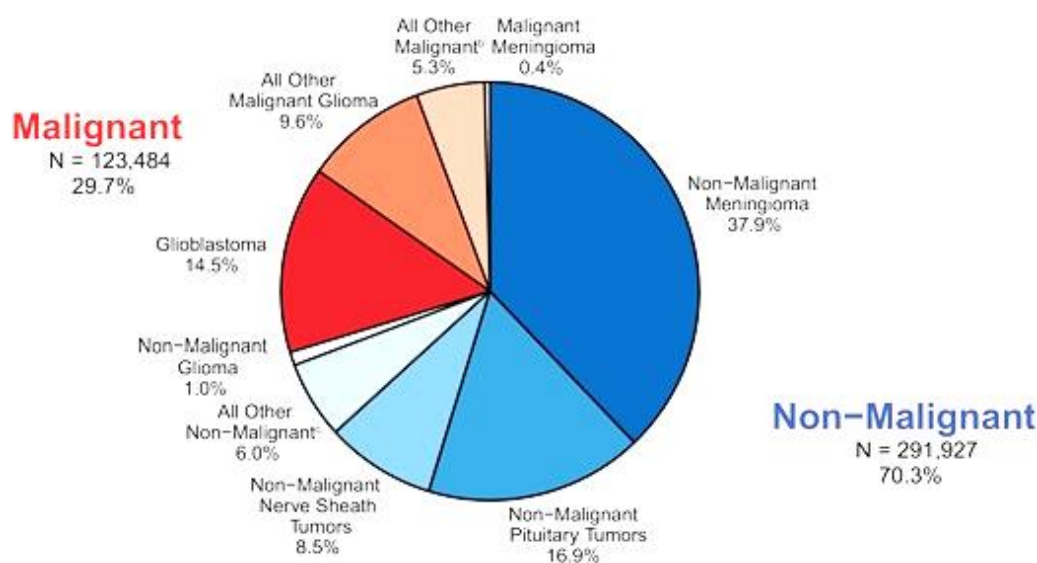


Figure 3.1. Distribution of primary brain and other CNS tumors. From CBTRUS Statistical report on 415 411 cases from the United States in years 2013-2017¹.

constitute 80% of all malignant gliomas and encompass WHO grade II and III oligodendrogliomas, grade II-III astrocytic tumors, and grade IV glioblastomas (GBM). The non-diffuse gliomas with more apparent tumor borders encompass pilocytic astrocytoma (grade I) and ependymoma (grade II) ³.

Despite decades of research, the therapeutic options for malignant gliomas are very limited, which is reflected by high mortality rates. The most aggressive type – GBM, which constitutes more than half of all gliomas, is primarily diagnosed at an older age (median of 65 years), and shows the worst median survival of 15 months ^{1,4}. WHO grade II and III gliomas are associated with better survival – 5-7 years in grade II, 2-3 years in grade III, and are more frequently diagnosed in younger patients (median 34 and 39 years, respectively) ^{1,5}. The therapeutic intervention is largely restricted to surgical resection and chemo-/radiotherapy. Multiple therapies have been tested in clinical studies, yielding a very limited improvement of patient outcomes ⁶.

3.1.2. Molecular characterization of diffuse gliomas

Diffuse gliomas are associated with substantial genetic heterogeneity that affects characteristics of the tumor and its microenvironment influencing responses to therapy and patient survival. As of 2016, the WHO glioma classification was largely redefined by the introduction of molecular parameters that provided additional factors for predicting clinical outcomes ³. The genomic context allows for a more precise definition of glioma subtypes as demonstrated in Figure 3.2 ⁷.

A key genetic alteration of the molecular classification of diffuse gliomas is the mutational status of genes encoding isocitrate dehydrogenases - *IDH1* and *IDH2*. IDH catalyzes the oxidative decarboxylation of isocitrate producing α -ketoglutarate (α -KG). The mutation occurs typically at codon 132 in *IDH1* (90% of cases) and codons 140 or 170 in *IDH2* ⁸. This nucleotide substitution results in arginine being replaced with histidine, leading to a gain-of-function, as the mutated enzyme reduces the α -KG to 2-hydroxyglutarate (2-HG) ⁸. The 2-HG accumulation exerts the inhibitory effect on histone and DNA demethylases, leading to a hypermethylation phenotype (G-CIMP – glioma CpG island methylator phenotype) and alterations of histone modifications that largely affects epigenetic and transcriptional pattern ^{9,10}. As a consequence, the *IDH1/2* mutation has a profound effect on clinical outcome, as it is associated with improved patient prognosis ^{11,12}. In addition, *IDH1/2* mutation is found in 70% of WHO grade II and III gliomas and only in 10% of GBMs (mostly recurrent GBMs) ^{8,13,14}. The IDH-mut gliomas are

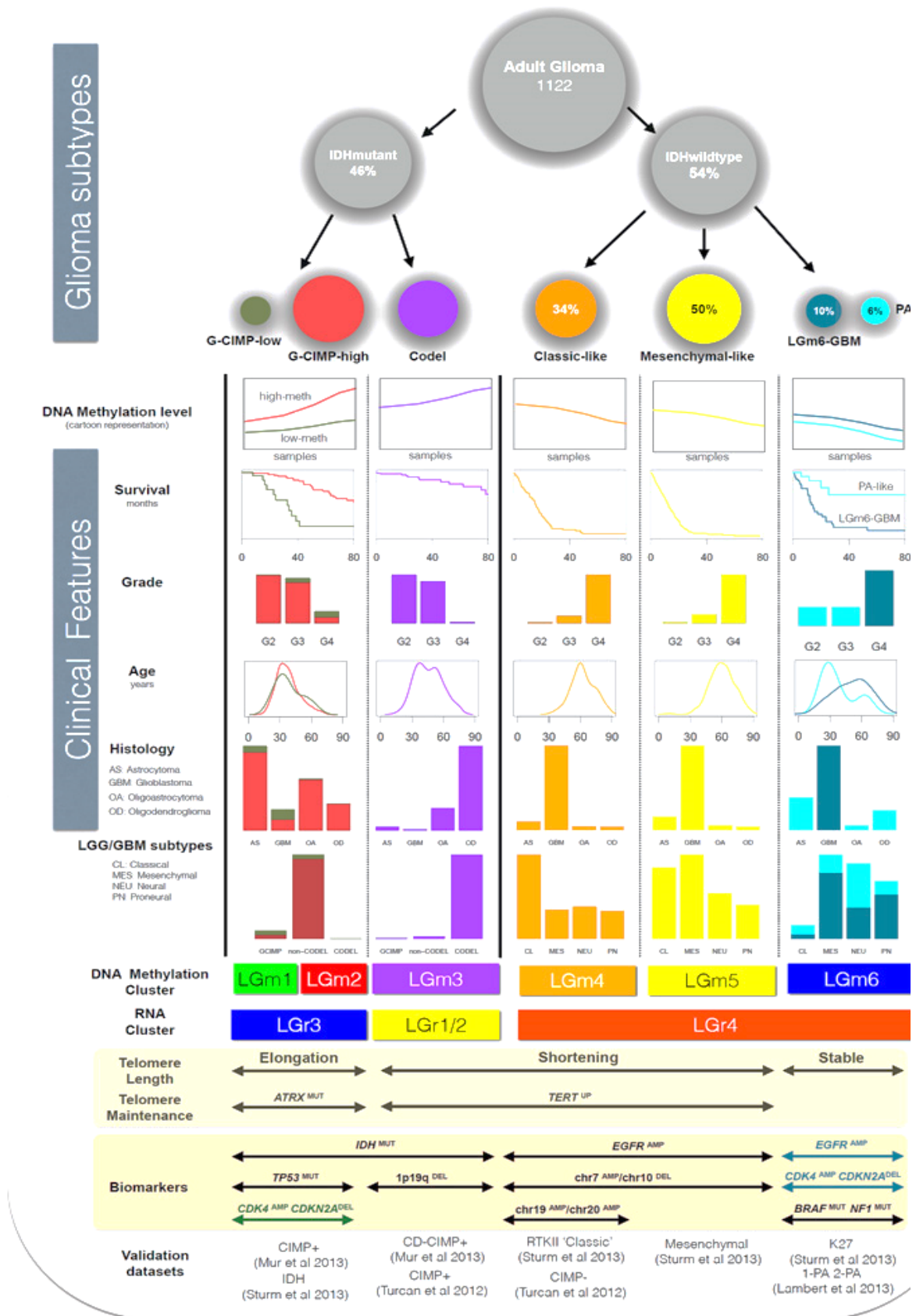


Figure 3.2 | Subtypes of adult diffuse glioma. Based on an integrative analysis of 1 122 adult gliomas. The size of the circles reflects the percentage of samples in each group. Figure from Ceccarelli et al. 2016 ⁷.

further divided into two groups: 1) exhibiting 1/19q co-deletion and the *TERT* promoter mutation, 2) harboring *ATRX* and *TP53* mutations; whereas cases with the combination of those two variants are very rare.

IDH wild type (IDH-wt) GBMs were found to express three major transcriptional profiles: classical, proneural, and mesenchymal^{15,16}. The classical subtype is associated with amplification of the *EGFR* gene (coding for Epithelial Growth Factor Receptor), which frequently co-occurs with the deletion of *CDKN2A* (coding for Cyclin Dependent Kinase Inhibitor 2a), and lacks *TP53* mutations. The proneural subtype exhibits a higher rate of *PDGFRA* amplification (encoding Platelet Derived Growth Factor Receptor Alpha) and increased frequency of *TP53* mutations as compared with other GBMs, which is associated with increased transcription of genes involved in oligodendrocyte (*PGGFRA*, *NKX-2*, *OLIG2*) and proneural development (*SOX*, *DCX*, *DLL3*, *ASCL1*, *TCF4*). The third, mesenchymal subtype is associated with deletion or mutation of *NFI* (encoding Neurofibromatosis 1) that frequently co-occurs with a *PTEN* mutation (encoding Phosphatase and Tensin Homolog) and exhibits increased expression of mesenchymal and astrocytic markers (*CHI3LI*, *CD44*, *MERTK*). This expression pattern might be reminiscent of epithelial-to-mesenchymal transition that has been associated with dedifferentiated tumors¹⁷. The three transcriptional GBM subtypes yield considerable differences in patient survival. The proneural type is associated with the best prognosis and the mesenchymal type with the worst prognosis, whereas the classical type shows the best response to aggressive therapy¹⁵.

Importantly, GBMs are not uniform, but are composed of cells exhibiting various molecular subtypes. Studies employing multiple sampling of distinct tumor regions and single-cell RNA sequencing (scRNA-seq) demonstrated that GBMs are rather formed by a mixture of neoplastic cells with a variable contribution of the three subtypes^{16,18,19}. Further analysis at the single-cell level pointed to the presence of four cellular states: neural-progenitor-like (NPC), oligodendrocyte-progenitor-like (OPC), astrocyte-like (AC), and mesenchymal-like (MES). Importantly, the defined states were consistent with previously defined molecular subtypes, as the NPC, OPC, AC, and MES states were associated with the following genetic alterations *CDK4*, *PDGFRA*, *EGFR*, and *NFI*, respectively^{16,18,19}.

The detailed classification of neoplastic cells demonstrated that each tumor exhibits a unique combination of cellular states. However, all tumors show recurrent signatures of the observed states. Therefore, it was suggested that GBM heterogeneity might be partially explained by the patterns of genetic alterations and the resulting cellular states^{16,18,19}.

3.2. THE IMMUNE ENVIRONMENT OF MALIGNANT GLIOMAS

3.2.1. Glioblastomas – immunologically “cold” tumors

Malignant gliomas are considered to be immunologically inert tumors characterized by a highly immunosuppressive microenvironment and low potential for activation of the inflammatory and anti-tumor responses. This is partly attributed to the CNS being an immune-privileged site and to the presence of the blood-brain barrier, which separates the CNS from the body. Still, gliomas are massively infiltrated by the immune system cells that can constitute up to 30 % of tumor mass²⁰. However, the immune population is dominated by myeloid cells, especially the brain-resident microglia, and monocytes/macrophages infiltrating from the periphery, whereas infiltration of activated T cells is rather low.

The immune escape of malignant gliomas has been found to result from several mechanisms. Tumor cells secrete factors recruiting and modulating the function of certain immune populations e.g. cytokine CCL2 that attracts monocytes, dendritic cells (DCs), natural killer (NK) cells, and T cells; cytokines CCL2/CCL22 that recruit regulatory T cells; transforming growth factor-beta (TGF- β) that blocks cytotoxic T lymphocytes; prostaglandin E2 (PGE2) that downregulates the production of inflammatory Th1 cytokines, upregulates Th2 immunosuppressive cytokines and inhibits anti-tumor activity of NK cells^{21,22}. NK cells are capable of killing malignant cells, which downregulate major histocompatibility complex (MHC) I and thus overcome cytotoxic T cell recognition. It has been found that NK cells can efficiently lyse cancer stem cells in GBMs. However, NK cells were also shown to contribute to the glioma stem cell differentiation, and the differentiated tumor cells show resistance to the NK-mediated cytotoxicity²³. In addition, eliciting adaptive immune response is blocked due to e.g. ineffective presentation of tumor antigens to T cells by antigen presentation cells (APC), accumulation of T regulatory cells that produce interleukins 10 and 35 (IL-10, IL-35) and TGF- β , which have an inhibitory effect on the response of the cytotoxic T lymphocytes²⁴. Additionally, the T cell infiltration to the brain is impeded by the T cells sequestration in the bone marrow²⁵. Whereas T cells that successfully migrated to the tumor mass are frequently hypo-responsive due to chronic antigen exposure, which is defined as T cell exhaustion. Exhausted T cells in GBMs upregulate many immune checkpoint proteins: programmed cell death protein 1 (PD-1), T cell immunoglobulin and mucin domain-containing 3 (TIM-3), lymphocyte-activation gene 3 (LAG-3), T cell immunoreceptor with Ig and ITIM domains (TIGIT), and CD39. Whereas the ability to produce proinflammatory factors e.g. interferon gamma (IFN- γ), interleukin 2 (IL-2), and tumor necrosis factor-alpha (TNF- α), is diminished²⁶.

The immune checkpoints are crucial elements of self-recognition, which are used by neoplastic cells to impede the recognition of tumor antigens and block T cell activation. Therefore, immunotherapy based on the immune checkpoint blockade (ICB) aims at blocking the interaction of tumor cells and immune checkpoints, facilitating the reactivation of tumor-specific immune responses. The ICB therapy improved patient outcomes in several cancer types, including brain metastases of melanomas and non-small lung cancer ^{27,28}. Regarding GBM, a series of recent clinical trials tested the efficacy of PD1 inhibitor (anti-PD1, Nivolumab) in monotherapy and combination with anti-angiogenic agent Bevacizumab (Check-Mate 143, NCT02017717), as well as in combination with radiotherapy (Check-Mate 498, NCT02617589) and both radio- and chemotherapy (Check-Mate 548, NCT02667587). The results were disappointing, as neither of the treatment schemes improved the median survival of GBM patients.

There is an ongoing discussion regarding the major factors impeding a successful reactivation of the anti-tumor immunity in malignant gliomas. Malignant gliomas exhibit broad interactions with the components of their microenvironment and the tumor progression heavily relies on the support of non-neoplastic cells. Unraveling the complexity of the immune microenvironment has been pointed as essential for improving our understanding of glioma pathobiology.

3.2.2. The role of Glioma Associated Macrophages in supporting tumor growth

The glioma microenvironment is rich in non-neoplastic cells including stromal, endothelial, and immune cells encompassing microglia, monocytes/macrophages, DCs, T cells, B cells, and NK cells. However, the glioma-associated microglia and macrophages (GAMs) constitute the most abundant population of immune cells in the glioma microenvironment²⁹.

Despite the high influx of the immune system cells to the tumor-bearing brain parenchyma, GAMs do not counteract tumorigenesis, but rather promote tumor invasion. Their accumulation increases with a tumor grade and high numbers of amoeboid, activated GAMs are associated with poor patient prognosis ³⁰. GAMs are recruited to the tumor niche and undergo tumor-directed education. As a result, GAMs contribute to tumor progression and evasion of the anti-tumor immune response via e.g. releasing immunosuppressive cytokines, inhibiting cytotoxic responses of NK cells, and blocking the activation of CD4⁺ T cells (reviewed in ³¹).

In the Laboratory of Molecular Neurobiology, it was previously shown that the glioma-derived factors drive the pro-tumorigenic transformation of microglia *in vitro* and that the reprogramming of myeloid cells (CD11b⁺/Iba1⁺) to the glioma-associated phenotype occurs in experimental rodent gliomas. GAMs fail to induce inflammatory signaling pathways³², exhibit suppressed anti-tumor immune responses³³, and promote proliferation and invasion of glioma cells^{34,35}. Summarizing, microglia and macrophages exhibit impeded anti-tumor responses and promote glioma growth and invasion.

3.2.3. *Dual origin of glioma-associated macrophages*

The GAMs term has been coined to collectively describe both microglia and macrophages that infiltrate gliomas. It reflects terminology used for peripheral macrophages where those cells are called tumor-associated macrophages - TAMs. Multiple studies have already shown that GAMs are not a uniform population and might consist of phenotypic subpopulations³⁶⁻³⁹.

Microglia are specialized CNS myeloid cells that originate from hematopoietic precursors - erythromyeloid progenitors (EMP) developing in an early embryonic life in the yolk sack⁴⁰. EMPs give rise to microglial progenitors that migrate to the brain starting from the embryonic day 9.5, until the formation of the blood-brain-barrier⁴¹. Microglia are long-living cells capable of self-renewal that is independent of bone marrow and circulating precursors^{40,42}. In contrast, GAMs of the monocytic lineage that infiltrate gliomas originate from circulating monocytes that renew continuously from the hematopoietic stem cells (HSC) residing in bone marrow^{43,44}. HSCs are capable of giving rise to all blood cell lineages such as red blood cells, lymphocytes, and myeloid cells like monocytes and macrophages⁴⁵.

Microglia and monocyte-derived macrophages (MDMs) exhibit high phenotypic-plasticity that might be shaped by the microenvironment. High adaptation potential was evidenced by the chromatin landscape reprogramming, which is induced for both bone marrow (BM) macrophage precursors and tissue-resident macrophages upon transplantation to the new environment. The BM-derived macrophage transplants acquired the majority of the enhancer histone modifications specific for tissue-resident macrophages⁴⁶. Moreover, Gosselin et al. (2017) showed that microglial transcriptional networks change in an environment-dependent manner and suggested that transcription regulatory elements are modulated by disease-associated microenvironmental perturbations⁴⁷.

Glioblastoma forms a highly influential microenvironment that profoundly alters the microglia/macrophage phenotypes. Thus, both brain resident microglia and infiltrating MDMs

found in the glioma microenvironment might undergo a phenotypic transformation that dominates over their origin. Until recently, insights into specific microglia and macrophage roles in glioma progression have been largely impeded by the lack of reliable markers that could specifically separate microglia and MDMs.

3.2.4. *Challenges in studying functions of microglia and macrophages in gliomas*

Many researchers attempted to elucidate the function of GAMs by isolating the GAM population from human and rodent gliomas and performing analyses of their transcriptomes. In those studies, CD11b⁺ cells were isolated by immunomagnetic beads or sorted by flow cytometry, as CD11b is a pan-marker of myeloid populations^{36,37,48-50}. We have recently analyzed all of those studies (including ours) and demonstrated a lack of consistency in the GAM transcriptomic signature across different laboratories, human samples, and animal models⁵⁰. We compared the gene expression profiles of GAMs derived from mouse^{36,50} and rat⁴⁸ gliomas, and patient-derived tumor samples^{37,49}. Those profiles showed remarkably low similarity, as only two genes – *Gpnmb* and *Tgm2*, (encoding Glycoprotein non-metastatic B and Transglutaminase 2, respectively) were identified in all investigated bulk-transcriptome studies. Moreover, the comparison did not yield consistent microglia phenotypes that could be classified according to the previously reported gene signatures – classical M1, alternative M2, and M2 a, b, c subtypes (reviewed in⁵¹).

The discrepancies in the field likely emerge from the diversity of cell populations cumulatively referred to as GAMs, and limited possibilities to reliably separate microglia and MDMs in the glioblastoma-bearing brains. The most commonly used strategy was Fluorescence Activated Cell Sorting (FACS) for CD11b⁺CD45^{low} (microglia) and CD11b⁺CD45^{high} (MDMs), which is based on the work on the irradiation bone marrow chimeras^{52,53}. However, CD11b is a pan-myeloid marker expressed in microglia, monocytes, macrophages (including CNS border associated macrophages), NK, and DCs. Thus, this strategy failed to reproduce the clear separation of subpopulations in cells sorted from human gliomas⁵⁴. Moreover, CD45 antigen was reported to efficiently separate microglia and MDMs only under homeostatic conditions. Once the two cell populations start to infiltrate the tumor, the expression of CD45 is upregulated by microglia impeding reliable separation⁵⁵.

Studies investigating microglia and MDMs ratio across glioma stages (based on CD11b⁺CD45^{high/low} gating) showed an increasing proportion of MDMs that constitute a sparse population at an early stage (1 week after tumor-induction) and greatly outnumber microglia at

nearly terminal stage (3.5 weeks)^{56,57}. Those findings are not conclusive since they relied on the CD45 gating. However, they point to differential roles of microglia and MDMs at subsequent glioma stages, which might be additionally associated with the gradual transformation of microglial cells to the CD45^{high} population.

One of the most reliable strategies for microglia and MDMs separation employs a lineage tracing relying on cell turnover differences of microglia and MDMs, in which administration of tamoxifen induces tdTomato expression in CX3CR1 (CX3C chemokine receptor 1) positive cells (all myeloid cells). This expression is lost by rapidly self-renewing macrophages, while long-lasting microglia remain TdTomato positive⁵⁸. Using this approach, Bowman et al. (2016) determined transcriptomic signatures that distinguish brain-resident microglia and bone-marrow-derived macrophages. Authors demonstrated differences in active chromatin regions and claimed distinct activation states of those cell populations⁵⁹. However, looking at the total number of genes in which differential expression was induced by the tumor (normal microglia vs all GAMs), a large fraction (over 1,000 genes) was common for microglia and MDMs. A substantially smaller number was found to be specific for microglia (around 100 genes) and MDMs (around 300 genes) suggesting the convergence of transcriptomic changes occurring in the glioma-infiltrating immune cells⁵⁹. The authors also proposed a CD49d (cluster of differentiation 49 d) as a discriminatory factor between microglia and MDMs, as CD49d was expressed exclusively by infiltrating macrophages⁵⁹. CD49d is an integrin subunit alpha 4 chain, which constitutes one of the chains of alpha 4 beta 1 (very late activating antigen-4 [VLA-4]) and alpha 4 beta 7 integrins. The finding was then reproduced on human clinical GBM samples⁶⁰.

Bennet et al. (2016) reported the microglia gene expression profile that provided several marker candidates for microglia under homeostatic conditions: *Tmem119*, *Fcrls*, *P2ry12*, *P2ry13*, *Gpr34*, *Gpr84*⁶¹, out of which expression of *Tmem119* was shown to be restricted to microglial cells also under pathological conditions such as Multiple Sclerosis⁶², brain injury and inflammation-induced activation⁶¹. However, its efficacy and specificity in the glioma environment remain to be further validated. Tmem119 (transmembrane protein 119) is a cell surface protein expressed by microglia cells in both mouse and human. However, there are some methodological limitations in using Tmem119 for immunophenotyping, since it is digested and destroyed by papain⁶³ – an enzyme used for gentle dissociation of brain tissue, which ensures high cell viability and isolation efficiency. Therefore Tmem119 might not be applicable in all experimental settings.

3.3. GLIOMA IMMUNE MICROENVIRONMENT – INSIGHTS FROM SINGLE-CELL STUDIES

The heterogeneity of the immune infiltrates and specific roles of distinct subpopulations could not be addressed with traditional methods. Therefore, the introduction of single-cell omics methods was a breakthrough that provided novel insights into the diversity of immune cells infiltrating gliomas.

Single-cell RNA sequencing (scRNA-seq) allows determining transcriptomic profiles of thousands of individual cells ⁶⁴. It relies on encapsulation of single cells together with reverse transcription reagents and unique cellular identifiers, enabling to add a cell-specific tag to each cDNA molecule that is synthesized based on an mRNA template. CyTOF (Cytometry by Time-Of-Flight) is a system for high-dimensional phenotypic analysis of single cells. It utilizes monoclonal antibodies conjugated with metal isotopes, which thanks to minimal overlap between channels allows evaluating over 40 parameters in a single run ⁶⁵. Thus, significantly outperforming classic flow cytometry analysis or multi-flow cytometry protocols. Cellular Indexing of Transcriptomes and Epitopes by Sequencing (CITE-seq) combines the two approaches to detect mRNA and surface proteins at the same time, by employing oligonucleotide-conjugated antibodies, of which the oligonucleotide tags are sequenced in parallel with transcriptome libraries, allowing simultaneous RNA and surface protein measurement ⁶⁶. This relatively new method has the advantage of comparing RNA expression with a protein level that are not always corresponding ⁶⁶, and gives a possibility to stain a virtually unlimited number of epitopes, although only surface proteins can be targeted.

While scRNA-seq, CITE-seq, and CyTOF techniques rely on bulk or immunosorted preparations of cells from the entire organ or tissues, the spatial information is lost. This obstacle might be overcome by emerging spatial transcriptomics techniques. Spatial transcriptomics allows associating the single-cell expression profile with spatial localization, in a quantitative manner on tissue sections ^{67,68}.

The single-cell omics studies are currently revising our knowledge on cell diversity and plasticity under various conditions. Since 2017, when the first scRNA-seq study addressing immune cells in gliomas was reported ³⁸, more than 30 single-cell studies demonstrating the diversity of myeloid cells in CNS were published (reviewed in ^{69,70}).

3.3.1. Heterogeneity of myeloid cells in gliomas

The first scRNA-seq analysis of myeloid cells in gliomas was carried out on IDH-mutant GBMs. The authors found a phenotypic spectrum ranging from microglia- to macrophage-like cells based on the gradual change in the expression of the previously established microglia and MDMs markers ³⁸. Another scRNA-seq profiling of CD11b⁺ cells from high-grade and low-grade gliomas has shown a similar continuum from microglia-high to MDM-high marker gene expression; however, the authors did not provide annotation of an IDH status in their analysis ³⁹. They identified tumor-activated microglia and putative monocytes/macrophages, and demonstrated distinct signatures using marker genes from murine glioma models ⁵⁹. The authors concluded that BM-derived GAMs upregulate immunosuppressive cytokines and markers of oxidative metabolism that are characteristic of the M2 phenotype ³⁹.

The *IDH* mutation status emerges as a potent modulator of the infiltration of immune cells in the glioma tumor microenvironment (TME). The IDH-mut gliomas show a lower accumulation of tumor-infiltrating lymphocytes and a lower level of the PD-L1 immune checkpoint protein ⁷¹. Friebel et al. (2020) used a mass cytometry analysis measuring 74 parameters to delineate the immune compartment of IDH-wt, IDH-mut gliomas, and brain metastases ⁷². The authors defined following subpopulations: microglia (P2RY12⁺), invading monocytes (CD11b⁺CCR2⁺), macrophages (CD11b⁺CD49d⁺), neutrophils (CD66b⁺CD16⁺), two subsets of classical dendritic cells (cDC1 - CD141⁺CADM1⁺ and cDC2 - CD1c⁺), T cells (CD3⁺), B cells (CD19⁺HLA-DR⁺), NK cells (CD56⁺CD16⁺), and plasma cells (CD19⁺CD38⁺). They showed that monocytes/macrophages constitute one-quarter of the myeloid immune infiltrate in the IDH-wt gliomas and one-half in the brain metastases, but in IDH-mut gliomas, the monocyte/macrophage population is minor ⁷². Additionally, the authors demonstrated that glioma infiltrating monocytes and macrophages show a gene expression trajectory consistent with a monocyte-to-macrophage (MDM) transition in the TME ⁷².

The differences in the proportion of resident microglia and invading MDMs may influence clinical outcomes. Stratification of GBM patients according to an MDM marker CD163 and microglial marker CX3CR1, demonstrated that the CD163 level negatively correlates with overall patient survival, whereas no correlation was found for the CX3CR1 level ⁷². Accordingly, the early scRNA-seq study on human gliomas indicated that the fraction of MDMs increases with tumor grade ³⁸ and the cell type identity score based on bulk RNA-seq data from The Cancer Genome Atlas (TCGA) demonstrated that microglia frequencies do not differ

between low-grade and high-grade gliomas³⁹. Altogether, the accumulating evidence suggests a diverse contribution of microglia and MDMs to glioma progression.

3.3.2. Cell identity vs localization and functional states

Several single-cell studies sampling various tumor areas showed consistently that MDMs tend to localize within the tumor core, whereas microglia reside mainly on the tumor edge and in the adjacent brain parenchyma^{59,72,73}. Müller et al. (2017) applied the identified transcriptomic signature of microglia and macrophage GAMs to estimate dominant populations across glioma anatomical regions in the dataset from the Ivy Glioblastoma Atlas Project⁷⁴. Analysis of the bulk RNA-seq performed on glioma microdissected regions indicated that microglia GAMs are enriched in the leading edge and adjacent white matter, whereas macrophage GAMs show increased accumulation in the regions of hyperplastic blood vessels, microvascular proliferation, and peri-necrosis³⁹. Consistently, scRNA-seq on human GBM samples resected from the tumor core and tumor periphery, revealed that MDMs (69%) predominate within the tumor core whereas microglia are most abundant at the tumor edge (86%)⁷⁵. Following on that, the transcriptional analysis of periphery- and core-derived samples demonstrated that GAMs in the periphery have enriched expression of pro-inflammatory interleukin *IL1B* and number of cytokines (*CCL2*, *CCL3*, *CCL4*, *TNF*), as well as colony-stimulating factor and its receptor (*CSF1*, *CSF1R*). Remarkably, the core-derived GAMs presented increased expression of the pro-angiogenic *VEGFA*, hypoxia-induced *HIF1A*, and anti-inflammatory interleukin *IL1RN*⁷⁵. Altogether, agglomerating evidence points to the importance of tumor proximity in the tumor-induced activation, but also show differences in transcriptional programs expressed by microglia and macrophages. Interestingly, immune-checkpoint encoding genes *CD274* (PD-L1), *PDCD1LG2* (PD-L2), *CD80* and *CD86* (CTLA4 receptors) were expressed in both regions, with the slightly higher level in the periphery that is indicative of the immunosuppressed microenvironment⁷⁵.

Sankowski et al. (2019) performed the functional analysis of microglial cells from human IDH-wt glioblastomas and age-matched controls with scRNA-seq and CyTOF⁷⁶. The cell clusters composed mainly of GBM-derived cells exhibited decreased expression of microglia core genes, and induced interferon-associated (*IFI27*, *IFITM3*), lipid metabolism-related (*LPL*, *APOE*, *TREM2*), and MHC-I and -II encoding genes (*HLA-A/B/C*, *HLA-DRB1*). Additionally, the authors identified cells showing high expression of genes associated with hypoxia (*HIF1A*, *VEGFA*). In their analysis, the authors identified only microglia and did not distinguished

monocytes and MDMs. However, the sample size was relatively low (n=1,701 microglial cells) that could impede a more detailed cell type identification and characterization of functional phenotypes. Nevertheless, using CyTOF the authors confirmed the glioma-induced expression of *HLA-DR*, *TREM2*, and *APOE* in microglia (P2RY12+TMEM119+) ⁷⁶. Another bulk transcriptomic analysis detected a type I IFN response in glioma MDMs (CD49d+) but not in microglia (CD49d-) ⁶⁰, pointing to the infiltrating GAM population as the major source of the interferon related genes.

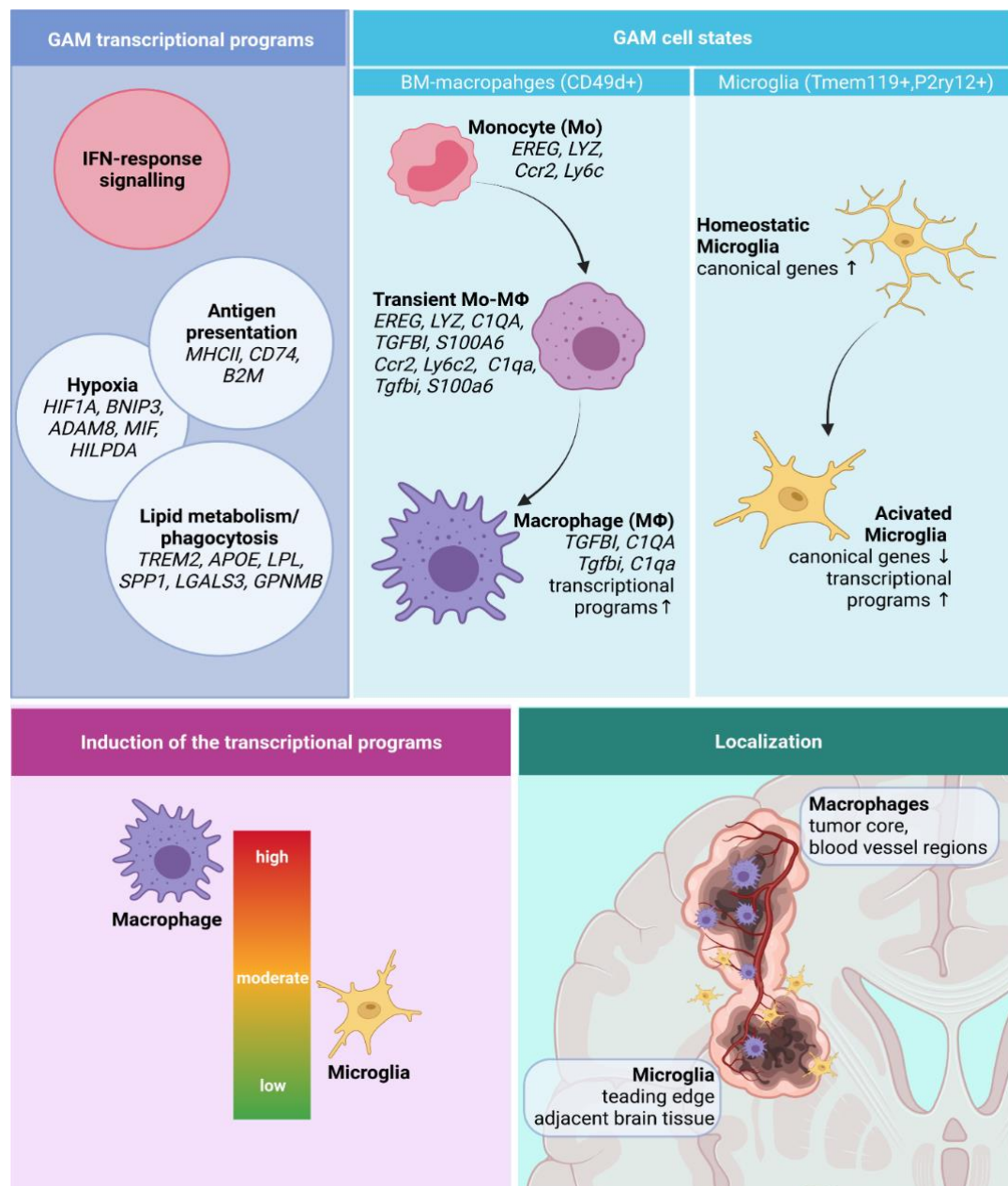


Figure 3.3 | Illustration summarizing functional states observed in microglia and MDMs in single-cell studies on murine and human malignant gliomas. From Kaminska, Ochocka and Segit (2021) ⁶⁹. Prepared with BioRender.com.

More detailed characterization of functional GAM phenotypes was provided in the recent scRNA-seq study on newly diagnosed (ND) and recurrent GBMs⁷⁷. In line with previous reports, the authors identified three major functional transcriptomic profiles: 1) **interferon-related** associated with increased expression of *STAT1*, *IFIT2*, *ISG15*, *CXCL10*, 2) **phagocytosis/lipid-related** showing enhanced expression of *GPNMB*, *LGALS3*, *FABP5*, *CD9* and 3) **hypoxic** characterized by induction of *BNIP3*, *ADAM8*, *MIF*, *HILPDA*. Those signatures were found in both ND and recurrent gliomas, as well as were recapitulated in a murine glioma model (C57BL6 mice injected with GL261 glioma cells). Importantly, the authors demonstrated that the identified transcriptomic signatures are differentially enriched in different cell clusters that may encompass different cell populations. The comparison of induced transcriptional profiles across microglia and MDMs, demonstrated that MDMs induce interferon and hypoxic signature at much higher levels. Amongst the infiltrating myeloid cells, the authors defined monocytes, transitory monocyte-macrophages, and several macrophage clusters enriched in specific transcriptional programs. Interestingly, in the murine glioma model the interferon-related genes *Rsad2* and *Cxcl10* showed also increased expression in monocytes and the transitory subpopulation, whereas hypoxic and lipid/phagocytosis-related signatures were enhanced only in macrophages⁷⁷. Interferon signaling is implicated in a response to pathogenic stimuli, known to elicit antiviral and immunoregulatory actions, and treatment with interferons has an anti-proliferative effect on tumor cells (reviewed in⁷⁸). In contrast, genes found in lipid/phagocytosis-related signature were found to play tumor-supportive roles. *TREM2* expression was shown to positively correlate with tumor progression, promote immunosuppression in the tumor microenvironment⁷⁹ and cooperate with CSF-1 in sustaining macrophage survival and proliferation⁸⁰. In turn, ApoE is the best-documented ligand of TREM2⁸¹. CD9 has been recognized as an anti-inflammatory marker of monocytes and MDMs⁸². Thus, the interferon and lipid/phagocytosis signatures may yield opposing activities.

Summarizing, the single-cell resolution studies of murine and human gliomas have shown a predominant MDMs accumulation and localization in the tumor core, monocyte-to-macrophage transition, a strong impact of MDM accumulation on patient's survival, and the expression of immunosuppressive factors by MDMs. Microglia rather decrease expression of their signature genes in human gliomas, show lower expression of the glioma-induced transcriptional patterns than MDMs, and being at the tumor invasive edge facilitate diffusive tumor growth in the brain parenchyma (**Figure 3.3**). Patient stratification based on the composition of the immune infiltrates may be informative in the selection of the

best immunotherapy approach. Further research is needed to determine whether a personalized therapy tailored to a specific composition of the immune TME may increase patient survival.

3.4. SEX-DEPENDENT VIEW ON MALIGNANT GLIOMAS

3.4.1. Frequencies and therapeutic outcomes of malignant gliomas in males and females

The sex of a patient is an important factor influencing brain tumors incidence rate, survival, and response to therapy ¹. Men show a higher incidence rate of the majority of malignant brain tumors, including glioblastoma (incidence ratio 1.6:1) (Figure 3.4), and show worse therapeutic outcomes from standard therapies than women ⁸³. Women more frequently develop a non-malignant meningioma (Figure 3.4) and female patients diagnosed with GBM show better survival as compared with men ^{1,84}.

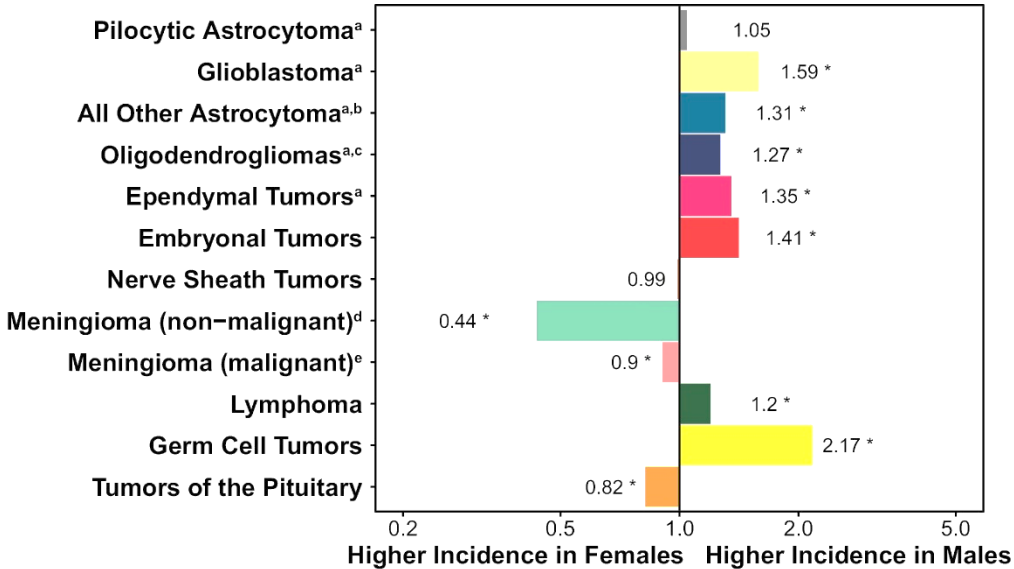


Figure 3.4 | Incidence Rate of selected primary CNS tumors regarding patient's sex (Males : Females). From CBTRUS statistical report from United States in 2013-2017 ¹.

Mechanisms underlying the sex dependence remain to be elucidated, however recent reports indicate that including sex in the molecular subtyping of GBMs could improve its classification ^{85,86}. As most gliomas occur in the advanced age, those differences might not necessarily depend on the effects of sex hormones. The analysis of molecular cell death profiles indicated that male GBM patients show higher volumes of necrosis and that the male high-necrosis group shows enrichment of *TP53* expression ⁸⁵. Whereas in females, the high-necrosis group is associated with worse survival and increased *MYC* ⁸⁵. Additionally, the loss of p53 was demonstrated to induce higher vulnerability for malignant transformation of male astrocytes ⁸⁶. Yang et al. (2019) analyzed therapeutic responses of male and female GBM

patients by comparing the therapeutic outcomes with transcriptional profiles⁸³. The transcriptional variation could be explained in 45% by the component common for both sexes. However, a large fraction (~35%) of the transcriptional variability appeared to be sex-specific. Importantly, the transcriptional patterns displayed a sex-dependent effect on survival, as the highest survival rate was achieved by women with down-regulated genes involved in integrin signaling, and men with diminished expression of cell-cycle genes⁸³.

The above-mentioned studies emphasize the importance of including sex in the analyses of glioma pathobiology and provide compelling evidence that combining the results from both sexes can conceal critical biological elements that govern tumor development and influence clinical outcomes in male and female glioma patients.

3.4.2. Sex-related differences in immune responses

The sex-specific outcomes of glioma patients may be linked to differences in the immune system function, as the efficacy of cancer immunotherapy differs between men and women, with men showing better therapeutic outcomes⁸⁷.

These differences may partially emerge from the interaction of the endocrine and immune systems, as sex hormones were shown to modulate immune responses. Women are found to elicit stronger immune responses and more frequently develop autoimmune diseases, compared with men^{88,89}. Immune cells, including macrophages and dendritic cells, express estrogen, and progesterone receptors. Depending on the context, estrogens may exert both inflammatory and immunosuppressive responses, whereas progesterone has broad anti-inflammatory properties (reviewed in⁹⁰). Androgens are also found to suppress the activity of immune cells, as testosterone diminishes the synthesis of a pro-inflammatory cytokine tumor necrosis factor-alpha (TNF α), inducible nitric oxide synthase (iNOS), as well as the production of nitric oxide by macrophages⁹¹. Men with androgen deficiency show increased levels of antibody titers and pro-inflammatory cytokines^{92,93}. Accordingly, the testosterone-reducing therapies result in a lower count of the blood T regulatory cells and an elevated number of NK cells⁹⁴.

Up to date, few studies that addressed the influence of sex on microglia functions revealed considerable sex-related differences. Male and female microglia were found to differ in overall frequency and fraction of amoeboid cells across specific brain areas^{95,96}. In addition, murine male microglia have higher expression of inflammation and antigen-presentation related genes, whereas female microglia show higher neuroprotective capacity^{95,97}. A bulk RNA-seq study combined with transplantation experiments demonstrated that the sex-specific transcriptomic

differences are tightly embedded and likely independent of sex hormones, as they were found to be retained upon cross-transplantation of microglial cells to the animal of the opposite sex ⁹⁷.

The influence of sex on glioma immunopathology remains largely unexplored, thus studies on microglia in both sexes are required to comprehend the importance of a sex-related variance. Ensuring proper representation of both sexes in further studies of microglial function in glioma development and progression may expand our understanding of the sex influence on glioma prevalence and responses to immunotherapy.

3.5. OVERVIEW OF APPLIED METHODOLOGIES

3.5.1. Murine glioma model

In this work a murine glioma model was employed, specifically, C57BL6 mice injected intracranially with GL261 murine glioma cells. The GL261 glioma cells have been developed from chemically induced tumors arising after intracranial administration of 3-methylcholantrene into C57BL/6 mouse, and subsequent series of subcutaneous and intracranial passages, leading to the development of *in vitro* cell cultures in the mid-1990s ^{98,99}. GL261 glioma cells have point mutations in *K-ras* (Kirsten rat sarcoma virus) gene and *p53* tumor suppressor gene, associated with *p53* upregulation and increased expression of *Myc* oncogene ^{99,100}. Human *TP53* is commonly deregulated in cancer, in GBMs the *TP53* aberrations are found in 36% of cases, among which point mutations associated with the *TP53* upregulation are most common ¹⁵. Overexpression of mutated *K-ras* along the mutated *Act* gene (encoding AKT kinase) in Nestin-positive cells was found to induce the formation of a tumor exhibiting the histological features of GBM in genetically engineered mouse models ¹⁰¹. Many GBMs show increased activity of the Ras (Rat sarcoma virus) protein family involved in signal transduction ¹⁰². The *K-ras* mutation has been recently described in gliomas, although its occurrence is not frequent ⁷.

GL261 grow rapidly in *in vitro* conditions and form highly aggressive, lethal tumors while transplanted intracranially. The tumors induced with $1-4 \cdot 10^5$ GL261 cells show 100% mortality rate within 21-25 days ^{99,103,104}, and are relatively resistant to radiotherapy ^{105,106}, although their growth pattern is not so diffusive as in most of the malignant gliomas ⁹⁹. A recent study provided a systematic comparison of the immune environment in human GBMs and several murine glioma models: (1) *K-ras/p53* mutant GL261, (2) *Pten* deficient CT2A, (3) *H-ras* and *Act* overexpressing a spontaneous tumor model 005, (4) Mut3 and (5) Mut4 generated by *NF1* and *p53* inactivation. Interestingly, the cell models harboring *NF1* mutation that is characteristic for

the most aggressive mesenchymal GBM subtype, failed to induce the tumor or showed slow tumor growth upon intracranial implantation. When human GBMs and murine models were compared, a high proportion of the immune infiltrates in human GBMs are antigen-presenting cells encompassing microglia, peripheral monocytes/macrophages, and DCs, which is also observed in GL261 tumors^{57,77}, although the frequency of DCs is higher in murine models¹⁰⁷. T-cell infiltration was found in all tumor types. However, GL261 had the highest rate of CD4⁺/8⁺ exhausted T-cells and a moderate level of CD4⁺ T regulatory cells compared with other types, pointing to high immunosuppression of the GL261 microenvironment¹⁰⁷.

A single-cell study investigating the glioma microenvironment demonstrated that immune cell populations identified in the human primary and recurrent GBMs are largely recapitulated by immune infiltrates of GL261 intracranial tumors. Both human GBMs and murine tumors are infiltrated by monocytes, microglia, macrophages, proliferating microglia, T cells, B cells, NK cells, and dendritic cells⁷⁷, although the proportions of contributing populations may differ. In addition, myeloid infiltrates were found to express several transcriptomic programs, that are represented in primary and recurrent GBMs, as well as in murine gliomas⁷⁷.

The immune cell composition may differ between malignant glioma patients, depending on the genomic context⁷⁰, administered treatments and patient characteristics such as sex, age, or life habits. Therefore, modeling the inter-patient variability might not be achievable in animal models. Still, GL261 tumors exhibit many characteristics of malignant gliomas and are capable of inducing infiltration of diverse immune cell populations, which to some extent, recapitulates the complex immune environment observed in GBMs. The results of the detailed analysis of glioma TME may improve our understanding of the heterogeneity and specialized functions of immune cells in gliomas.

3.5.2. *Single-cell RNA sequencing technology*

scRNA-seq allows transcriptomic analysis of every single cell in a mixture of thousands of different cells. Thus, information about diverse subpopulations is retained, in contrast to bulk RNA profiling methods in which gene expression is averaged over a total number of cells and information about the cell diversity is lost.

The first single-cell mRNA sequencing study came already in 2009 and was performed for four blastomere single cells¹⁰⁸. Soon after, a plate-based multiplexing solution was introduced that allowed assaying from tens to several thousand cells in a single experiment^{109,110}. In this approach, single cells were sorted onto 96-well plates and lysed to release mRNA that was then

indexed with a cell-specific barcode, before pooling for library preparation. This method provided great insight into the power of single-cell resolution. However, the number of cells that could be assayed was very limited and the procedure time-consuming. Improvement was brought by the introduction of the droplet-based encapsulation in a capillary system, which was demonstrated independently by two research groups^{111,112}. It allowed encapsulating single cells in nanoliter aqueous droplets, together with barcode indexes and reagents for reverse transcription, enabling fast processing of even thousands of individual cells. The droplet microfluidics was then commercialized¹¹³, making it available to a higher number of investigators. Currently, the end-to-end solutions are provided by many producers (10x Genomics, Bio-Rad, 1CellBio, BD, Mission Bio, Dolomite Bio, WaferGen, Genesis), and the number of cells that can be processed in a single run ranges from thousands to hundreds of thousands of cells (high-throughput Chromium X, 10x Genomics).

During one decade, the single-cell sequencing technology has been greatly expanded, from very few cells that were individually processed through library preparation steps, to multiplexed high-throughput solutions making the technique more and more widespread and accessible.

3.5.3. Droplet-based scRNA-seq system

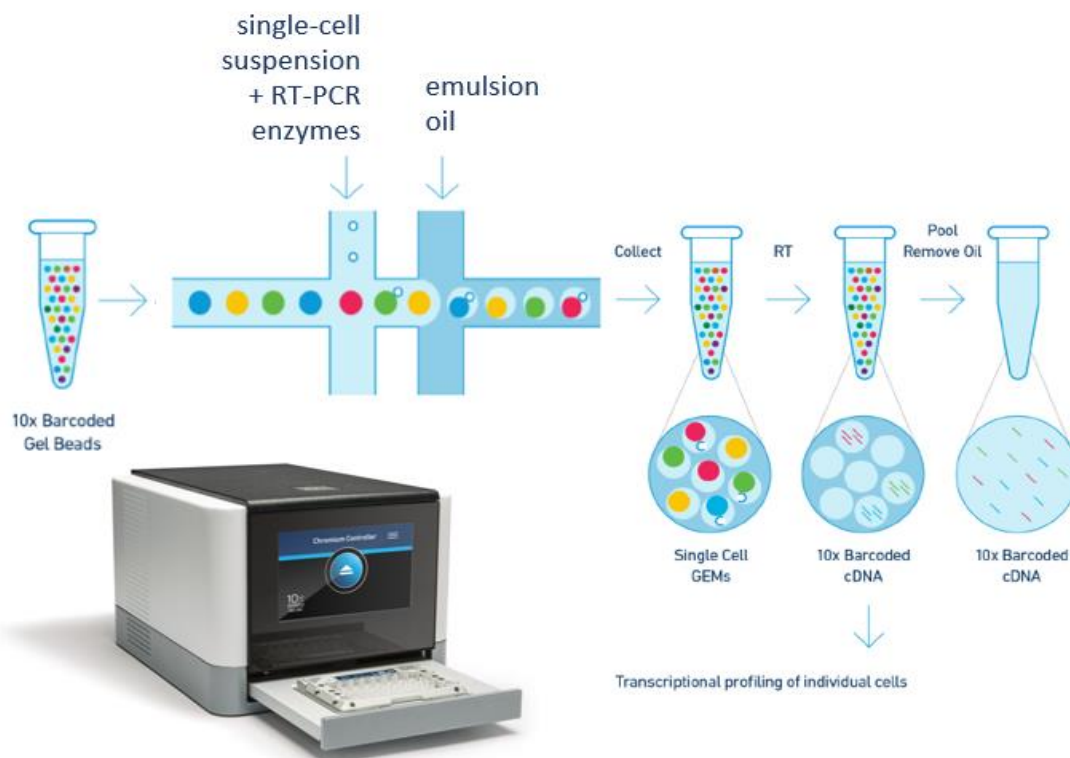


Figure 3.5 | Schematic workflow of the scRNA-seq with 10x Chromium (10x Genomics). Adapted from www.10xgenomics.com.

The droplet-based single-cell RNA sequencing technology employs a capillary system to encapsulate individual cells in water-phase droplets. A single cell is encapsulated together with a bead covered with a unique set of oligonucleotide indexes, cDNA synthesis enzymes, and cell lysing reagents forming a microcapsule referred to as a gel-bead in emulsion (GEM) (Figure 3.5).

Once encapsulation is finished, cells lyse releasing mRNA molecules and gel-beads dissolve unleashing the oligonucleotide indexes within the GEM interior. Next, mRNA molecules bind to the GEM-specific oligonucleotide indexes via poly-A tail and are reverse transcribed. To specifically analyze only polyadenylated mRNA molecules, and to circumvent capturing ribosomal RNAs, poly(T)-primers are typically used. The polyadenylated mRNA is next converted to complementary DNA (cDNA) by reverse transcriptase and tagged with unique molecular identifiers (UMIs) to mark unequivocally a single mRNA molecule and preserve information on cellular origin. The UMI tags will be used in a subsequent computational analysis to identify reads coming from the mRNA molecules of the same cell. Upon cDNA synthesis, the emulsion is broken down and all molecules from different cells are pooled together for further steps of library preparation, which are conducted similarly to the standard bulk RNA-seq protocols.

3.5.4. Simultaneous mRNA and surface protein assaying at the single-cell level

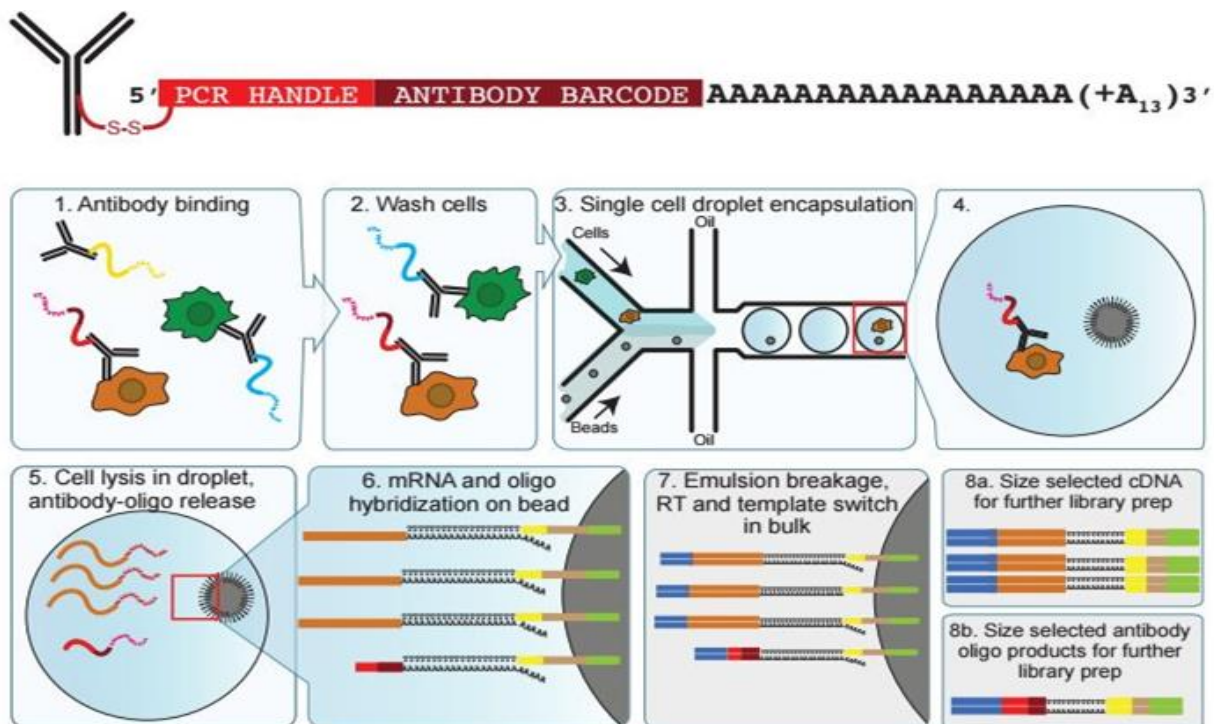


Figure 3.6 | CITE-seq procedure scheme. Illustration from Stoeckius et al (2017) ⁶⁶

Transcriptome sequencing at the single-cell level provides a great amount of information regarding a cell type and cell state, allowing the assessment of cellular diversity and the identification of specialized cell populations. Still, the mRNA level not necessarily corresponds to the protein level, which may hamper identification of e.g. cell type-specific surface protein markers. Simultaneous mRNA and surface protein assaying at the single-cell level expands the scRNA-seq method by employing the antibody-oligonucleotide conjugates (Ab-oligo). Cellular Indexing of Transcriptomes and Epitopes (CITE-seq)⁶⁶ and RNA expression and protein sequencing assay (REAP-seq)¹¹⁴ were developed in parallel and both employ cell staining with an antibody – similar as in the case of flow cytometry, but the CITE/REAP-seq antibodies carry oligonucleotide tags instead of fluorophores.

The Ab-oligos are composed of an antibody targeting the epitope of interest, conjugated with an oligonucleotide containing an antibody-specific barcode. Since the barcode is a 15-digit sequence, the CITE-seq method allows staining a virtually unlimited number of surface epitopes. The oligonucleotide barcodes from Ab-oligo conjugates are processed similarly to mRNA molecules, converting the protein detection into a sequenceable readout that can be quantified (**Figure 3.6**). First, cells are stained with Ab-oligos and then encapsulated with the capillary-based system. Following cell lysis, oligonucleotides from Ab-oligos bind to the complementary sequences of the cell-specific oligonucleotide index, which can be either based on the poly-A and poly-T hybridization as in the case of mRNA molecules or can employ dedicated hybridization sequences. Next, reverse transcription is performed, resulting in the generation of the oligo products that consist of an antibody-specific barcode and a cell-specific index. The oligo products are further amplified for library preparation. Since the libraries generated from Ab-oligos are shorter (155-180 bp) than libraries generated from mRNA molecules (400-450 bp), they can be easily separated with size selection using magnetic beads¹¹⁵. Libraries separation allows adjusting the concentration of samples loaded for sequencing and obtain optimal sequencing depth as the recommended range differs about 10-fold: $2\text{-}5 \times 10^3$ reads per cell for Ab-Oligo and $2\text{-}5 \times 10^4$ for mRNA library. Next, during a computational analysis, RNA readouts are paired with the Ab-oligo read-outs, thanks to the cell-specific indexes. Thus, both RNA and protein levels of the same targets can be assessed simultaneously in every single-cell.

3.5.5. Cell hashing procedure for sample multiplexing

An additional advantage of CITE-seq is the possibility to use the “hashtag” Ab-oligos for sample labeling ¹¹⁶. In this approach, Ab-oligos are made with antibodies targeting abundant epitopes that are expressed by all cell types. The hashing Ab-oligos employed in mouse and human studies typically consists of a mixture of antibodies e.g. anti-CD45 and anti-MHCI antibodies (mouse), and anti-CD298 and anti- β 2-microglobulin (human) (Biolegend., TotalSeq).

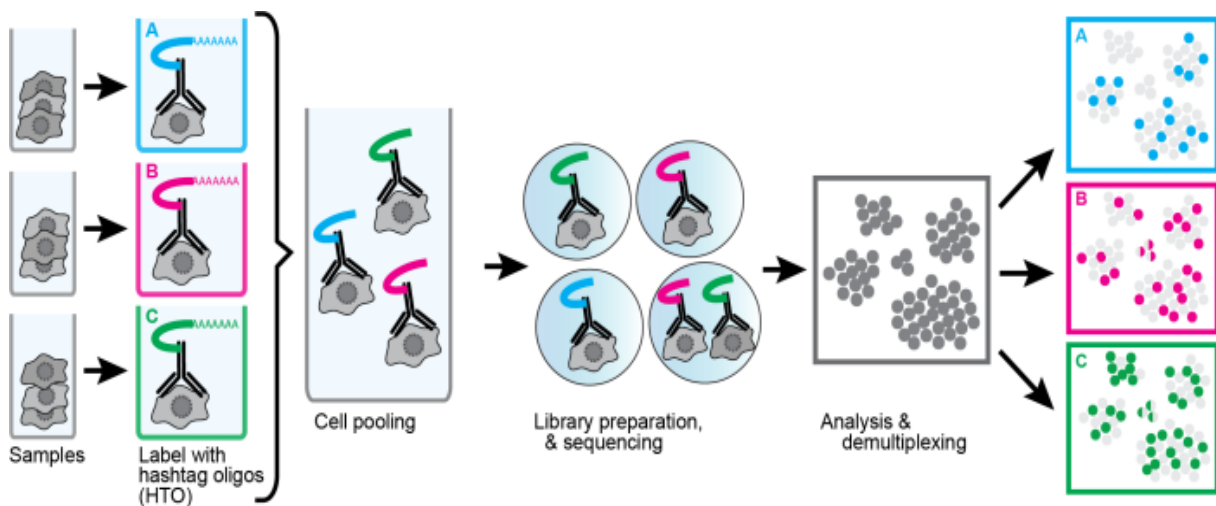


Figure 3.7 | Schematic representation of cell hashing procedure. Illustration from Stoeckius et al (2018) ¹¹⁶

Sample labeling with a hashing antibody allows multiplexing of several samples in one encapsulation well (**Figure 3.7**), which yields two major benefits. First, since multiple samples can be loaded into one well, the amount of reagents needed to conduct the scRNA-seq procedure decreases and thus significantly reduces the costs. Additionally, sample multiplexing favors increasing the number of replicates, since running e.g. 10 000 cells in one replicate vs 2 500 cells in four replicates generates approximately the same costs, but the latter provides much better statistical power and control over reproducibility and batch effects.

Second, the capillary-based single-cell encapsulation is not 100% efficient and results in the generation of multiple empty droplets – that can be easily identified and removed from the analysis, as well as droplets containing more than one cell – multiplets that are challenging to be identified with computational methods and can interfere with the analysis. The higher number of cells loaded onto a single well, the higher the multiplet rate. In cell hashing, droplets in which cells derived from two (or more) samples were encapsulated, result in the presence of two (or more) distinct hashing indexes. Therefore, the cell hashing procedure allows removing the vast majority of multiplets and improves data quality.

Summing up, the single-cell-based methods immensely advanced since the invention of scRNA-seq a decade ago. They can be applied with the end-to-end commercial systems allowing sequencing of thousands of individual cells in a single run and become more and more accessible to a wide number of investigators. Thus, studies on cellular heterogeneity might substantially improve our understanding of various biological processes.

4. Aims of the study

This study aimed to decipher the heterogeneity of myeloid cells in the microenvironment of the experimental murine gliomas, provide functional characteristics of a given cell type and identify surface protein markers for reliable separation of microglia and macrophages in the glioma microenvironment.

To address the issue of cellular heterogeneity, the study employed: 1) single-cell RNA sequencing (scRNA-seq) that allows transcriptomic profiling at a single cell level, and 2) Cellular Indexing of Transcriptomes and Epitopes by Sequencing (CITE-seq) that combines scRNA-seq with simultaneous assaying of cell-surface markers at protein level. All experiments were performed on a murine glioma model: C57BL6 mice implanted with GL261 cells.

The specific aims were as follows:

- 1) Implement scRNA-seq to reveal the heterogeneity of myeloid cells in the microenvironment experimental murine gliomas 14 days after implantation (the pre-symptomatic phase).
- 2) Provide functional characteristics of a given myeloid cell type infiltrating the glioma TME.
- 3) Validate main findings and discriminating markers by flow cytometry and immunofluorescence.
- 4) Search for potential sex differences in responses of myeloid cells in the glioma TME.
- 5) Implement CITE-seq to reveal the heterogeneity of myeloid cells in the glioma TME 14 and 21 days after implantation (at the pre-symptomatic and symptomatic phases).
- 6) Compare the heterogeneity and functional phenotypes of myeloid cells in the TME of experimental and human malignant gliomas.

5. Materials and methods

5.1. DEVELOPMENT OF THE GL261 tdT+ LUC+ GL261 MURINE GLIOMA CELL LINE

GL261 glioma cells were obtained from prof. Helmut Kettenman (MDC, Berlin, Germany). Cells were cultured in Dulbecco's Modified Eagle Medium (DMEM) supplemented with 10% fetal bovine serum (FBS, Gibco, MD, USA) and antibiotics (100 U/mL penicillin, 100 µg/mL streptomycin) in a humidified atmosphere of CO₂/air (5%/95%) at 37°C (Heraeus, Hanau, Germany).

In order to obtain a cell line allowing bioluminescent *in vivo* imaging, GL261 were stably transfected with pcDNA3.1(+)/Luc2=tdT plasmid (Addgene, Teddington, UK) carrying a fusion gene *luc2=tdT* that encodes Firefly Luciferase and tandem Tomato red fluorescent protein. The plasmid was first linearized by enzymatic digestion with NotI restriction enzyme (ThermoFisher). GL261 cells were seeded in the antibiotic-free medium in a density of $3 \cdot 10^5$ cells/well on a 12-well plate. After 24h incubation, a mixture containing 4ul of Lipofectamine2000 (ThermoFisher), 1.6 µg of the linearized plasmid or equivalent volume of Opti-Mem [SigmaAldrich] for mock transfection and Opti-Mem up to 200ul was prepared according to manufacturer's protocol. The mixture was added to the cells for 4h and then changed to the antibiotic-free medium. After 24 h the medium was changed to the one supplemented with 400 µg/ml G-418 Solution (Roche) until complete death of mock-transfected cells. Next, the tdT-positive cells were enriched twice with fluorescence activated cell sorting (FACS), expanded and cryopreserved in FBS with 10% dimethyl sulfoxide (Sigma-Aldrich).

5.2. ANIMALS

Male and female 10-week-old C57BL/6 mice were purchased from the Medical University of Bialystok, Poland. Animals were kept in individually ventilated cages, with free access to food and water, at the temperature of 21-23°C, 50-60% humidity, under a 12h/12h day and night cycle. All experimental procedures on animals were approved by the First Local Ethics Committee for Animal Experimentation in Warsaw (approval no 563/2018 and 764/2018).

5.3. IMPLANTATION OF THE tdT+LUC+ GLIOMA CELLS TO C57BL6 MICE

Mice (12-week old) were put under anesthesia with 2% isoflurane that was maintained during the entire procedure. Next, animals were injected with analgesic butorphanol (Butomidor) 0.03 mg/kg bodyweight and mounted in the stereotactic apparatus. Skin on the

head was incised and a whole was drilled at the following coordinates: +1 mm anterior-posterior (AP), -1.5 mm medial-lateral (ML), -3 mm dorsal-ventral (DV). Next, using a Hamilton syringe a single cell suspension of tdT⁺luc⁺ GL261 cells (80 000 cells in DMEM) were injected in the total volume of 1 μ l at the rate of 0.25 μ l/min to the right striatum. The syringe was withdrawn at the rate of 1 mm/min to prevent backward outflow of the cell suspension. Next, the incision was closed and an animal was monitored until full recovery from the anesthesia.

5.4. BIOLUMINESCENT IMAGING OF TUMOR GROWTH

Tumor growth was verified by assaying GL261-expressed luciferase activity with Xtreme *in vivo* bioluminescence imaging system (Bruker, Germany), at 7, 14 and 21 day post-implantation. Animals were injected intraperitoneally with 150 mg/kg body weight of D-Luciferin sodium salt (BC218, Synchem). Next, animals were put under anesthesia with 2% isoflurane and placed in the imaging apparatus. At the 10 min post D-Luciferin injection the bioluminescent signal was acquired for 2 minutes.

5.5. TISSUE DISSOCIATION

Naïve animals (controls), and mice 14 and 21 days post-implantation with a confirmed tumor presence were perfused transcardially with ice-cold phosphate-buffered saline (PBS), in order to remove blood cells from the brain. Next, brains were dissected and tumor-bearing hemispheres or whole brains of naïve animals were dissociated enzymatically. The dissociation was performed with the Neural Tissue Dissociation Kit with papain (Miltenyi Biotec) – for scRNA-seq preparations, or with 0.5 mg/ml DNase I (DN25, Sigma-Aldrich) in DMEM (Gibco, Germany) – for flow cytometry and CITE-seq preparations in order to preserve the Tmem119 epitopes. GentleMACS Octo Dissociator (Miltenyi Biotec) was used according to the producer's protocol. Following the enzymatic dissection, the resulting cell suspension was passed through a 70 μ m and 40 μ m strainer, washed with Hank's Balanced Salt Solution (HBSS) with calcium and magnesium (Gibco, Germany) and centrifuged at 300 g, 4 °C for 10 min. For myelin gradient removal, the pellet was suspended in 25 ml cold Percoll solution (18.9 mL gradient buffer containing 5.65 mM NaH₂PO₄H₂O, 20 mM Na₂HPO₄2(H₂O), 135 mM NaCl, 5 mM KCl, 10 mM glucose, 7.4 pH; 5.5 mL Percoll (GE Healthcare, Germany); 0.6 mL 1.5 M NaCl), overlaid with 5ml of cold PBS and centrifuged for 20 min at 950 g and 4 °C, without acceleration and brakes. Following centrifugation, the myelin layer was carefully removed from the interface of PBS layer and bottom layer and the remaining supernatant was removed. Cell pellet was suspended with Stain Buffer (BD Pharmingen), and cells counted with

an EVE™ Automatic Cell Counter (NanoEnTek Inc., USA) before further processing. In case of scRNA-seq experiment, cell suspension from two pooled tumor or control animals was split between for CD11b⁺ cell sorting for scRNA-seq and flow cytometry analyses, whereas for CITE-seq whole cell suspension from single animal (not pooled) was taken for CD11b⁺ cell sorting for CITE-seq.

5.6. FLOW CYTOMETRY

The staining procedure for flow cytometric analysis was performed directly after dissociation, samples were kept on ice avoiding prolonged light exposure. Cells were pelleted and suspended in 50 µl LiveDead Fixable Violet Dead Stain (ThermoFisher) or Fixable Viability Dye eF506 (eBioscience) (1:1000 in PBS) for 10 min. For the dead cell staining, a positive control was prepared by incubation of a cell suspension aliquot for 20 min at 56 °C. Next, the cells were washed with Stain Buffer (BD Pharmingen) and suspended in 50 µl of CD16/CD32 Fc Block™ (BD Pharmingen) diluted 1:250 in Stain Buffer and incubated for 10 min, to block FcγRIII/II and reduce unspecific antibody binding. Subsequently, 50 µl of antibody cocktail was added (see Table 5.1 for antibody specifications and dilutions). The flow cytometry procedures conducted in parallel with scRNA-seq experiments and for validation of scRNA-seq results were performed by Salvador Cyranowski, M.Sc. from the Laboratory of Molecular Neurobiology in cooperation with Julian Swatler, M.Sc. from the Laboratory of Cytometry, Nencki Institute, Warsaw.

5.7. FLUORESCENCE ACTIVATED SORTING OF CD11B⁺ FOR SCRNA-SEQ

Directly after dissociation, cells were pelleted (at 300 g, 4 °C for 10 min) and suspended in LiveDead Fixable Violet Dead Cell Stain (ThermoFisher) in PBS, in the density of $1 \cdot 10^6$ cells per 100 µl. After 10 min incubation at 4 °C, cells were washed twice with Stain Buffer (BD Pharmingen) and suspended in the anti-mouse CD16/CD32 Fc Block™ (BD Pharmingen), in the density of $1 \cdot 10^6$ cells per 100 µl, in order to block the unspecific antibody binding. Next, anti-mouse CD11b antibody (M1/70, BD Pharmingen) was added and cell suspension incubated for 20 min at 4 °C. Then, cells were washed twice with Stain Buffer and sorted with the dead cell exclusion to 20% FBS in PBS. For reagents dilutions and catalog numbers see Table 5.1. The cell sorting procedures were performed in the Laboratory of Flow Cytometry, Nencki Institute, Warsaw.

Table 5.1 | List of reagents and antibodies used for flow cytometric analysis and fluorescence activated cell sorting

Reagent	Manufacturer	Cat. number	Clone	Fluorophore	Dilution
LiveDead Fixable Violet Dead Cell Stain	ThermoFisher	L34955	-	-	1:1000
Fixable Viability Dye eF506	eBioscience	65-0866	-	-	1:1000
Stain Buffer	BD Pharmingen	554656	-	-	-
anti-mouse CD16/CD32 Fc Block	BD Pharmingen	553141	-	-	1:250
anti-CD45	BD Pharmingen	561868	30-F11	PE-Cy7	1:800
anti-CD11b	BD Pharmingen	557960	M1/70	Alexa Fluor 700 (flow cytometry)	1:800
anti-CD11b	BD Pharmingen	553310	M1/70	FITC (FACS)	1:800
anti-Ly6C	BD Pharmingen	560525	AL-21	PerCP-Cy5.5	1:100
anti-CD49d	BioLegend	103605	R1-2	FITC	1:400
anti-PD-L1	ThermoFisher	63-5982-82	MIH5	SuperBright600	1:100
anti-Tmem119	Abcam	ab210405	106-6	unconjugated (rabbit)	1:400
anti-rabbit Alexa Fluor 488 pAb	Abcam	ab150077	-	Alexa Fluor 488	1:1000
anti-Gal-3	eBioscience	125408	M3/38	Alexa Fluor 648	1:200 FC 1:100 IF

5.8. SINGLE-CELL RNA SEQUENCING

After sorting, viability and cell count was verified with an EVE™ Automatic Cell Counter (NanoEnTek Inc., USA). The cell suspension volume equivalent to 5000 target cells were used for further processing. Cell encapsulation and library preparation was performed with Chromium Controller (10x Genomics) and Single-Cell Gene Expression Kit v (10x Genomics) according to the producer's user guide (CG00052). The quality and quantity of generated libraries were verified with High-Sensitivity DNA Kit (Agilent Technologies, USA) on a 2100 Bioanalyzer (Agilent Technologies, USA). Sequencing was performed in the rapid run mode and the rapid run flow cell, paired-end (read 1 – 26 bp, read 2 – 100 bp) on a HiSeq 1500 (Illumina). The sequencing depth was targeted to $4 \cdot 10^4$ reads per cell. Sequencing of the scRNA-seq libraries was performed by Bartłomiej Gielniewski, Ph.D. and Bartosz Wojtaś, Ph.D. in the Laboratory of Molecular Neurobiology, Nencki Institute, Warsaw.

5.9. SCRNA-SEQ DATA PROCESSING

Raw sequencing data (BCL files) were demultiplexed and converted to FASTQ files using the Cell Ranger v3.0.1 (10x Genomics) (<https://support.10xgenomics.com/single-cell-gene-expression/software/pipelines/latest/installation>)^{113,117} and bcl2fastq v2.20.0.422 (Illumina). Sequencing results were mapped to a mouse genome GRCm38 (mm10) acquired from the 10x Genomics website and quantified using a Cell Ranger v.3.0.1^{113,117}. The total number of cells identified by the Cell Ranger was 41 059. The median number of detected genes per cell was 1,059, and the median unique molecular identifiers (UMIs) per cell was 2 178. Data analysis was performed in R using Seurat v3^{117,118}, within which data normalization, graph-based clustering, non-linear dimensionality reduction (UMAP/tSNE) and identification of cluster differentially expressed genes were performed. Unless otherwise specified in the description, all other quantitative parameters were fixed to default values. To filter out possible empty droplets, low-quality cells, and possible multiplets, cells with <200 or >3,000 transcripts were excluded from the analysis. Additionally, cells of poor quality, recognized as cells with >5% of their transcripts coming from mitochondrial genes, were excluded from the downstream analysis. After applying these filters, 40 401 cells were present in the data set. Gene expression measurements for each cell were normalized by the total number of transcripts in a cell, multiplied by a default scale factor, and the normalized values were log-transformed ("LogNormalize" method). Following the Seurat workflow, for each replicate the 2 000 most highly variable genes were identified using variance stabilizing transformation ("vst"). To facilitate identification of cell types these gene sets were expanded by adding genes described as having important roles in immune cells (see Supplementary Table 3) and genes involved in cell cycle regulation¹¹⁹. This extension did not influence our conclusions. The data processing was performed in collaboration with Paweł Segit, M.Sc. and Jakub Mieczkowski, Ph.D. from the Laboratory of Molecular Neurobiology, Nencki Institute, Warsaw.

5.10. IDENTIFICATION OF MYELOID CELLS IN SCRNA-SEQ

Having two biological replicates for each sex and condition (female control, female tumor, male control, male tumor), data from the corresponding samples were integrated using a Seurat v3 approach¹¹⁷. To avoid obtaining results fitted too closely to a particular data set and therefore possibly failing to fit to the additional data, firstly 2000 integration anchors (i.e., cells that are mutual nearest neighbors between replicates) were found. These anchors were then used as an input to the data sets integration procedure.

Integrated data were scaled, and unwanted sources of variation, namely a total number of counts per cell, the percentage of transcripts coming from mitochondrial genes per cell, and cell cycle effect were regressed out, as described in a corresponding vignette (https://satijalab.org/seurat/v3.0/cell_cycle_vignette.html). Data dimensionality reduction was performed using a principal component analysis (PCA), and the first 30 principal components were used in the downstream analyses. For each condition separately, the expression profiles were then clustered using an unsupervised, graph-based approach with the resolution parameter set to 0.3. Clustering results were visualized using two-dimensional t-Distributed Stochastic Neighbor Embedding (t-SNE) ¹²⁰. Based on expression of the reported/canonical markers, the clusters dominated by myeloid cells in four conditions were identified and further analyzed. The computational part of myeloid cells identification was performed in collaboration with Paweł Segit, M.Sc. and Jakub Mieczkowski, Ph.D. from the Laboratory of Molecular Neurobiology, Nencki Institute, Warsaw.

5.11. IDENTIFICATION OF CELL POPULATIONS IN SCRNA-SEQ

Myeloid cells identified in each condition separately (see above) were extracted and merged. For the merged data set, a new set of the 2,000 most highly variable genes was identified using variance stabilizing transformation ("vst"), and this set was further expanded by adding the genes involved in cell cycle regulation. Computation of expression estimations, regression of the unwanted variation, and data dimensionality reduction were performed as described above. Next, the expression profiles were clustered using the same approach as above, but with a resolution parameter set to 0.6. After clustering, data were visualized using two-dimensional Uniform Manifold Approximation and Projection (UMAP) ¹²¹. Based on expression of reported/canonical markers of myeloid cells, clusters with cells of interest (microglia, macrophages, and BAMs) were identified.

Differentially upregulated genes (signature genes) were found for each class of interest. Significantly upregulated genes between compared groups were found using a Wilcoxon Rank Sum test implemented in Seurat v3 (min.pct = 0.25, only.pos = TRUE). These genes were subsequently used for the functional analysis and characterization of the identified clusters. Gene Ontology analysis was performed using the clusterProfiler v3.12.0 package ¹²². This part was performed in cooperation with Paweł Segit, M.Sc. and Jakub Mieczkowski, Ph.D. from the Laboratory of Molecular Neurobiology, Nencki Institute, Warsaw.

5.12. ANTIBODY-OLIGONUCLEOTIDE TAG CONJUGATION FOR CITE-SEQ

The oligonucleotide tags were designed according to the 10x Chromium guidelines, in a way to be compatible with the v3 and v3.1 10x chemistry (**Figure 5.1**). Briefly, the oligonucleotide sequence consisted of: Capture Sequence 1 - sequence complementary to the capture sequence on the Gel Bead; Feature Barcode - an antibody-specific tag allowing for the feature identification; TruSeq Read 2 - a primer site for library amplification. The unique Feature Barcode sequences were selected from the Barcode Whitelist Rev A CG000193¹²³, in order to exclude a possibility of the barcode overlap with the existing barcode sequences utilized in the 10x and TotalSeq reagents. Full oligonucleotide tags sequences are shown in Table 5.2.

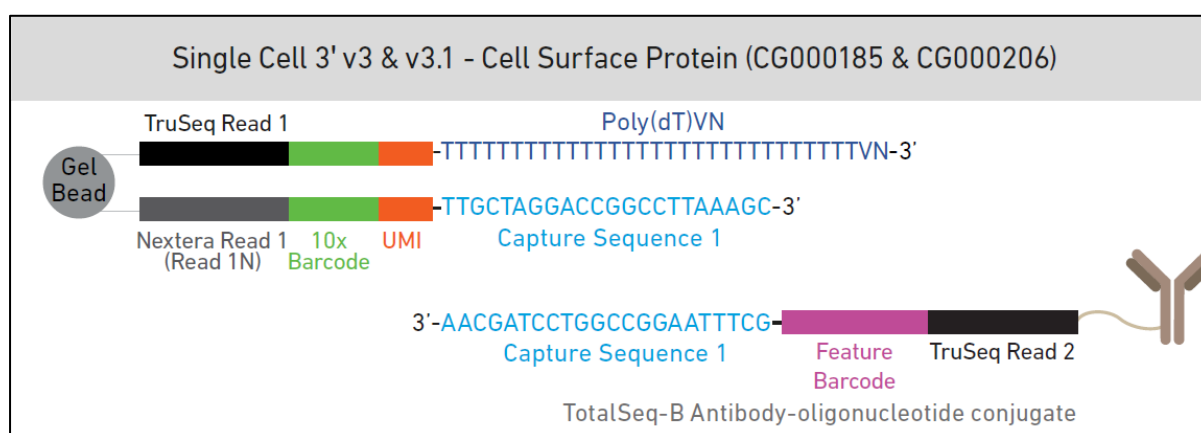


Figure 5.1 | Schematic representation of the antibody-oligonucleotide conjugate capture. Adapted from the CG000149 Rev B demonstrated 10x protocol¹²⁴.

A list of antibodies used for conjugation is given in Table 5.3. The recommended antibody amount for conjugation is 100 μ g in a concentration of 1 mg/ml. Thus, anti-CD74 antibody was condensed to the recommended concentration with the Antibody Concentration Kit ab102778 (Abcam) before conjugation. The antibody and oligonucleotide conjugation was performed with the Oligonucleotide Conjugation Kit ab218260 (Abcam) according to the producer's protocol. Briefly, 100 μ M of an oligonucleotide diluted in 100 μ l of Wash Buffer was activated with Oligonucleotide Activation Reagent for 30 min at RT. Simultaneously, 100 μ l of an antibody at 1 mg/ml concentration was activated with an Antibody Activation Reagent for 30 min at RT. Next, the activation reagents were removed with desalting columns, and antibody and oligonucleotide eluents were mixed in a ratio of 1:3, 1:5, or 1:10 and incubated for 1 h at RT. The conjugates were then purified using Conjugate Clean Up reagent that was added to the conjugates in an equal volume, incubated for 20 min at RT, and centrifuged for 5 min at 15,000g and RT. Next, the supernatant was removed carefully, and the conjugate pellet was suspended

in the Antibody Suspension Buffer supplemented with 0.02% sodium azide to a final concentration of 1 mg/ml. The conjugation efficiency was verified with SDS-PAGE on 4-12% gradient gel, and the conjugate solutions were stored at 4 °C.

Table 5.2 | Sequences of the oligonucleotide tags. The Feature Barcode sequence is given in bold. AmMC12 indicates an amine group at the C12 of the 5' end.

oligo1	5' AmMC12/GTGACTGGAGTTCAGACGTGTGCTCTTCCGATCTNNNNNNNNNN AAGGCAGACGGTGC ANNNNNNNNNGCTTTAAGGCCGGTCCTAGCAA 3'
oligo2	5' AmMC12/GTGACTGGAGTTCAGACGTGTGCTCTTCCGATCTNNNNNNNNNN GGCTGCGCACCGCCT NNNNNNNNNGCTTTAAGGCCGGTCCTAGCAA 3'
oligo3	5' AmMC12/GTGACTGGAGTTCAGACGTGTGCTCTTCCGATCTNNNNNNNNNN TAGTTGACATGCCA TNNNNNNNNNGCTTTAAGGCCGGTCCTAGCAA 3'

Table 5.3 | List of antibodies used for conjugation.

Name	Concentration	Cat. No	Clone	Lot	Producer
Anti-Tmem119	1 mg/ml	ab220249	106-6	GR3264318-2	Abcam
Anti-CD74	0.5 mg/ml	151002	In-1	B297738	Biolegend
Anti-CD52	1 mg/ml	D204-5	BTG-2G	062	MBL

5.13. FLUORESCENCE ACTIVATED SORTING OF CD11b⁺ FOR CITE-SEQ

Directly after dissociation, the volume of cell suspension equivalent to 1 x 10⁶ cells was centrifuged at 300 g, 4 °C for 10 min and the pellet was suspended in LiveDead Fixable Violet Dead Cell Stain (ThermoFisher) 1:1000 in PBS, in the density of 1 x 10⁶ cells per 100 µl. After 10 min incubation at 4 °C, cells were washed twice with Stain Buffer (BD Pharmingen) and suspended in 50 µl of anti-mouse CD16/CD32 Fc Block™ (BD Pharmingen) 1:250, in order to block the unspecific antibody binding. During incubation, the antibody cocktail containing marker panel and cell hashing Ab-oligo conjugates was prepared. Briefly, proper amounts of marker panel Ab-oligos were mixed (**Table 4.3**), filled with Stain Buffer up to 52.5 µl x the number of samples, and aliquoted for each CITE-seq sample. Next, a sample-specific cell hashing Ab-oligo (**Table 4.4**) was added, and antibody cocktails were centrifuged at 14,000g, 4°C for 10 min. Next, supernatants from each Ab-oligo cocktail mix and anti-mouse CD11b antibody (M1/70, BD Pharmingen) were added to the appropriate cell suspension sample and incubated for 20 min at 4 °C. Cells were washed twice with Stain Buffer and sorted with the dead cell exclusion to 20% FBS in PBS. The sorting was stopped after obtaining 50,000 cells per sample. The cell sorting procedures were performed in the Laboratory of Flow Cytometry, Nencki Institute, Warsaw.

Table 5.4 | List of antibody-oligo conjugates included in the protein panel for CITE-seq

Name	Producer	Cat. No	Clone	Lot	Barcode	Conjugation
Anti-Tmem119	Abcam	ab220249	106-6	GR3264 318-2	GGCTGCGC ACCGCCT	in-house
Anti-CD74	Biolegend	151002	In-1	B297738	AAGGCAG ACGGTGCA	in-house
Anti-CD52	MBL	D204-5	BTG- 2G	062	TAGTTGAC ATGCCAT	in-house
TotalSeq™-B0014 Anti-CD11b	Biolegend	101273	M1/70	B300518	TGAAGGCT CATTGT	commercial
TotalSeq™-B0096 Anti-CD45	Biolegend	103161	30-F11	B294506	TGGCTATG GAGCAGA	commercial
TotalSeq™-B0013 Anti-Ly-6C	Biolegend	128053	HK1.4	B302523	AAGTCGTG AGGCATG	commercial
TotalSeq™-B0116 Anti-Gr-1	Biolegend	108465	RB6- 8C5	B305364	TAGTGTAT GGACACG	commercial
TotalSeq™-B0190 Anti-CD274 (PD-L1)	Biolegend	153608	MIH6	B307175	TCGATTCC ACCAACT	commercial
TotalSeq™-B0078 Anti- CD49d	Biolegend	103631	R1-2	B305995	CGCTTGGA CGCTTAA	commercial
TotalSeq™-B0117 Anti-I-A/I-E (MHCII)	Biolegend	107657	M5/11 4.15.2	B305131	GGTCACCA GTATGAT	commercial

Table 5.5| List of cell hashing antibodies used in CITE-seq

Name	Clone/ producer	Lot number	Barcode	Sample stained
TotalSeq™-B0301 anti- mouse Hashtag 1 Antibody	M1/42; 30-F11/ Biolegend	B306476	ACCCACCAGTAAGAC	Day 0, female
TotalSeq™-B0302 anti- mouse Hashtag 2 Antibody	M1/42; 30-F11/ Biolegend	B306447	GGTCGAGAGCATTCA	Day 0, male
TotalSeq™-B0303 anti- mouse Hashtag 3 Antibody	M1/42; 30-F11/ Biolegend	B306444	CTTGCCGCATGTCAT	Day 14, female
TotalSeq™-B0304 anti- mouse Hashtag 4 Antibody	M1/42; 30-F11/ Biolegend	B308313	AAAGCATTCTTCACG	Day 14, male
TotalSeq™-B0305 anti- mouse Hashtag 5 Antibody	M1/42; 30-F11/ Biolegend	B304763	CTTTGTCTTTGTGAG	Day 21, female
TotalSeq™-B0306 anti- mouse Hashtag 6 Antibody	M1/42; 30-F11/ Biolegend	B289041	TATGCTGCCACGGTA	Day 21, male

5.14. CELLULAR INDEXING OF TRANSCRIPTOMES AND EPITOPES BY SEQUENCING

After sorting, the CD11b⁺ cell suspensions containing an equal number of cells in each sample (50,000 cells) were pooled together and centrifuged at 500 g, 4 °C for 10 min. Each pool consisted of a sample from each tested condition and replicates were separated between different pools in order to control for the batch effect (**Table 4.4**). Next, cells were suspended in 100 µl PBS and filtered through 40 µm Flowmi™ cell strainers (Scienceware). Next, cell density and viability were verified with an EVE™ Automatic Cell Counter (NanoEnTek Inc., USA), and if needed the cell suspension was diluted to a cell density of 700 – 1,200 cells/µl. Sample pools were run in triplicates, each replicate was loaded onto a separate chip well (10x Genomics). Subsequently, cell encapsulation and library preparation was performed with Chromium Controller (10x Genomics) and Chromium Next Gem Single Cell 3' Reagent Kit v3 with Feature Barcode technology for Cell Surface Protein (10x Genomics) according to the producer's user guide (CG000185 Rev D).

The library quality and quantity were assessed with a High-Sensitivity DNA Kit (Agilent Technologies, USA) on a 2100 Bioanalyzer (Agilent Technologies, USA). Sequencing was run on Novaseq 6000 (Illumina), with NovaSeq 6000 S2 Reagent Kit (Illumina), pair-end (Read 1 – 28 bp, Read 2 -100 bp). The sequencing depth was targeted to 4 x 10⁴ mRNA reads and 7 x 10³ Ab-oligo reads per cell. Sequencing was performed by the Genomics Core Facility in the Center of New Technologies, Warsaw; and by Paullina Szadkowska, M.Sc., Bartłomiej Gielniewski, Ph.D. and Bartosz Wojtaś, Ph.D. in the Laboratory of Molecular Neurobiology, Nencki Institute, Warsaw.

5.15. CITE-SEQ DATA PROCESSING

After sequencing, raw sequencing data (BCL files) were transformed to FASTQ files using the CellRanger v3.0.1 mkfastq^{113,117}. Next, sequencing reads were mapped to a mouse genome GRCm38 (mm10) acquired from the 10x Genomics website and quantified using a CellRanger v.4.0.0 count function^{113,117}. Subsequent data analysis was performed in R v3.6.1 using Seurat v3.2.3^{117,118}. First, input data count matrices were split into mRNA, protein panel, and HTO (hashtags) groups. The HTO data was normalized with CLR method using Normalize Data function. The normalized HTO reads were demultiplexed with HTODemux function in order to identify the sample of origin of each read. Based on the demultiplexing results, multiplets and empty droplets were determined and filtered out. After filtering, the sample identities were assigned to the cell based on the HTO indices. Next, the data set was filtered to remove data of

poor quality: cell with the percentage of mitochondrial reads > 10%, the number of transcripts <300, and a low ratio of unique transcripts per gene ($\log_{10}\text{GenesPerUMI} < 0.8$) were excluded. All samples were integrated into one data set (for RNA and protein panel separately) with a standard Seurat workflow.

The dimensionality reduction was performed with the PCA algorithm and data visualization in the 2D space was performed with the UMAP algorithm. Clustering analysis was performed using the FindClusters function. First, the clustree diagram was used for assessment of multiple clustering resolution and Res=1.1 was determined as an optimal value of the resolution. The differential expression analyses were performed with Find All Markers function applying the following parameters: min.pct=0.5, average log fold-change =0.25. The top expressed cluster genes and immune markers (Supplementary Table 1) were used to assign cell identities to clusters. The applied resolution was intentionally selected in a way to return a higher number of clusters than the number of expected cell populations (based on scRNA-seq analysis), in order to properly assess the diversity of cell types and cell states in obtained data set. Clusters that showed similar transcriptional patterns implying the same functionality were merged. The computational analysis of CITE-seq data was performed in cooperation with Paweł Segit, M.Sc. from the Laboratory of Molecular Neurobiology, Nencki Institute, Warsaw.

5.16. ANALYSIS OF THE INTERFERON-RELATED GENE SIGNATURE

The list of interferon-response genes was downloaded from the INTERFEROME v 2.0 database ¹²⁵. The applied search conditions included interferons of any type, subtype, and treatment concentrations. Genes obtained in both *in vitro* and *in vivo* experiments, in mouse and human were included. Only genes expressed in the brain, and by the cells overlapping with the following categories were included: microglial cell, blood monocyte-derived macrophages, monocyte-derived macrophages, derived macrophages, macrophages, Peripheral Blood Mononuclear Cells, bone marrow-derived macrophages. In total, 469 unique genes were identified, out of which 453 were found in the CITE-seq data set, within clusters belonging to microglia (MG), monocytes/macrophages (Mo/MΦ), and DCs populations. The heatmap demonstrating expression of the interferon-response genes was generated using Complex Heatmap v2.6.2 package, the hierarchical clustering was performed using ward.D2 method, and a dendrogram was ordered with a minimum distance.

For the IFN score, genes encoding proteins that belong to IFI, IFITM, and IRF protein families and were expressed in the CITE-seq data set in the clusters belonging to MG, Mo/MΦ,

and DCs populations were identified. The identified genes were as follows: *Ifi211*, *Ifih1*, *Ifi44*, *Ifi206*, *Ifi203*, *Ifi209*, *Ifi205*, *Ifi208*, *Ifi214*, *Ifi204*, *Ifi207*, *Ifi213*, *Irf9*, *Irf3*, *Ifitm5*, *Ifitm1*, *Ifitm3*, *Irf7*, *Irf5*, *Irf2*, *Irf8*, *Irf2bp1*, *Ifitm10*, *Irf2bp2*, *Ifitm6*, *Ifitm2*, *Ifi35*, *Irf1*, *Irf4*, *Irf2bpl*, *Ifit1*, *Ifit2*, *Ifit3b*, *Ifi27*, *Ifit3*, *Ifi47*, *Ifi27l2a*, *Ifit1bl1*. Next, the distribution of expression level across all cells for each of the genes was inspected individually on feature plots. The expression pattern was similar for all the genes, except *Irf7* and *Ifitm2* that were excluded from further analysis. The mean expression of the identified genes (38) was calculated per cell generating the IFN score.

5.17. ANALYSIS OF GAM PROPORTION IN PUBLIC HUMAN DATA SETS

For the analysis of proportions of distinct subpopulations within the GAM population, two public data sets were used: CyTOF data generated from human GBMs (n=14)⁷² and scRNA-seq data from primary human GBMs⁷⁷. For the CyTOF⁷² data analysis, fcs files were downloaded from the data repository (<https://data.mendeley.com/datasets/jk8c3c3nmz/draft?a=c0a9d8dc-8ac2-4942-baf9-208de7a8c310>). The downloaded data set contained preprocessed data of living cells from individual patients. Two experimental batches were merged using CytobatchAdjust package¹²⁶ and the analysis was performed with R 4.0.5 according to the Nowicka et al. (2019) workflow¹²⁷. The mass cytometry data were transformed with a cofactor 5 using an inverse hyperbolic sine (arcsinh) function. Myeloid cell fraction was obtained by excluding cells with expression levels of CD45 = 0, CD11b < 1.5, CD3 > 1.5. Only data for patients with GBM and with cell count > 8 · 10⁵ were taken for further analysis. Next, 8 · 10⁵ cells were randomly selected from each sample, and data were normalized between 0 and 1 to the 99th percentile of the merged sample. Clustering was performed with the k-nearest neighbors method using Rphenograph algorithm¹²⁸. Identified clusters were manually annotated and merged based on the similarity of antigen expression. The analysis of CyTOF data was done in cooperation with Karol Jacek, M.Sc. from the Laboratory of Molecular Neurobiology.

For scRNA-seq data set⁷⁷ analysis the cell type proportions were calculated based on cell annotations provided by the authors using a cell annotation matrix for human GBM scRNA-seq data set downloaded from <https://www.brainimmuneatlas.org/download>.

5.18. IMMUNOHISTOCHEMISTRY ON BRAIN SLICES

For tissue collection for histology, mice were anesthetized and transcardially perfused using first PBS and next 4% paraformaldehyde (PFA). Brains were dissected and post-fixed in 4% PFA overnight, then placed in 30% sucrose for 2 days, and then embedded in Tissue-Tek O.C.T

Compound. Cryosections (10 μm) were cut and stored at -80°C . Cryosections were blocked in PBS containing 10% donkey serum in 0.1% Triton X-100 solution for 2 hours and incubated overnight at 4°C with rat anti-Gal-3 and rabbit anti-Tmem119 antibodies. Next, sections were washed in PBS and incubated with corresponding secondary antibodies for 2 hours at room temperature. Nuclei were counter-stained with DAPI (0.1 mg/mL). Images were obtained on a Leica DM4000B fluorescent microscope. All antibodies were diluted in 0.1% Triton X-100/PBS solution containing 3% of donkey serum. For reagent specifications, catalog numbers, and concentrations see Table 5.6. The immunohistochemistry staining was performed by Kamil Wojnicki, M.Sc. from the Laboratory of Molecular Neurobiology, Nencki Institute, Warsaw.

Table 5.6 | Antibodies used for immunohistochemistry

Reagent	Manufacturer	Cat. number	Clone	Fluorophore	Dilution
anti-Gal-3	eBioscience	125408	M3/38	Alexa Fluor 648	1:200 FC 1:100 IF
anti-TMEM119 pAb	Synaptic Systems	400002	-	-	1:500
anti-MHC II	ThermoFisher	14-5321-82	M5/114.15.2	-	1:200
anti-rabbit Alexa Fluor 488 pAb	Invitrogen	A21206	-	Alexa Fluor 488	1:1000
anti-rat Alexa Fluor pAb	Invitrogen	A21208	-	Alexa Fluor 488	1:1000
anti-guinea pig Cy5 pAb	Jackson ImmunoResearch	706-175-148	-	Cy5	1:1000

5.19. PRIMARY MICROGLIA AND GL261 CO-CULTURES

Primary microglial cultures were prepared from cerebral cortices of P0–P2 old C57BL/6J male and female mice as described in Walentynowicz et al. (2018)⁵⁰. Microglial cells were seeded onto round glass coverslips at 5×10^5 per well in a 6-well plate and GL261 cells were seeded onto 0.4 μm inserts (Falcon) at 1.25×10^5 cells per insert. Twenty four hours after seeding, the inserts were transferred into the plate with microglial cells and co-cultured for 48h.

5.20. QUANTITATIVE GENE EXPRESSION ANALYSIS

RNA was isolated using RNeasy Mini Kit (QIAGEN, USA) and RT-PCR was performed using SuperScript III Reverse Transcriptase (Invitrogen) on 500 ng of total RNA. Quantitative real-time PCR was performed on 40 ng of cDNA in duplicates using TaqMan™ Fast Advanced

Master Mix (ThermoFisher) and TaqMan™ Gene Expression Assay (FAM) probes (ThermoFisher). Following probes were used: *Cd74* (Mm01262765_g1), *H2-Aa* (Mm00439211_m1), *H2-Ab1* Mm00439216_m1, *H2-Eb1* (Mm00439221_m1), *Gapdh* (Mm99999915_g1), *Actb* (Mm00607939_s1). Ct values were normalized to the endogenous expression of *Actb* and *Gapdh*. Similar results were obtained for both housekeeping genes, thus only *Actb* is presented. Delta Ct values obtained for technical replicates (n=2) were averaged and the linear model was built only with biological replicates (n=2). Apart from sex, also a litter of animals and genes were used as covariates. The analysis was done with R statistical environment.

5.21. DATA VISUALIZATION

The graphical schemes demonstrating experimental design were prepared with BioRender.com (Figure 6.6 a, 6.13a, 6.22 a) or Adobe Illustrator v24.1 (Figure 6.7a, 6.9a, 6.16b, 6.20a, 6.21 a). The flow cytometry graphs were prepared with FlowJo software v10.5 and GraphPad (Figure 6.10 c,d; 6.11 d,e; 6.12 d,e). The remaining graphs were prepared with R v 4.0.3 with the use of ggplot2 v3.3.3¹²⁹, ggpubr v0.4.0, ggrepel v0.9.1, ggriidges v0.5.3, VennDiagram v1.6.20, Complex Heatmap v2.6.2¹³⁰, clusterProfiler v3.12.0¹²² and Seurat v3^{117,118} packages and graphically arranged with Adobe Illustrator v25.4.

Following graphs types were employed:

- (1) Boxplot (Figure 6.1a; 6.2 e,f; 6.21 b,d); upper and lower hinges of the boxplots correspond to 25th and 75th percentile respectively, bar in the center represents median value and whiskers range from -1.5 to 1.5 of the interquartile range (IQR). Outliers defined as observations lower than 1.5 IQR or higher than 1.5 IQR are represented as single points. Individual data points were shown with dot plots (geom_dotplot) layered over boxplots (geom_boxplot).
- (2) The “knee” plots (Figure 6.3; 6.5); demonstrating the quality of scRNA-seq and sequencing saturation plots data were generated as part of the Cell Ranger pipeline and downloaded from the summary Html file.
- (3) Density plots (Figure 6.6 c; 6.11 b, 6.16 c; 6.19 c; 6.20 c,d; 6.21 c,e); kernel density estimate demonstrating the distribution of cells along with an expression level of a given gene/protein/score, generated with function geom_density_ridges.
- (4) UMAP/tSNE plots (Figure 6.7 b; 6.8 a,d; 6.9 a; 6.11 c; 6.13 c; 6.16 a; 6.17 a; 6.18 a, 6.20 a; 6.21 a); demonstrating scRNA-seq/CITE-seq metadata (clusters, conditions, sex)

across all cells arranged in 2D space with UMAP or tSNE algorithm, prepared using function `geom_jitter`, points opacity was set to 70% ($\alpha=0.7$), and cells were plotted in random order to avoid groups overlaying.

- (5) Feature plots (Figure 6.8 e; 6.10 a,b; 6.11 a; 6.12 a-c; 6.13 d-h, 6.14 a; 6.18 b-d; 6.19 b; 6.21 a); demonstrating scRNA-seq/CITE-seq feature level (gene expression, protein level, score value) across cells arranged in 2D space with UMAP or tSNE algorithm, extreme values of gene/protein expression level were cut to 99.9th percentile (scRNA-seq) or 1st and 99th percentile (CITE-seq, the bottom extreme values were also transformed due to data normalization, which yielded minimum values lower than 0), prepared using function `geom_jitter`.
- (6) Grid point plot (Figure 6.7 c); demonstrating expression level of selected genes from the immune marker panel (Supplementary Table 1) per cell cluster (mean), dot size corresponds to the percentage of cells showing expression of a given marker, generated with function `geom_point`.
- (7) Pie chart (Figure 6.7 d); generated with function `geom_bar()+coord_polar("y", start=0)`.
- (8) Heatmap (Figure 6.6 b; 6.8c; 6.9 c; 6.13 b; 6.19 a); heatmaps were prepared using either a feature level per cell – then each column represents an individual cell, or an averaged feature level in a given cell population. Plots were generated using `HTOHeatmap`, `DoHeatmap` functions from Seurat workflow or `heatmap` function from `ComplexHeatmap` package. If hierarchical clustering was applied, the dendrograms were generated with the `ward.D2` method and ordered by a minimum distance.
- (9) Network plots (Figure 6.9 d,e); results of the Gene Ontology analysis of biological processes were represented with `cnetplot` function from `clusterProfiler` package, top 5 terms are demonstrated.
- (10) Violin plots (Figure 6.8 f; 6.9 f,g; 6.16 d,e; 6.17 d); generated with function `geom_violin`, with default scale value ("area" - all violins have the same area) and no trimming.
- (11) Gene ontology
- (12) Scatter plot (Figure 6.9 b, 6.20 e); scatter plot generated using function `geom_jitter`. Figure 6.9 b supplemented with Venn Diagram representing the number of DE genes that were common or specific for each group, Venn Diagram was generated with `venn.diagram` function from `VennDiagram` package.

- (13) Stacked bar plot (Figure 6.6 d; 6.14 b; 6.21 b-d); representing proportion of selected cell population in given condition/patient, generated using function `geom_bar(position="fill")` or `geom_bar(position="stack")`.
- (14) "Pseudo-flow cytometry" graphs based on CITE-seq protein level (Figure 6.15; 6.16 f; 6.17 b; 6.18 f); generated with the use of the functions `geom_jitter` (individual points), `geom_density_2d` (lines of the contour plot demonstrating binned cell frequency), `stat_density_2d` (fill with the contour plot, the darker color corresponds to higher cell density), gates were set manually by drawing diagonal lines. The plots are supplemented with density plots demonstrating distribution of expression level of a single parameter and bar plots demonstrating generated with function `geom_bar`, demonstrating absolute number of cells from given population in a specified gate.
- (15) Half-volcano plots (Figure 6.17c; 6.18e), represent DE genes obtained with Wilcoxon test comparing cells from a given cluster (Mphi_1, Mphi_2, Mo-DCs, cDCs) to all cells from the Mo/Mphi population (Mo, Int, Mphi_1, Mphi_2, Mo-DCs, cDCs), p_{adj} was calculated with Bonferroni correction, plot generated with function `geom_jitter`, text labels were assigned using `geom_text_repel`.
- (16) Filled density plots (Figure 6.18 d, 6.19 d); demonstrate the frequency of a given cell population along with the expression level of selected genes, generated with function `geom_density_2d(position="fill")`.
- (17) Volcano plots (Figure 6.20b); represent DE genes obtained with Wilcoxon test comparing male and female cells within a given population, p_{adj} was calculated with Bonferroni correction, plot generated with function `geom_jitter`, text labels were assigned using `geom_text_repel`.

6. Results

6.1. KINETICS OF THE tdT+ LUC+ GL261-IMPLANTED TUMOR GROWTH

A murine GL261 glioma model was employed in the present study. The GL261-derived tumors carry *K-ras* and *p53* point mutations and are frequently used as syngeneic models of gliomas⁹⁹. These tumors recapitulate many characteristics of human glioblastomas (GBMs)¹³¹.

To verify the dynamics of the tumor growth, tdT=Luc+ GL261 cells were implanted intracranially to 10-week-old male C57BL/6 mice and imaged *in vivo* with the Xtreme platform every 7 days (Figure 6.1 a-b). The bioluminescent imaging allowed detection of the implanted tumors already at the 7 day post-implantation and demonstrated a significant increase of the tumor size in time (ANOVA (day) $F_{2,69} = 5.435$, $p_{val} = 0.006$). Importantly, the tumor size was found to be dependent on sex (ANOVA (sex) $F_{1,69} = 4.877$, $p_{val} = 0.031$) (Figure 6.1 a), as females showed smaller tumor sizes than males.

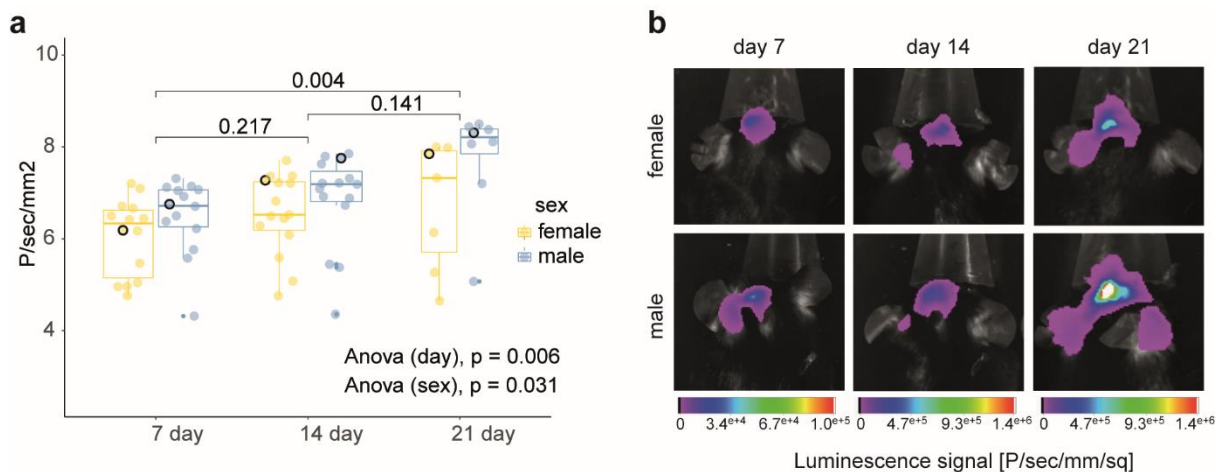


Figure 6.1 | Growth kinetics of the tdT+Luc+ GL261 murine gliomas. (a) Quantification of bioluminescent imaging at 7,14 and 21 day post-implantation. Two-Way ANOVA and Tukey's HSD post hoc test was performed. The results of the Tukey's HSD test for between days comparison are shown above the bars. Upper and lower hinges of the boxplots correspond to 25th and 75th percentile respectively, bar in the center represents median value and whiskers range from -1.5 to 1.5 of the interquartile range (IQR). Outliers defined as observations lower than 1.5 IQR or higher than 1.5 IQR are represented as single points. (b) Representative tumor images. Observations corresponding to the selected images are marked with thick black border on the Figure 6.1a.

6.2. OPTIMIZATION OF DISSOCIATION AND FLUORESCENCE-ACTIVATED CELL SORTING PROCEDURES

Both scRNA-seq and CITE-seq required enrichment of the CD11b⁺ myeloid cells with fluorescence-activated cell sorting (FACS). Prior to FACS, the brain tissue needs to be dissociated to obtain a single cell suspension. The procedure optimized in the Laboratory of Molecular Neurobiology, which yields the best sample purity and viability includes

enzymatic digestion with the papain enzyme mix (Neural Tissue Dissociation Kit with papain, Miltenyi Biotec). However, it needs to be taken into consideration whether the epitopes of interest are not affected during the steps of enzymatic digestion.

Papain digests the epitopes of Tmem119⁶³, a surface protein that was included in the protein panel for the CITE-seq analysis. To preserve the Tmem119 epitopes, papain was substituted with DNase I (0.5 mg/ml), and brain tissue dissociation was performed according to the standard procedure (see Methods). Both dissociation methods allowed obtaining a single cell suspension, and identification of CD11b⁺ population with flow cytometry (**Figure 6.2 a,b**). The fraction of alive cells was significantly lower in the DNaseI than in papain digested samples (Papain median=92.1%, DNase I median=55.8%, Wilcoxon test $p = 7.1 \cdot 10^{-5}$) (**Figure 6.2 e**). However, the majority of CD11b⁺ cells were found in the fraction of alive cells, as indicated by the gating on the Live/Dead stain, Pacific Blue A channel (**Figure 6.2 c,d**). The percentage of live CD11b⁺ cells was also lower in the samples digested with DNase I than in papain-digested samples, although the difference was minor (Papain median=96.3%, DNase I median=93.8%, Wilcoxon test $p = 0.00077$) (**Figure 6.2 f**). Therefore, in the procedures requiring assaying Tmem119, samples were processed with DNase I. Additionally, all sorting procedures included dead cells exclusion with a viability dye (see Methods).

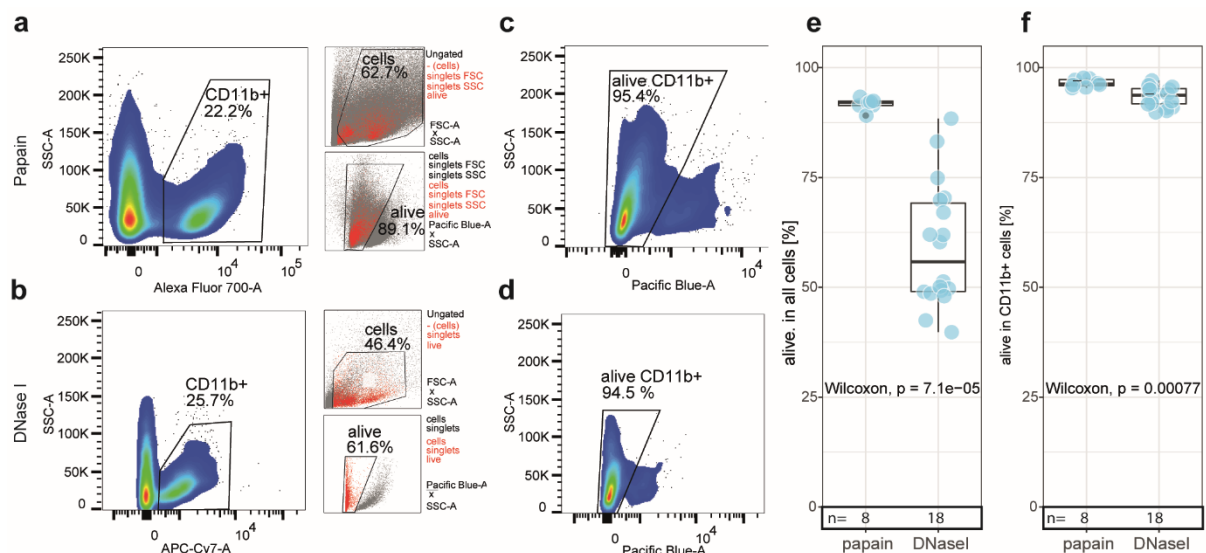


Figure 6.2 | Assessment of cell viability in the brain tissue preparations dissociated with Papain and DNaseI. (a,b) CD11b⁺ gate with backgating of “Ungated cells” on FSCxSSC and singlets on Pacific Blue (Live/Dead stain) x SSC for Papain – a, and DNase I preparation – b. (c,d) Gate for alive cells for CD11b⁺ cells without dead cells exclusion in Papain – c, and DNase I preparation – d. (e,f) Quantification of alive cells in all singlet cells (e) and in CD11b⁺ cells (f) in cell preparation for scRNA-seq (Papain) and CITE-seq (DNase I) (two-sided Wilcoxon Rank Sum Test. Upper and lower hinges of the boxplots correspond to 25th and 75th percentile respectively, bar in the center represents median value and whiskers range from -1.5 to 1.5 of the interquartile range (IQR)). Outliers defined as observations lower than 1.5 IQR or higher than 1.5 IQR are marked with black points.

6.3. QUALITY ASSESSMENT OF THE scRNA-SEQ READS

The scRNA-seq capability to assess the cell heterogeneity heavily depends on the number of cells included in the analysis. However, increasing the cell number loaded onto a single well of the encapsulation chip is connected with an elevated number of multiplets that can negatively influence the computational analysis. For the scRNA-seq, the targeted number of cells was equal to 5,000 cells/sample, which is within the recommended range (1,000-10,000 cells) and provides a high number of cells with a relatively low number of multiples (4 %) ^{113,132}.

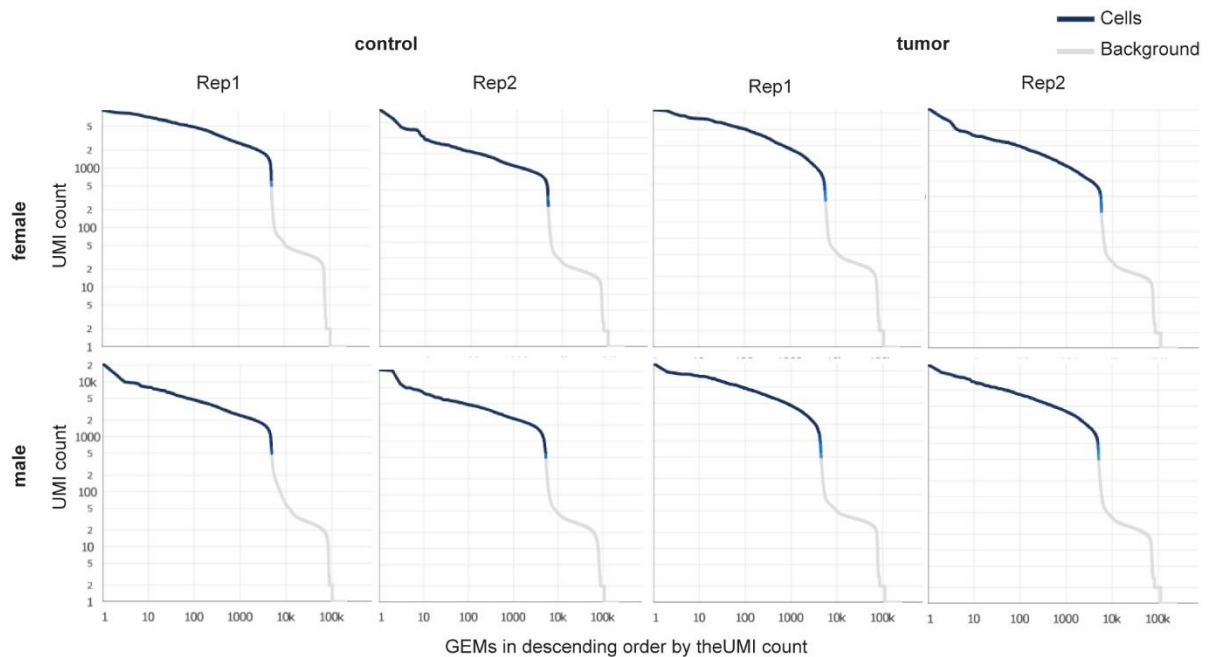


Figure 6.3 | Knee plots for assessment of the quality of reads obtained for scRNA-seq. The reads identified as background were removed from further analysis.

The “knee” plots showing the number of unique RNA reads (UMI – unique molecular identifier) obtained per single gel-bead in emulsion (GEM), demonstrated a good quality of the obtained data. The “knee” plots allow separating GEMs that contained cells, from the empty GEMs in which only free-floating mRNA was amplified. The empty GEMs are indicated by a sudden drop of the UMI counts (**Figure 6.3**).

The obtained number of cells in each sample was close to the number of targeted cells (**Table 6.1**), demonstrating accurate cell loading during the encapsulation procedure. Samples were sequenced in pairs (~10,000 cells per sequencing run) on the HiSeq1500 (Illumina) instrument (up to 4×10^8 total reads), which allowed to obtain ~36 thousand reads per cell and a high level of sequencing saturation (mean=87%) (**Table 6.1**).

Table 6.1 | The scRNA-seq sequencing details before and after applying filtering steps.

	female				male				mean	sum
	control rep1	control rep2	tumor rep1	tumor rep2	control rep1	control rep2	tumor rep1	tumor rep2		
cells identified	5,223	4,870	5,802	5,579	4,873	5,301	4,402	5,009	5,150	41,059
reads per cell	42,512	33,630	31,190	31,680	35,228	37,195	43,450	31,842	36,412	
median genes per cell	1,008	1,092	1,099	1,067	984	1,008	1,219	1,091	1,071	
saturation	90.1%	87.0%	83.8%	84.7%	88.6%	89.5%	86.2%	84.9%	87%	
cells after filtration	5,167	4,787	5,654	5,491	4,820	5,239	4,306	4,937	5,066	40,401
genes after filtration	12,520	12,720	13,424	13,192	12,636	12,781	12,978	13,030		

6.4. ANTIBODY-OLIGONUCLEOTIDE CONJUGATION

CITE-seq utilizes antibodies conjugated with oligonucleotide tags (Ab-oligos) for assessment of the surface protein level. Before cell loading to an encapsulation chip, cells are stained with the Ab-oligos. Subsequently, the oligonucleotide tags are indexed with the cellular barcode and processed through library preparation and sequencing steps similarly to the mRNA molecules. In this study, we utilized a panel of 10 Ab-oligos for the assessment of the surface protein expression, 7 of which were commercially available (TotalSeq™, Biolegend), and 3 were conjugated in-house. To obtain an optimal conjugation efficiency, three ratios of the antibody: oligonucleotide volumes in the conjugation mixture were tested. The Ab-oligo conjugation was assessed with SDS-PAGE along with the positive control (“+ctrl” - commercially available Ab-oligo conjugate TotalSeq™-A0014 anti-mouse/human

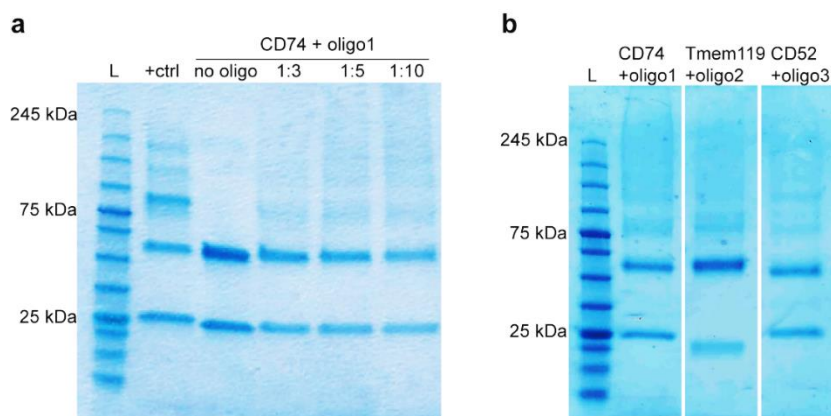


Figure 6.4 | **SDS-PAGE of the antibody-oligonucleotide conjugates.** (a) Assessment of the antibody and oligonucleotide ratio in the conjugation mixture, from the left: L- protein size marker, +ctrl – commercial antibody-oligonucleotide conjugate TotalSeq™-A0014 anti-mouse/human CD11b Antibody (Biolegend) used as a positive control, no oligo – CD74 antibody without conjugation used as negative control, 1:3/ 1:5/ 1:10 – tested ratios of antibody and oligonucleotide amounts: 1 part of antibody and 3, 5 and 10 parts of oligonucleotide respectively. (b) Assessment of conjugation efficiency of all antibody-oligonucleotide conjugates mixed in a ratio 1:10.

CD11b Antibody, Biolegend), and the negative control (“no oligo” -CD74 antibody before conjugation) (Figure 6.4 a). Bands observed for the unconjugated antibody (no oligo) represent the light and heavy antibody chain. Bands that are observed at higher molecular weights represent the Ab-oligo conjugate. A single antibody can be conjugated with more than one oligonucleotide molecule, which is demonstrated by multiple bands of the Ab-oligo conjugates. The conjugation at 1:10 ratio resulted in the most intense Ab-oligo bands, which best recapitulated the band pattern obtained for the positive control. Thus, the 1:10 ratio was applied for the conjugation of all antibodies, and the successful conjugation was confirmed with SDS-PAGE (Figure 6.4 b).

6.5. QUALITY ASSESSMENT OF THE CITE-SEQ READS

The CITE-seq libraries consist of two library types: mRNA that is prepared in the same way as for the scRNA-seq experiment, and Ab-oligo that contains reads generated from the Ab-oligo conjugates (both protein panel and cell hashtags). The mRNA and Ab-oligo libraries are separated, which allows adjusting sequencing depth to each library type.

In the CITE-seq experiment, it was aimed to achieve 14,000 (Exp1) and 16,000 (Exp2) cells in a single replicate, and a minimum of 35,000 RNA reads and 10,000 Ab-oligo reads per cell. The targeted number of the RNA reads provided good saturation in a previous scRNA-seq experiment. For the Ab-oligo libraries, the recommended sequencing depth ranges between 5,000 -7,000 reads per cell. However, to make sure that the obtained depth will allow separating samples that were barcoded with the hashtag antibodies and assessing the expression level of proteins included in the Ab-oligo protein panel, the targeted number of Ab-oligo reads per cell was increased to 10,000.

Table 6.2 | The CITE-seq sequencing details before and after applying filtering steps.

	Exp1	Exp2		mean	sum
	Rep1	Rep2	Rep3		
Cells identified	13,978	11,055	16,324	13,785	41,357
RNA reads per cell	35,863	67,527	44,522	49,304	
median genes per cell	1,694	2,523	1,496	1,904	
Saturation	77.6%	77.7%	78.8%	78.03%	
Ab-oligo reads per cell	12,031	25,489	17,432	18,317	
Cells post filtration	11,632	9,217	1,548		22,397

The CITE-seq experiment was divided into two rounds. First (Exp1) included one replicate (Rep1), in which all the targeted sequencing parameters were achieved ([Table 6.2](#)) and the cell-containing GEMs were clearly separated from the background GEMs ([Figure 6.5](#)). Additionally, the computational analysis showed that all the Ab-oligo barcodes that were included in the protein and cell hashing panel ([Table 5.3 and 5.4](#)) can be identified.

Upon verification of the successful RNA and Ab-oligo libraries sequencing, the CITE-seq was performed for the remaining replicates (Exp2: Rep2 and Rep3). In Rep3, the “knee” plot indicated a failure preventing reliable identification of the cell-containing GEMs, which was inspected in the subsequent computational analysis (see [Figure 6.6](#)). The number of obtained cells differed from the targeted number. Still, the minimal sequencing depth was achieved and all samples showed a similar saturation rate ([Table 6.2](#)). Surprisingly, the saturation rate was lower than in the scRNA-seq experiment, although exceeding the targeted number of reads per cell. The lower saturation rate could be connected with the higher number of genes per cell detected in the CITE-seq (mean 1,904), as compared with the scRNA-seq (mean= 1,071). This could be achieved due to employing a new generation of the 10x Genomics chemistry for the CITE-seq library preparation (v3), which offers improved RNA capture efficiency as compared to the chemistry employed in the scRNA-seq experiment (v2) (see Methods). The saturation plots indicated that the saturation was already achieving plateau, thus increasing the number of reads by additional sequencing would not provide a substantial improvement of the library complexity ([Figure 6.5 b](#)).

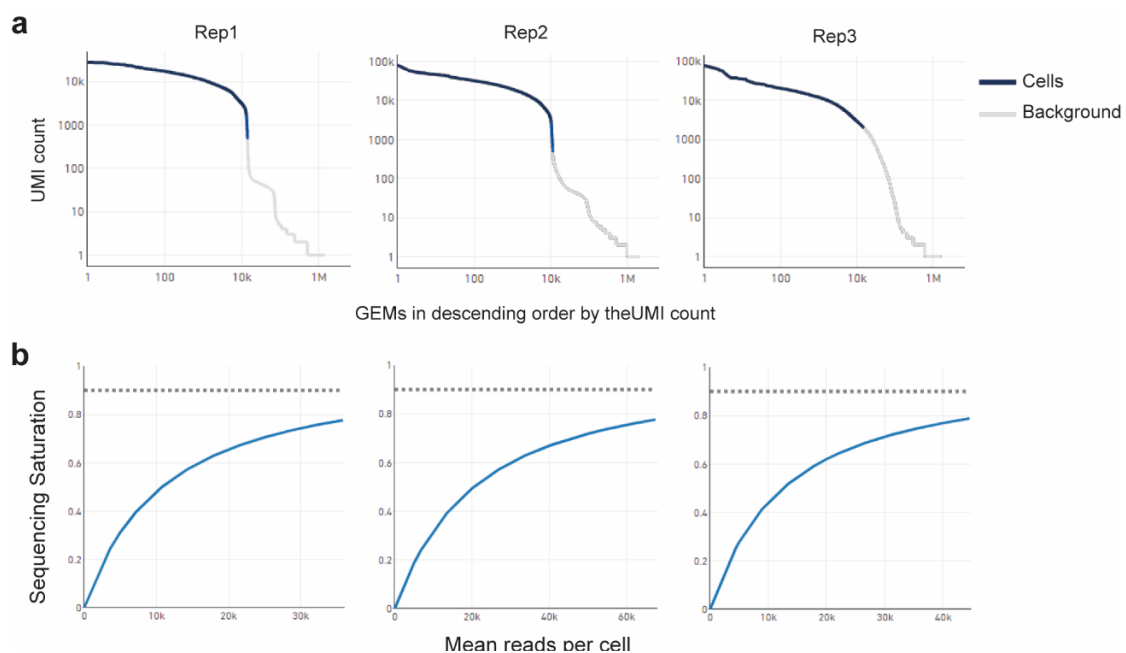


Figure 6.5 | Plots for the CITE-seq quality assessment. (a) Knee plots demonstrating separation of the cell containing and background GEMs. (b) Sequencing saturation plots demonstrating the relation between increasing number of reads per cell and saturation of the sequenced reads.

6.6. SAMPLE IDENTIFICATION WITH THE CELL HASHTAG-OLIGO BARCODES

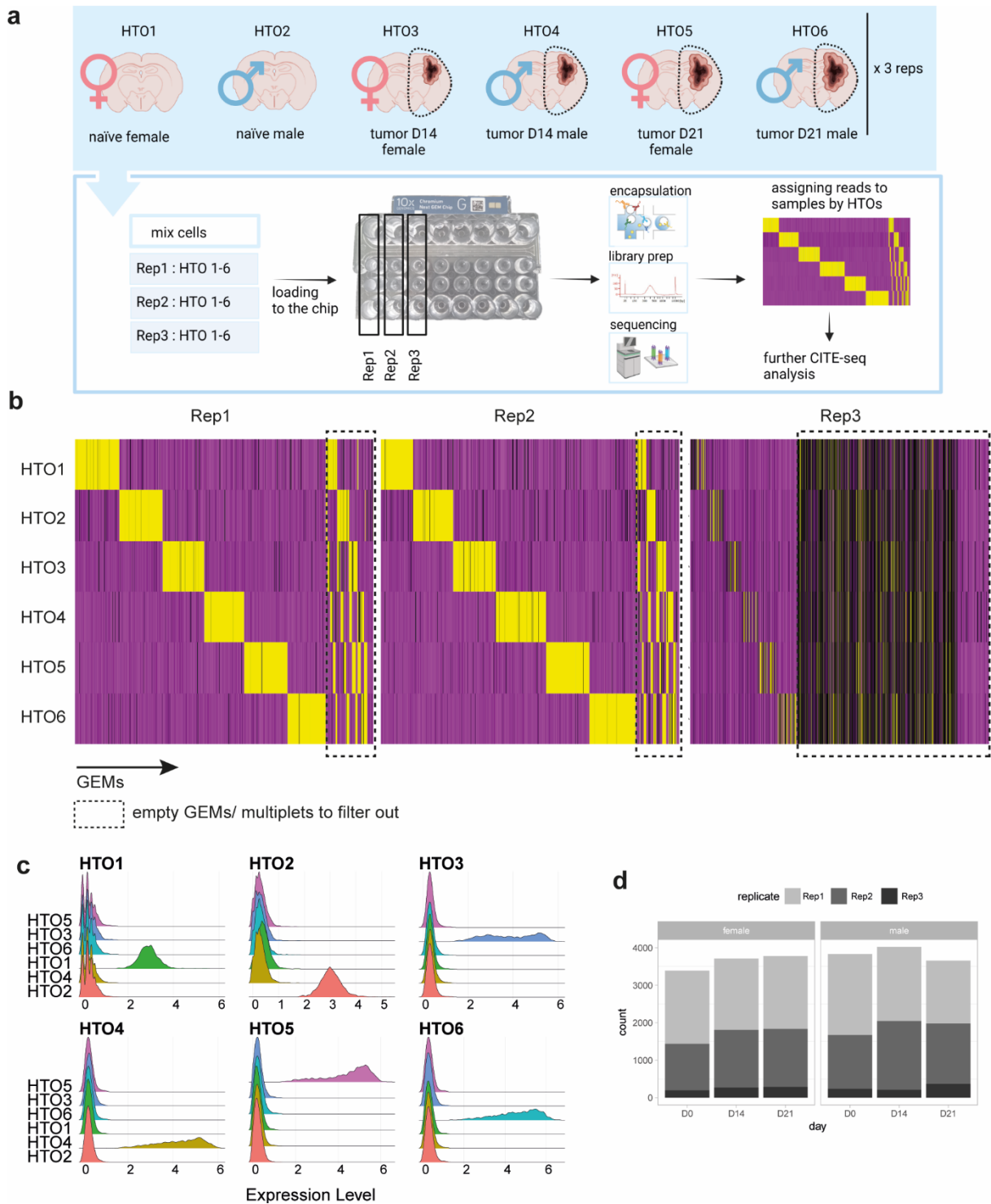


Figure 6.6 | Sample identification with the cell hashtag-oligo barcodes. (a) Schematic representation of the hashing procedure, prepared with BioRender.com. (b) Heatmaps demonstrating the number of HTO barcodes identified per GEM, a dotted line marks multiplets and empty GEMs that were discarded prior to further analysis. (c) Ridge plots showing expression of single, sample-specific hashtag in each sample after filtering the multiplets and empty GEMs. Example for replicate 1 is shown. Replicate 2 and 3 are shown in the Supplementary Figure 1. (d) Final number of cells obtained after all filtering steps for all conditions and replicates.

Cell hashing is a method of cell samples barcoding with the Ab-oligo conjugates that allows mixing different samples before being loaded onto the chip for encapsulation. Such an approach allows reducing the costs and increasing the number of replicates. In the procedure of encapsulation, a certain fraction of GEMs consists of multiple cells (multiplets), which can negatively affect the computational analysis. The higher number of cells loaded, the higher is the multiplets rate. Thus, in the standard scRNA-seq presented in this work, the number of target cells was limited to 5,000, which corresponds to the multiplet rate of around 4%. Cell hashing allows identifying multiplets consisting of cells from distinct samples and thus discarding the majority of the multiplets from further analysis. Thanks to that, the total number of target cells can be increased even up to 20,000 target cells/well¹¹⁶, without the risk of having a very high multiplet rate.

In the CITE-seq procedure, cell samples from all the conditions were given a specific cell hashtag-oligo barcode (HTO), mixed and loaded onto a single well (**Figure 6.6 a**). This approach allowed overcoming batch effects, generated during encapsulation, library preparation and sequencing, as all those steps were performed simultaneously for all the conditions. A total of three replicates in two independent experiments were prepared. Following sequencing, reads were assigned to samples using the HTO barcodes. As expected, GEMs in which multiple cells with different HTOs were encapsulated, appeared as readouts with more than one type of HTO barcode and were assigned as multiplets (**Figure 6.6 b**). Next, multiplets and GEMs with no HTO barcode were discarded from further analysis. In replicate 3 (Rep3), a large fraction of such GEMs was obtained, which could result from an encapsulation failure or a premature breakdown of the GEM emulsion. Since a fraction of GEMs in the Rep3 appeared as singlets, we decided to include them in further analysis, although the relatively small number. After filtering out the empty GEMs and multiples, all samples showed the presence of a single HTO type, which allowed for a clear distinction from the other samples (**Figure 6.6 c**).

Following the sample identification, cells were filtered with the quality control parameters (parameters with thresholds - see Methods, Supplementary Figure 2). The final number of cells obtained from each replicate differed due to the high multiplet rate in the Rep3 (Rep1- 11,632, Rep2- 9,217, Rep3- 1,548). Still, each replicate showed a similar contribution to all the tested conditions (**Figure 6.6 d**).

6.7. IDENTIFICATION OF IMMUNE CELL TYPES ACROSS THE GLIOMA-INFILTRATING MYELOID CELLS WITH SCRNA-SEQ

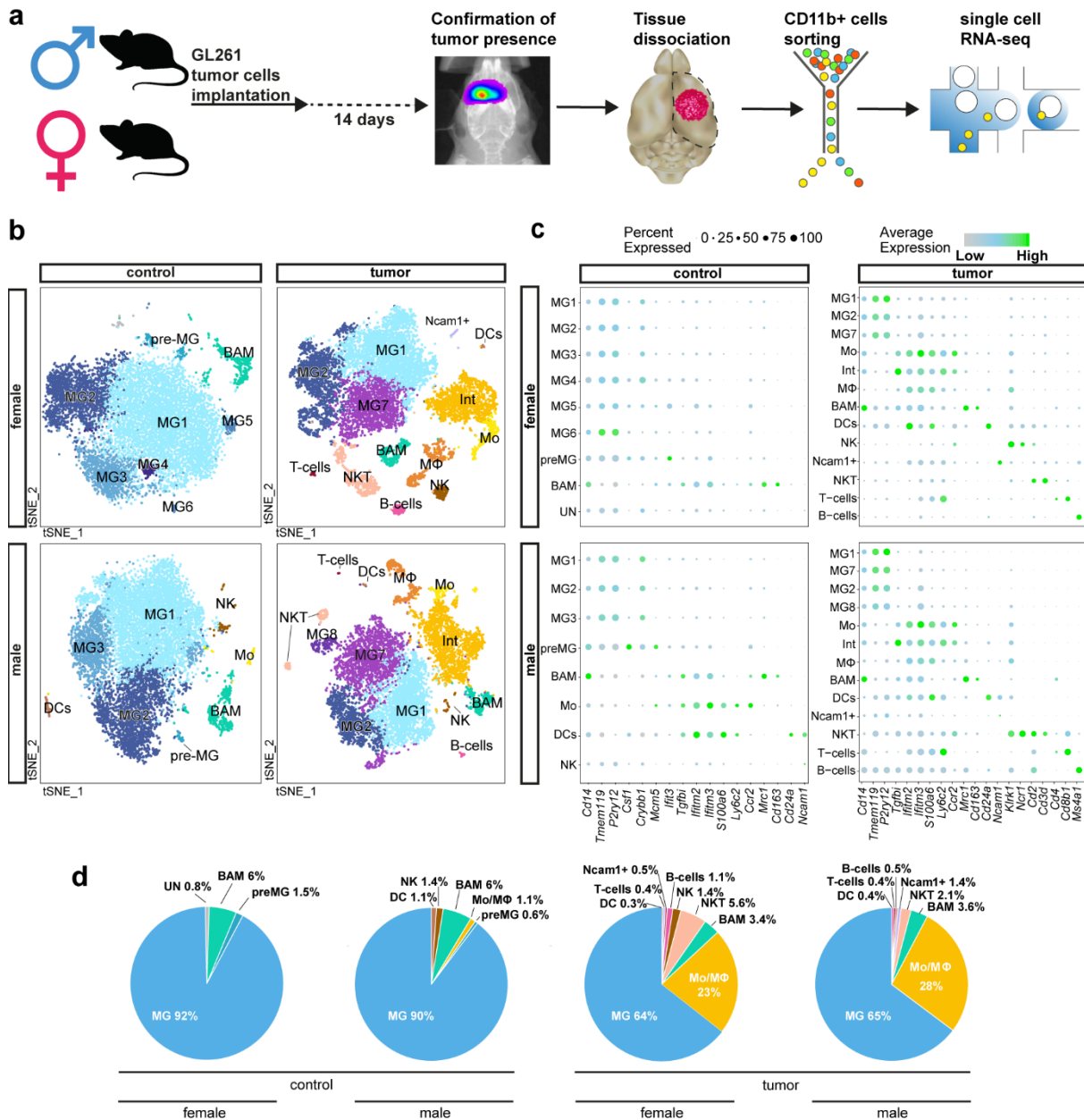


Figure 6.7 | Cell type identification based on scRNA-seq expression profiles. (a) Scheme of the experimental workflow. The used brain image was modified from Database Center for Life Science. (b) t-SNE plot demonstrating clustering obtained for each group (female control, female tumor, male control, and male tumor), two biological replicates were combined. Clusters annotations: MG - microglia, preMG - premature microglia, Mo - monocytes, Int - intermediate monocyte–macrophage, MΦ - macrophages, BAM - CNS border-associated macrophages, DCs - dendritic cells, Ncam1+ - Ncam1-positive cells, NK - natural killer cells, NKT - natural killer T cells, B cells - B lymphocytes, T cells - T lymphocytes. (c) Expression of the “signature” genes selected from the immune marker panel for identification of a cluster cell type (Supplementary Table 1). (d) Pie charts demonstrating distribution of the identified cell types across samples.

To assess the heterogeneity of the myeloid cells infiltrating gliomas, we performed the scRNA-seq on CD11b⁺ cells sorted from male and female brains of naïve and GL261-implanted animals (pool of 2 animals in each replicate, 2 replicates) (**Figure 6.7 a**). The analysis was performed on the 14th day post-implantation that corresponds to a pre-symptomatic stage of tumor progression, in which there are no signs of necrosis, and BM-derived macrophages and microglia occur in equal proportions ⁵⁷.

The scRNA-seq analysis identified 40,401 cells and 14,618 genes after applying the quality control filtering steps (see Methods). To assess the transcriptomic cell diversity, the data was projected onto the two-dimensional space with t-distributed stochastic neighbor embedding (t-SNE). The graph-based clustering was performed for each condition separately, using the same value of the resolution parameter that controls the number of obtained clusters (See methods). The number of clusters obtained for male and female animals within the same condition was similar, whereas between conditions the number of clusters was higher for the tumor-bearing brains compared to the brains of naïve animals (male control= 9, female control=8, male tumor 13, female tumor= 13), reflecting an increased cell diversity in the tumor microenvironment.

The cell types of the obtained clusters were identified using significantly overexpressed genes in each cluster and an immune cell marker panel, designed with the literature-based markers (**Figure 6.7 b,c, Supplementary Table 1**). The naïve brains consisted mainly of microglia (MG) that constituted 92% and 90% of the CD11b⁺ cells in males and females, respectively. Additionally, naïve brains showed the presence of a microglial cluster that exhibited increased expression *Csf1*, *Mcm5*, *Ifit3* genes, indicative of a premature state (pre-MG) ¹³³.

Other cell types found in the naïve brains included CNS border-associated macrophages (BAMs), and a minor fraction of dendritic cells (DCs), natural killer cells (NK), and monocytes (Mo) that were found only in male brains (**Figure 6.7 d**). Contrastingly, the tumor-bearing brains showed a smaller fraction of MG (females- 64%, males- 65%), due to infiltration of the BM-derived monocytes and macrophages (Mo/MΦ) from the periphery.

Among the Mo/MΦ population, 3 clusters were distinguished for both males and females. Those clusters were identified as monocytes (Mo) that had high expression of *Ly6c2* and *Ccr2* genes, typical for infiltrating monocytes; differentiated macrophages (MΦ) which expressed *Ifitm2*, *Ifitm3*, *S100a6* at a high level, but showed low expression of *Ly6c2* and *Ccr2*; and a

monocyte-to-macrophage intermediate population (Int) that had increased expression of both *Ly6c2*, *Ccr2* and *Ifitm2*, *Ifitm3*, *S100a6* genes.

Additionally, the CD11b⁺ cells from the tumor-bearing brains consisted of DCs, NK, natural killer T cells (NKT) and a marginal fraction of B and T cells. Expression of CD11b is not typical for lymphocytes, thus the presence of NKT, T and B cells was not expected. However, detection of rare CD11b⁺ lymphocytes in the brain during viral infections has been already reported^{134,135}.

Since the main aim of this work was to dissect the transcriptional heterogeneity of the brain resident microglial cells and BM-derived monocytes and macrophages within the tumor microenvironment, the further analysis focused on the MG, Mo/MΦ, and BAMs that are the most abundant cell populations found in the glioma TME.

6.8. SCRNA-SEQ EXPRESSION PROFILES DISTINGUISH MICROGLIA AND MONOCYTES/MACROPHAGES

Cells belonging to clusters identified as MG, Mo/MΦ, and BAMs were selected. The cells from all conditions were combined and re-clustered. The re-clustering resulted in obtaining three separate groups corresponding to MG, Mo/MΦ, and BAMs, as demonstrated by the projection onto the two-dimensional space with a Uniform Manifold Approximation and Projection (UMAP) algorithm (**Figure 6.8 a**). The composition of the obtained groups was largely corresponding with the identity of cell clusters obtained for separate conditions (**Figure 6.8 b**). Thus, demonstrating a predominance of a biological signal over technical artifacts or batch effects.

To confirm the identity of the obtained groups, differential expression analysis was performed. Among the top 10 most highly upregulated genes, we found commonly acknowledged canonical microglia genes – *P2ry12*, *Sparc*, *Tmem119*, *Gpr34*, *Selplg*, *Cx3cr1*^{61,136} in MG group; genes highly expressed by monocytes – *Ly6i*, *Ly6c2*, and macrophages – *Ifitm3*³⁸ in the Mo/MΦ group, and genes previously reported for BAMs – *ApoE*, *Ms4a7*, *Mrc1*¹³⁷ in the BAMs group (**Figure 6.8 c**).

In search of marker candidates that could be applied for the separation of microglia and macrophages in the TME, the specificity and expression rate of the top expressed genes were examined. *Tmem119*, *Cx3cr1*, *P2ry12*, *Gpr34*, *Olfml3*, and *Sparc* were enriched only in MG (**Figure 6.8 c**, **Supplementary Figure 3**). Whereas the other genes expressed at a high level in MG were also highly expressed in BAMs (*Cd81*), BAMs and Mo/MΦ (*Hexb*, *Cst3*) or were found only in a fraction of MG cells (*P2ry13* gene was expressed by less than 75% of MG cells) (**Supplementary Figure 3**). For Mo/MΦ, we found enriched expression of previously reported

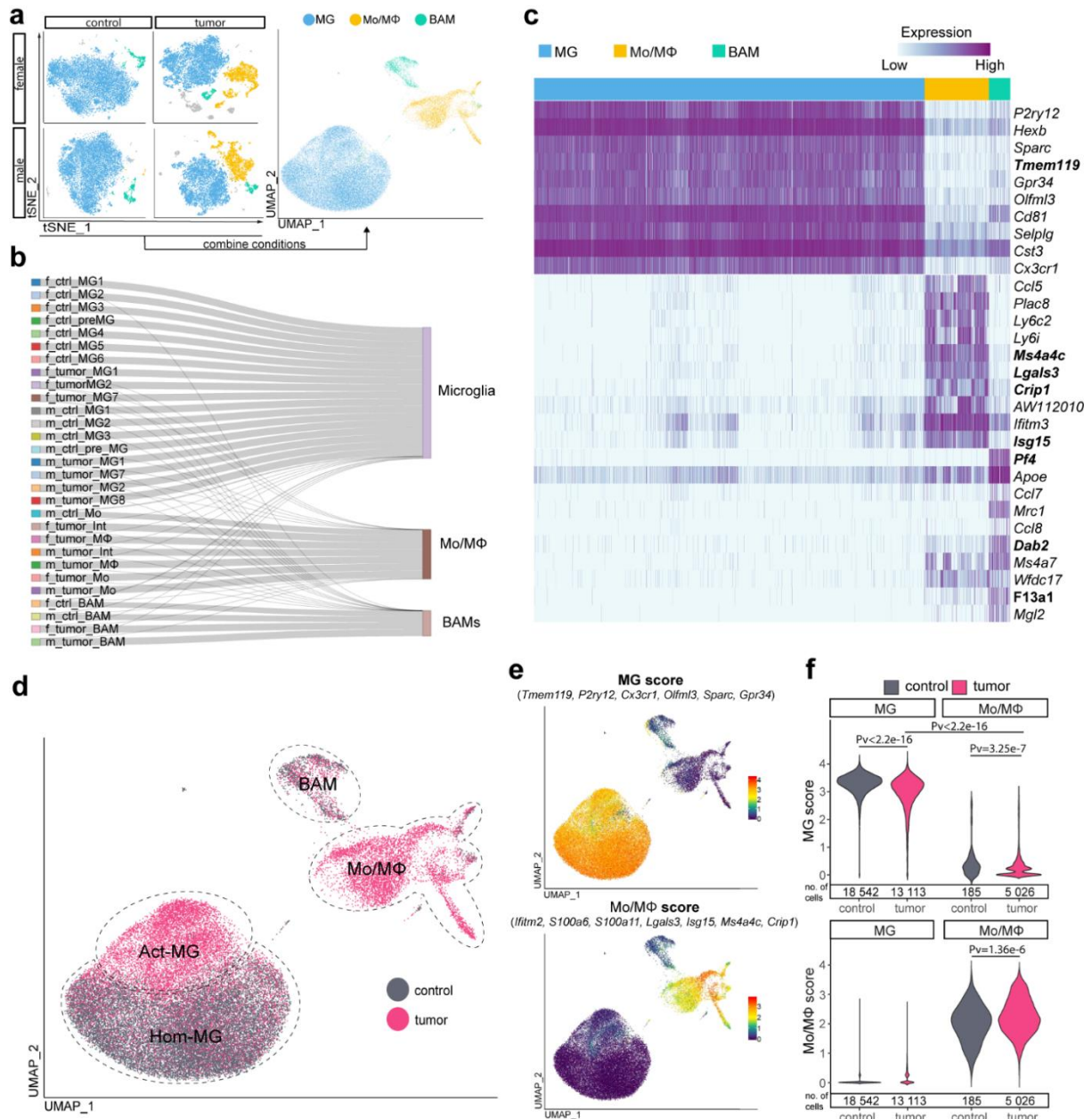


Figure 6.8 | scRNA-seq expression profiles distinguish between microglia and monocytes/macrophages. (a) Schematic representation of selection of cell clusters (as MG, Mo/MΦ and BAMs) from clustering performed for each condition separately, and re-clustering those cells for all the conditions combined. (b) Projection of the clusters from first clustering onto the cell clusters obtained after re-clustering for combined conditions. (c) Heatmap demonstrating top 10 differentially expressed genes ranked by the average log fold-change value, all with adjusted (Bonferroni correction) p-value < 10⁻¹⁰⁰. New marker candidates are given in bold. (d) UMAP plot demonstrating distribution of the control- and tumor-derived CD11b⁺ cells across cell populations for the combined clustering. (e) Feature plots showing levels of MG and Mo/MΦ scores (average expression of the selected genes that are given in brackets). (f) Violin plots comparing level of MG and Mo/MΦ scores between each other and between the control and tumor condition (two-sided Wilcoxon signed-rank test).

genes such as *Ifitm2*, *S100a6*, and *S100a11*³⁸, as well as novel genes, namely *Ms4a4c*, *Lgals3*, *Crip1*, and *Isg15* (**Figure 6.8 c, Supplementary Figure 3**). *Ifitm3* was highly expressed by the Mo/MΦ population, but appeared also in a substantial fraction of MG, showing its low specificity towards monocytes/macrophages within glioma TME. *Lgals3* was found to be a promising marker candidate as it encodes surface protein Galactin-3 (Gal-3) and its expression was enriched predominantly in the Mo/MΦ. BAMs showed high expression of *ApoE* and *Ms4a7*, which were recently proposed as markers of CNS border macrophages¹³⁷. However, those genes showed also high expression in Mo/MΦ, suggesting that *ApoE* and *Ms4a7* are not exclusive for BAMs in the TME. On the contrary, *Mrc1* expression was restricted to BAMs. Additionally, *Pf4*, *Dab2* and *F13a1* were also highly and specifically expressed by BAMs (**Figure 6.8 c, Supplementary Figure 3**).

The distribution of cells derived from naïve and tumor-bearing brains across clusters revealed that the MG clusters group by condition. The MG clusters enriched in cells derived from the naïve brains were assigned as homeostatic microglia (Hom-MG), and clusters consisting mostly of cells from the tumor-bearing brain as glioma-activated microglia (Act-MG). Mo/MΦ cells were derived mainly from the tumor-bearing brain, as they rarely occur in the brain under homeostatic conditions. Whereas BAMs did not show any condition-dependent grouping, although cells from both conditions were represented (**Figure 6.8 d, Supplementary Figure 4**). This result demonstrates that TME induces substantial changes in the transcriptional profile of microglial cells, which is not observed for BAMs.

Therefore, the influence of TME on microglia and monocyte/macrophage “signatures” was examined. Genes demarcating a given population were selected to generate MG and Mo/MΦ scores, defined as an average of the expression levels of the selected genes (**Figure 6.8 d**). Comparison of the MG score across conditions indicated a shift toward lower microglial “signature” in tumor-derived compared with control-derived cells. Still, the MG score for microglia from the tumor-bearing brains was high and distinguishable from Mo/MΦ. Similarly, the Mo/MΦ score was high and distinctive for the Mo/MΦ group, as compared with the MG group. Thus, demonstrating that the signature genes of microglia and monocyte/macrophages are retained even under the strong influence of the glioma environment.

6.9. TMEM119 AND GAL-3 SEPARATE MICROGLIA AND MONOCYTE/MACROPHAGES WITHIN THE TME AND SHOW THE DISTINCT LOCALIZATION

A major aim of this project was to identify cell markers for the separation of microglia and monocytes/macrophages within the glioma microenvironment. From the top differentially expressed genes in the MG and Mo/M Φ groups, candidate genes of enriched expression in the majority of cells within the target group were selected – *Tmem119* (MG) and *Lgals3* (Mo/M Φ) (Figure 6.9 a,b). *Tmem119* was already proposed for the microglia marker by Bennet et al. (2017)⁶¹, who confirmed its utility in CNS inflammation and nerve injury. *Lgals3* encodes

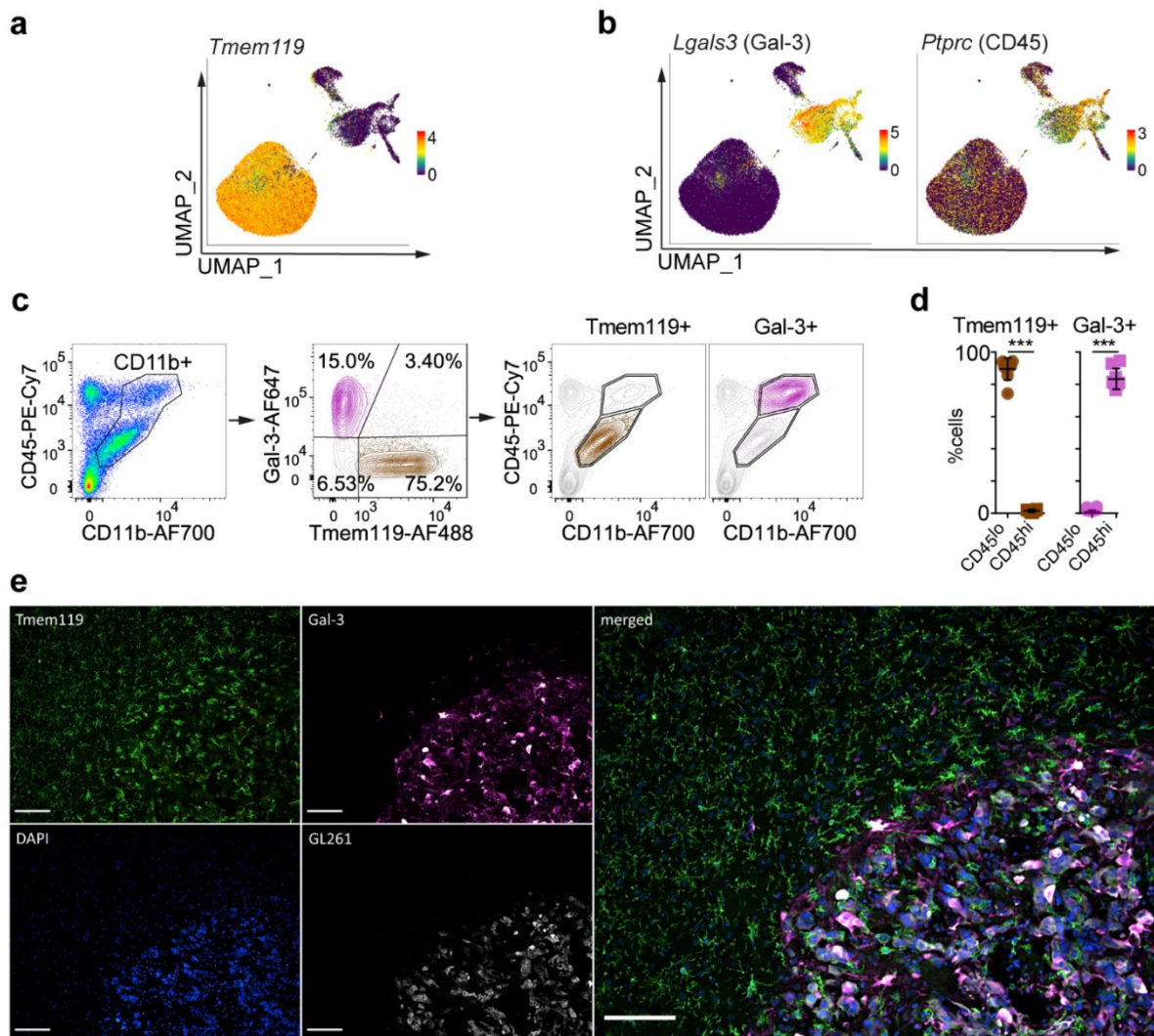


Figure 6.9 | Validation of *Tmem119* and *Gal-3* as cell markers separating microglia and monocyte/macrophages population within the TME. (a) Feature plots demonstrating expression level of genes highly expressed in MG and (b) Mo/M Φ . (c) Flow cytometric analysis showing separation of the CD11b⁺ cells with *Tmem119* and *Gal-3*, and projection of the CD11b⁺ and *Tmem119*⁺ cells onto CD45/Cd11b graphs. (d) Dot plots showing quantification of the *Tmem119*⁺ cell fraction within the CD11b⁺CD45^{lo} gate, and *Gal-3*⁺ cells fraction within the CD11b⁺CD45^{hi} gate (n=8, 4 males and 4 females, two-sided Wilcoxon Rank Sum Test, mean \pm SD, ***<0.001, *Tmem119* Pv=0.0002, *Gal-3* Pv=0.0002). (e) Immunohistochemical staining for microglia (*Tmem119*⁺, *Gal-3*⁻) and Mo/M Φ (*Tmem119*⁻, *Gal-3*⁺) shows the localization of specific immune cells within the tumor and its surroundings in female animal (for male see Supplementary Figure 5); a dashed line marks the tumor edge; scale - 100 μ m; the staining was performed for 3 animals, 4 sections each. a representative image is shown.

Gal-3, a lectin involved in tumor immunosuppression¹⁴². Gal-3 is produced and secreted by macrophages, regulates IL-4 induced alternative macrophage activation¹⁴³, and acts as a monocyte/macrophage chemoattractant.

The protein level of Tmem119 and Gal-3 was assessed in CD11b⁺ cells from the tumor-bearing hemispheres by flow cytometry at day 14 post-implantation (**Figure 6.9 c**). Brains were mechanically processed and dissociated enzymatically with DNase I to preserve a Tmem119 surface marker (see Methods). Gal-3 and Tmem119 allowed for the discrimination of two populations: Tmem119⁺Gal-3⁻ (75.2% of cells) and Tmem119⁻Gal-3⁺ (15.0% of cells), whereas the Tmem119⁺Gal-3⁺ population was sparse (**Figure 6.9 c**). Therefore, validating the reliable separation of microglia and monocytes/macrophages with the proposed markers at the protein level.

CD45 was a previously applied marker for the microglia (CD45^{lo}) and monocyte/macrophage separation (CD45^{hi}). However, its utility has been criticized due to CD45 upregulation by microglia cells under pathological conditions⁵⁵. Thus, the protein level of Tmem119 and Gal-3 was determined also for the CD11b⁺CD45^{lo} and CD11b⁺CD45^{hi} cells in order to compare these marker candidates with the markers that were used previously. Interestingly, the two methods produced similar separation, as 89.5% of CD11b⁺CD45^{lo} cells were Tmem119⁺ and 83.4% of CD11b⁺CD45^{hi} cells were Gal-3⁺ (**Figure 6.9 c,d**).

Additionally, using the defined pair of microglia (Tmem119⁺) and monocytes/macrophages (Gal-3⁺) markers, spatial localization of those populations was assessed with an immunohistochemistry staining of tumor-bearing brain slices. Tmem119⁺ microglia adopted an ameboid morphology in the tumor proximity and localized abundantly in the peritumoral space and at the tumor edge. Whereas Gal-3⁺ monocytes/macrophages were localized predominantly within the tumor mass (**Figure 6.9 e, Supplementary Figure 5**). This finding confirms that microglia localize mostly in the tumor periphery and monocytes/macrophages occupy the tumor core, which was previously reported^{56,75}.

6.10. MONOCYTE-TO-MACROPHAGE POPULATIONS

The Mo/MΦ population in glioma TME showed substantial heterogeneity that is likely related to the differentiation state, as the top upregulated Mo/MΦ genes encompassed genes typically elevated in monocytes and differentiated macrophages. The high *Ly6c2* expression was found in a large fraction of Mo/MΦ, which could be further divided into *Ly6c2*^{high}*Ccr2*^{high} monocytes (Mo) and *Ly6c2*^{high}*Tgfb1*^{high} monocyte/macrophage intermediate cells (Int) (**Figure 6.10 a,b**). The remaining cells resembled differentiated tissue macrophages (MΦ),

because they lacked the markers of the cytotoxic monocytes (*Ly6c2*, *Ccr2*) and were demarcated by *CD49d* expression, a recently proposed marker of BM-derived GAMs (Figure 6.10 a,b). Thus, three differentiation stages – Mo, Int and MΦ were discriminated within the Mo/MΦ population (Figure 6.10 c).

Notably, the MΦ population expressed *Ccl22* and *Ccl5* genes, encoding chemokines important for T-cell recruitment^{46,47} and *Cd274*, a gene encoding an immune checkpoint protein PD-L1 (Figure 6.10 a,b). Such expression pattern suggests a putative role of these cells in mediating the immunosuppressive response.

The level of PD-L1 protein was examined with flow cytometry. The PD-L1 expression was restricted to the CD11b⁺CD45^{high} population (Figure 6.10 d), thus implying that it is produced by monocytes/macrophages but not microglia (see Figure 6.9 c,d). Additionally, PD-L1

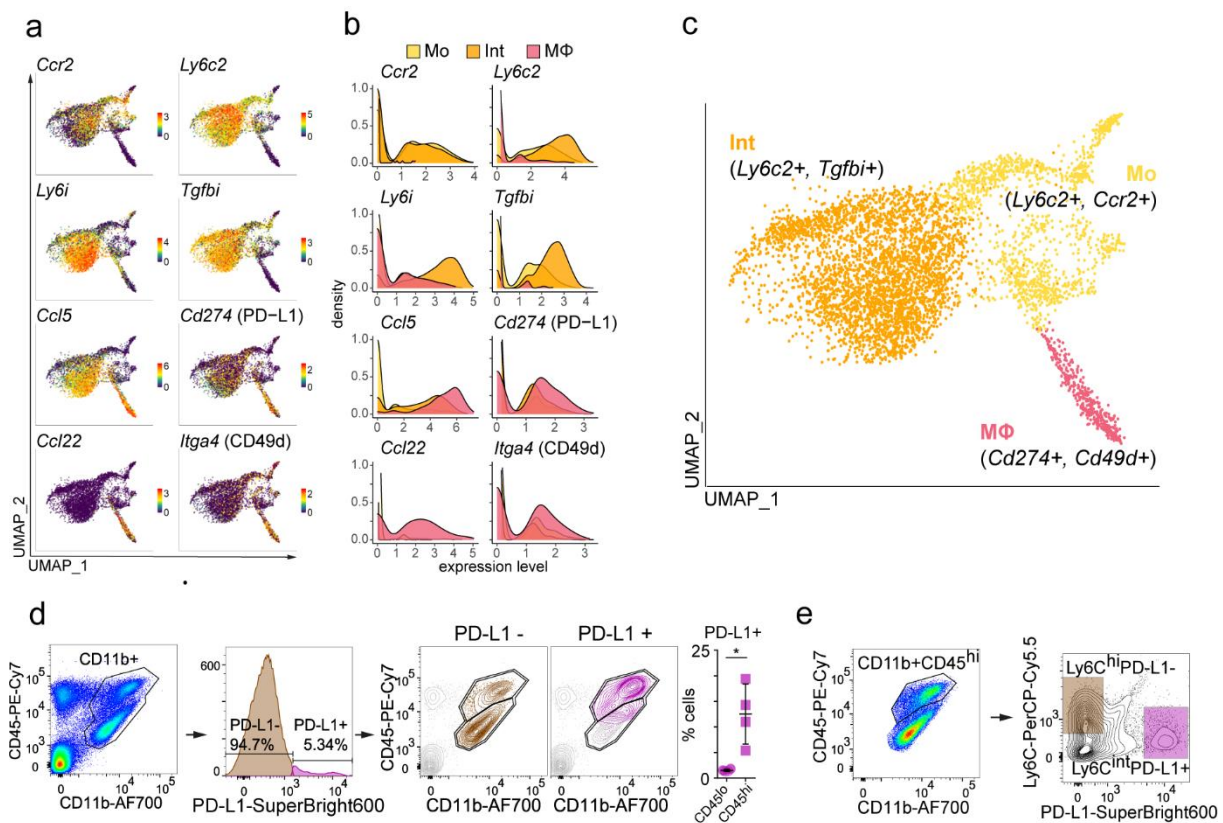


Figure 6.10 | Examination of the monocyte and macrophage populations. (a) Feature plots depicting the distribution of the expression of genes discriminating Monocytes (Mo), Monocyte-Macrophage intermediate (Int), and Macrophage (MΦ) subpopulations. (b) Density plots demonstrating the expression level of markers discriminating the Mo/MΦ subpopulations (Mo, Int, MΦ). (c) UMAP plot shows clusters of Mo/MΦ subpopulations. (d) Flow cytometric analysis of PD-L1 protein within the CD11b⁺ cells and their projection onto CD11b/CD45 graphs, dot plots demonstrate percentages of CD49d⁺ and PD-L1⁺ cells within CD45^{hi} and CD45^{lo} groups (n=4, 2 males and 2 females; two-sided Wilcoxon Rank Sum Test, mean ± SD, *<0.05). (e) Flow cytometric analysis of the distribution of the markers discriminating Mo/MΦ subpopulations within CD11b⁺CD45^{hi} cells, dot plots demonstrate percentage of CD11b⁺CD45^{hi} cells that belong to the defined populations (n=4, 2 males and 2 females; two-sided Wilcoxon Rank Sum Test, mean ± SD *<0.05).

expression was not found in the Ly6C⁺ monocytes (Figure 6.10 e), demonstrating that it is rather produced by the differentiated macrophages.

6.11. ASSESSMENT OF THE PREVIOUSLY PROPOSED MARKERS OF GLIOMA INFILTRATING MONOCYTES/MACROPHAGES

In recent years several reports proposing markers for monocytes/macrophages separation within the brain TME appeared in the field. Thus, we verified the expression of the proposed markers at the single-cell level. Haage et al. 2019 suggested *Hp*, *Emilin2*, and *Sell* based on the meta-analysis of bulk RNA-seq data sets and validated the gene candidates at RNA and protein level. The scRNA-seq analysis presented here, showed that the expression of *Hp* and *Sell* is limited to the Mo cell fraction, whereas *Emilin2* is expressed in Mo and Int groups, but the fraction of expressing cells in those groups is low (Figure 6.11 a). We recently proposed *Tgm2* and *Gpnmb* as universal gene markers of GAMs, based on a critical assessment of bulk RNA expression profiles across glioma animal models (mouse, rat) and human patient-derived samples. At the level of single-cell, the expression *Tgm2* and *Gpnmb* also appeared to be restricted to a fraction of cells, which were found mostly within the Int group (Figure 6.11 b).

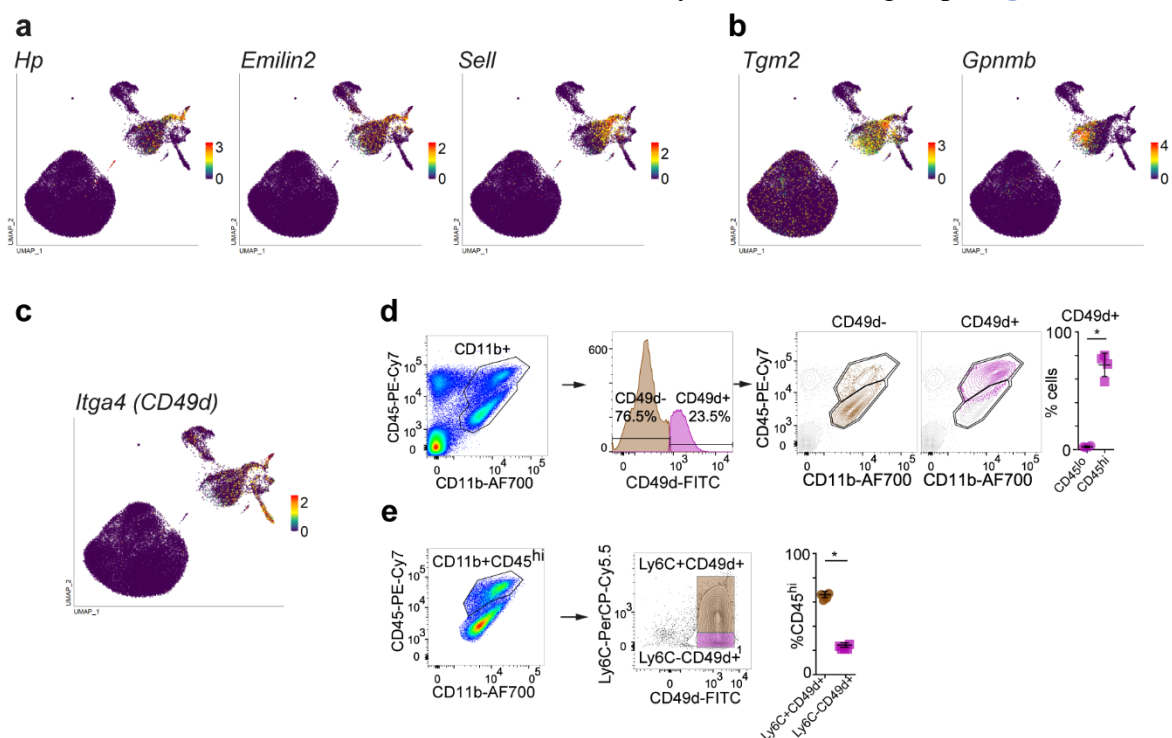


Figure 6.11 | Assessment of previously proposed monocyte/macrophages and GAM markers in the glioma TME. Feature plots demonstrating RNA expression level of marker candidates proposed by (a) Haage et al. (2019), (b) Walentynowicz et al (2018) and (c) Bowman et al (2016). (d) Assessment of CD49d expression in CD11b⁺CD45^{lo} and CD11b⁺CD45^{hi} populations (n=4, 2 males and 2 females two-sided Wilcoxon Rank Sum Test, mean ± SD, *<0.05, Pv=0.0286). (e) Assessment of Ly6C (monocytes) expression within the CD11b⁺CD45^{hi} and CD49d⁺ populations (n=4, 2 males and 2 females; two-sided Wilcoxon Rank Sum Test, mean ± SD *<0.05, Pv=0.0286).

Those results demonstrate how bulk RNA-seq can be biased by genes that although expressed at the high level, are found only in a subset of cells.

On the other hand, the RNA level not necessarily corresponds to the protein level. Bowman et al. (2016) showed that *Itga4* encoding CD49d is specifically repressed by microglia, while being expressed on the surface of BM-derived infiltrating monocytes and macrophages^{59,60}. Here, it was found that *Itga4* is expressed by the subset of Mo/MΦ population, especially by the MΦ (**Figure 6.11 c**). However, flow cytometric analysis indicated that the CD49d protein is more abundant than the transcript of the gene encoding for this protein. The CD49d+ cells constituted 72.1% of the CD11b⁺CD45^{hi} population, whereas they were not found in the CD11b⁺CD45^{lo} population (**Figure 6.11 d**). To determine whether the CD49d protein is expressed mainly by the fraction of differentiated macrophages, the CD11b⁺CD45^{hi} cells were assessed for protein expression of Ly6C (demarcating monocytes) and CD49d (**Figure 6.11 e**). The CD49d+ cells were found to consist of both monocytes (Ly6C⁺, 66.2%) and differentiated macrophages (Ly6C⁻, 24.5%). Therefore, these findings demonstrate that the RNA and protein expression pattern of *Itga4* (CD49d) are not concordant and that CD49d might indeed be expressed on the surface of both monocytes and differentiated macrophages.

6.12. TRANSCRIPTIONAL NETWORKS EXPRESSED BY GAMs ARE MORE PRONOUNCED IN THE INFILTRATING MONOCYTES/MACROPHAGES

Microglia and monocytes/macrophages showed distinct transcriptional signatures informing about their cell type. Still, a distinct cell type does not necessarily imply a distinct function. Thus, the transcriptional networks activated by MG and Mo/MΦ in TME were examined to elucidate their roles in supporting the growth of glioma.

First, differential expression (DE) analysis was performed for Act-MG compared to Hom-MG to extract genes that are induced by the tumor in microglial cells. Next, the DE analysis was performed for Mo/MΦ compared to Act-MG, the sets of obtained genes were compared between groups and analyzed functionally with the Gene Ontology analysis (GO) (**Figure 6.12 a**). Act-MG showed significant induction of 156 genes in the glioma TME. Importantly, the majority of those genes (93) were expressed by Mo/MΦ at a significantly higher level than in Act-MG (**Figure 6.12 b**). Whereas Mo/MΦ showed a substantial number of elevated (481) genes that were not found to be upregulated in Act-MG. The commonly induced genes included genes of the interferon pathway: *Stat1* (Signal Transducer and Activator

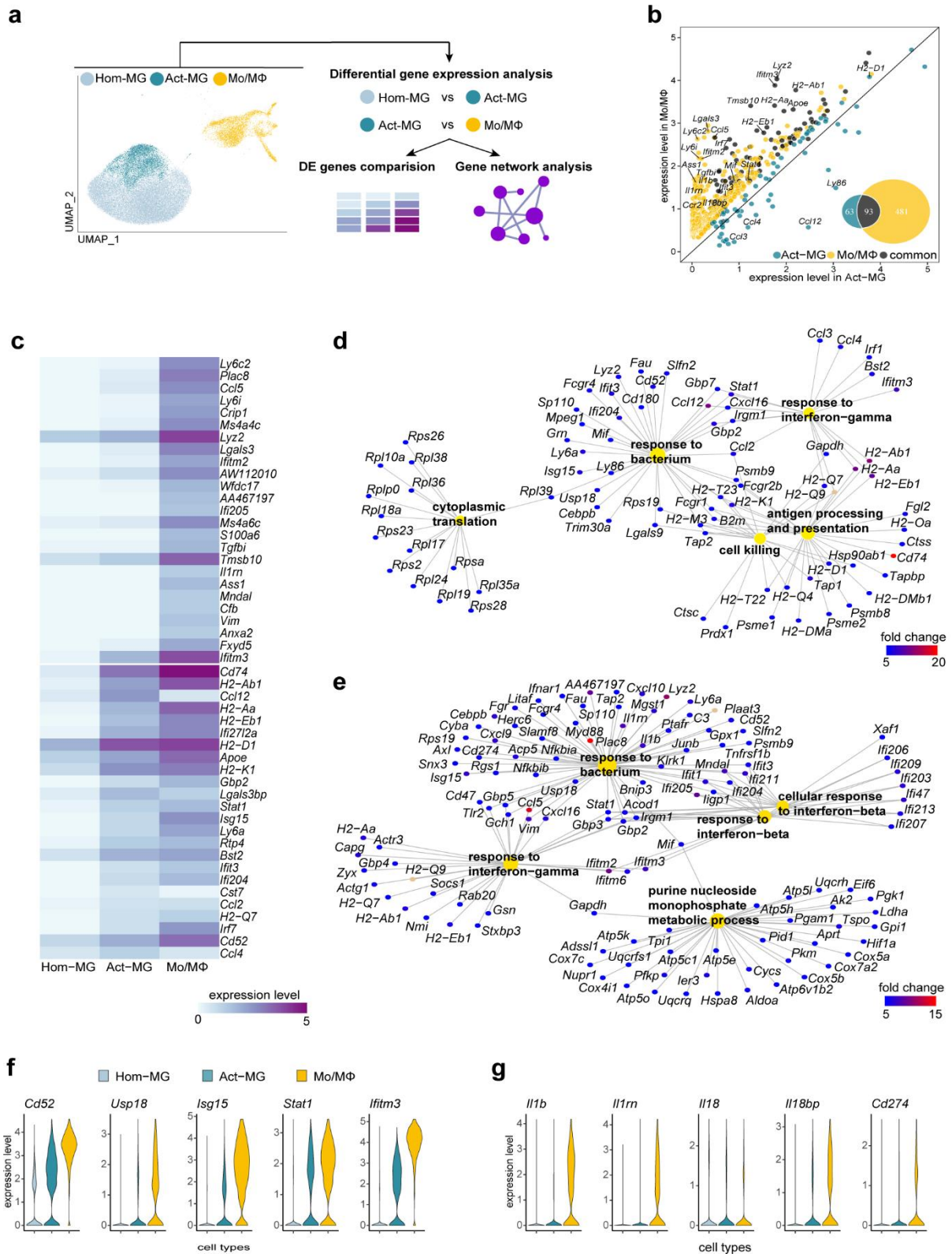


Figure 6.12 | Functional analysis of transcriptional networks expressed by microglia and monocytes/macrophages in glioma microenvironment. (a) Scheme of the analytical approach. (b) Scatter plot depicting expression level of differentially upregulated genes in Act-MG and Mo/MΦ. (c) Heatmap showing the comparison of expression of top 25 upregulated genes in Hom-MG vs Act-MG and Act-MG vs Mo/MΦ. Gene Ontology analysis of biological processes for genes upregulated in (d) Act-MG compared to Hom-MG and (e) Mo/MΦ compared to the Act-MG. (f, g) Expression level of selected genes expressed specifically in distinct subpopulations

of Transcription 1), *Ifitm3* (Interferon Inducible Transmembrane Protein 3), *Irf7* (interferon regulatory factor 7); and genes encoding major histocompatibility complex (MHC) II components: *H2-Aa*, *H2-Ab1*, *H2-D1*, *H2-K1*. Act-MG showed specific upregulation of cytokine encoding genes: *Ccl2*, *Ccl3*, *Ccl4*, *Ccl12*, which are involved in the recruitment of e.g. monocytes, T-cells, and NK cells ¹³⁸. Accordingly, *Ccr2* – a gene encoding a receptor for Ccl2 cytokine, was specifically expressed in the Mo/MΦ group, pointing to the capability of microglia to attract monocytes to the site of tumorigenesis (**Figure 6.12 b, c**).

Next, the GO analysis of biological processes was performed on the two sets of genes – genes significantly upregulated in Act-MG compared to Hom-MG (**Figure 6.12 d**) and genes significantly upregulated in Mo/MΦ compared to the Act-MG (**Figure 6.12 e**). The analysis indicated enrichment of terms directly related to the immune function and largely shared between Act-MG and Mo/MΦ, consisting of “response to bacterium” and “response to interferon-gamma”. However, those terms encompassed a broader number of genes for Mo/MΦ. In addition, the Mo/MΦ population showed enrichment of other interferon-related terms, connected with the response to interferon-beta (“response to interferon-beta”, “cellular response to interferon-beta”). Whereas, the “antigen processing and presentation” term was found only for Act-MG, although many of the genes represented in this term, were also found to be significantly upregulated in Mo/MΦ – *H2-Aa*, *H2-Ab1*, *H2-Eb1*, *H2-Q7*, *H2-Q9*. Other determined terms included “cytoplasmic translation” in Act-MG and “purine monophosphate metabolic process” in Mo/MΦ.

Several shared genes (*Cd52*, *Stat1*, *Isg15*, and *Usp18*) were expressed at a higher level in Mo/MΦ compared to their levels in Act-MG (**Figure 6.12 f**). Proteins encoded by those genes are involved in immune responses: CD52 mediates co-stimulatory signals for T-cell activation and proliferation ¹³⁹; *Stat1* is a mediator of interferon signaling; *Isg15* stabilizes *Stat1* preventing premature termination of an inflammatory response ¹⁴⁰; *Usp18* negatively regulates *Stat1* expression and termination of interferon-induced genes ¹⁴¹. Such expression patterns may indicate that both microglia and monocytes/macrophages initiate some elements of the immune response, with more prominent activation in monocytes/macrophages. Among genes that were highly expressed in Mo/MΦ, we found *Il1b* coding for an inflammatory cytokine IL-1β along with *Il1rn* and *Il18b* coding for the inhibitors of pro-inflammatory cytokines (**Figure 6.12 g**). These data, together with the high expression of *Cd274* coding for PD-L1 in Mo/MΦ, suggest stronger activation of immunosuppressive pathways in monocytes/macrophages (**Figure 6.12 g**).

6.13. VERIFICATION OF THE MYELOID CELL POPULATIONS IN THE GLIOMA MICROENVIRONMENT WITH CITE-SEQ

The CITE-seq was performed for CD11b⁺ cells sorted from naïve brains (D0) and tumor-bearing hemispheres at 14 (D14) and 21 (D21) days post-implantation of the GL261 cells. Similarly to the scRNA-seq experiment, the procedure included both male and female animals (**Figure 6.13 a**). Clustering was performed based on RNA expression profiles for combined conditions and the resulting clusters were examined using the protein level and cluster top expressed genes. The cell identity was assigned according to the literature-based immune marker panel (Supplementary Table 1) (**Figure 6.13 b,c**).

In agreement with the scRNA-seq analysis, the major identified cell populations were microglia and monocytes/macrophages. Microglia clusters (MG) expressed the canonical microglia genes (*Tmem119*, *P2ry13*, *Cx3cr1*) and were distinguished by an elevated level of the Tmem119 protein (**Figure 6.13 b,d**). MG could be divided into homeostatic (Hom-MG) and tumor-activated microglia (Act-MG), as indicated by increased expression of the genes previously found to be induced by microglia in the TME in the Act-MG clusters (*Ccl12*, *H2-Aa*, *H2-Ab1*, *H2-Eb1*) (**Figure 6.13 b**).

Monocytes/macrophages (Mo/MΦ) showed high expression of genes observed in this group in the scRNA-seq analysis (*Lgla3*, *Tgfbi*, *Ly6c2*, *Ifitm2*, *S100a6*, *S100a11*) (**Figure 6.13 b**). Interestingly, at the protein level, the Mo/MΦ clusters showed the uniform expression of the CD49d and CD45 protein, whereas the encoding genes *Itga4* and *Ptprc* were expressed only by a fraction of the Mo/MΦ (**Figure 6.13 e**). Thus, demonstrating that the RNA level does not necessarily correspond to the protein level.

In agreement with the scRNA-seq, Mo/MΦ could be further divided into monocytes (Mo; *Ly6c2*^{hi}, *Ccr2*^{hi}), monocytes-to-macrophages intermediate (Int; *Ly6c2*^{hi}, *Ccr2*^{mid}, *Tgfbi*^{hi}, *Ifitm2*^{hi}) and differentiated macrophages (MΦ₁, MΦ₂; *Tgfbi*^{hi}) (**Figure 6.13 c,e,f**). The level of Ly6C protein across Mo/MΦ clusters was consistent with the Mo, Int and MΦ clusters discrimination, as Ly6C was highly elevated in Mo, along with the monocyte gene markers (*Ly6c2*, *Ccr2*, *Vcan*), and decreased toward the clusters of the differentiated macrophages MΦ₁, MΦ₂ (**Figure 6.13 f**).

The CITE-seq analysis indicated also the presence of non-classical Monocytes (*Spn*⁺, *Ace*⁺ *Ear2*⁺; nc-Mo) (**Figure 6.13 g**), which were also found in a recent scRNA-seq study employing the same murine glioma model and human GBM samples ⁷⁷. Interestingly, two

clusters that along with the Mo, Int, and MΦ were demarcated by high CD49d and CD45 protein expression, were demarcated by *Ccr7* expression and the highest level of the MHCII protein (Figure 6.13 h). The CCR7 cytokine receptor is expressed by dendritic cells (DCs) and is involved in one of the most important chemokine systems orchestrating DCs migration from affected tissue to the lymph nodes^{144,145}. DCs are professional antigen presentation cells, capable of expressing a high level of MHCII. Additionally, some CD11b⁺ conventional DCs

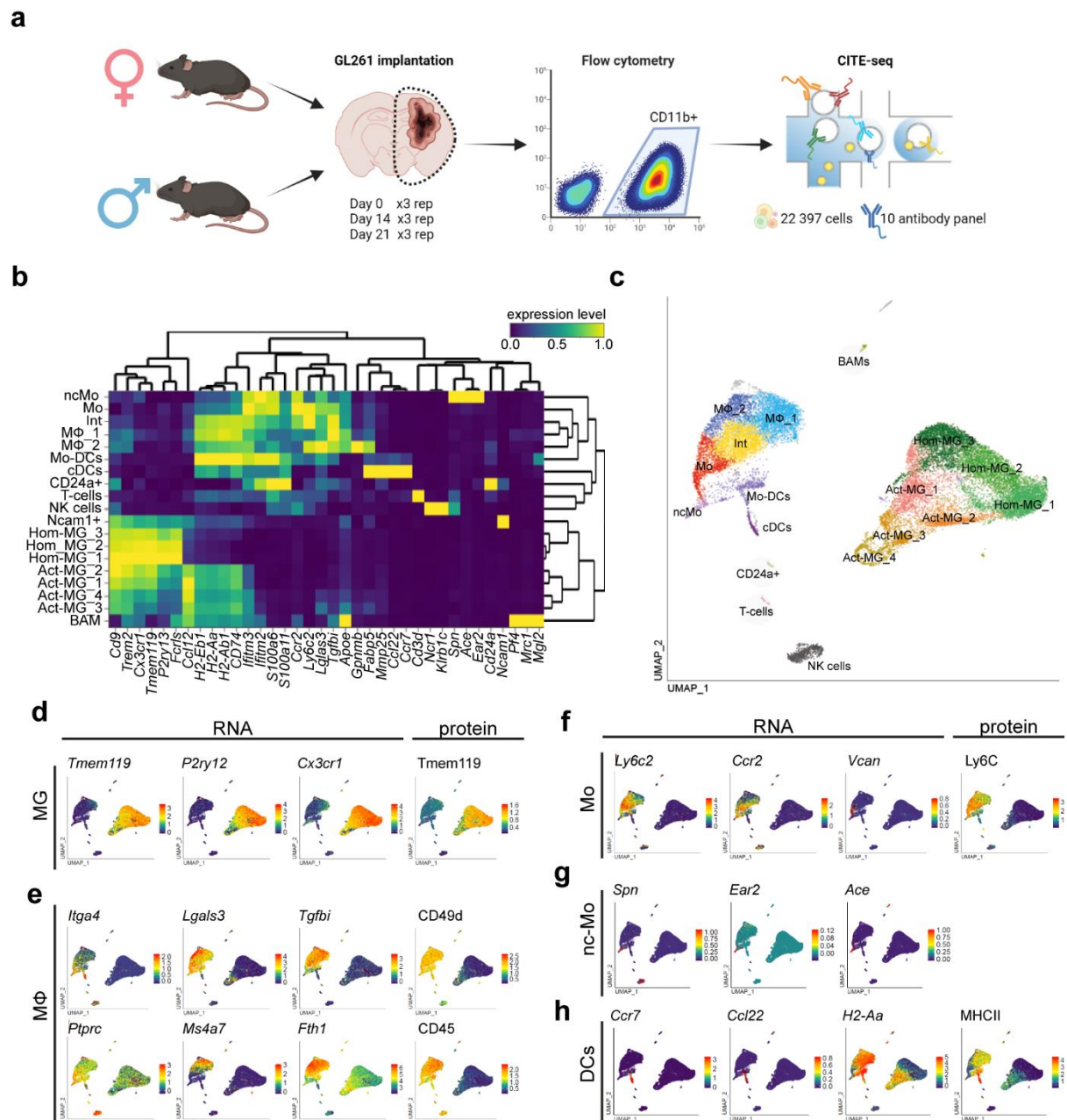


Figure 6.13 | Cell type identification in the CITE-seq data. (a) Schematic representation of the CITE-seq experiment. (b) Heatmap demonstrating the expression level of the genes from the immune marker panel (Supplementary Table 1) in all the defined cell clusters. (c) UMAP demonstrating clusters obtained in a result of graph-based clustering and cell type identification. (d-h) Distribution of the expression level of genes and proteins highly expressed in MG (d), MΦ (e), Mo (f), nc-Mo (g) and DCs (h) cluster.

(cDCs) populations are found to differentiate from monocytes¹⁴⁶. Thus, those clusters assigned as Mo-DCs and cDCs were explored in further analysis (see paragraph 6.18).

The other cell populations identified in the CITE-seq data set were NK cells (*Ncr1*⁺, *Klrbl1c*⁺), T cells (*CD3d*⁺) and BAMs (*Pf4*⁺, *Mrc1*⁺, *Mgl2*⁺). In contrast to the previous analysis, the identified BAM population was very minor. Additionally, two small clusters showed expression of a single cell type marker: *CD24a*⁺ that is expressed by dendritic cells and granulocytes, and *Ncam1*⁺ which is a marker of NK cells (Figure 6.13 c).

6.14. THE PROPORTION OF MAJOR GAM POPULATIONS IN DIFFERENT GLIOMA STAGES

The contribution of the major identified cell populations: Hom-MG, Act-MG, Mo, Int, MΦ, and DCs (DCs + Mo-DCs) was examined within the healthy brain and two murine glioma stages. CD11b⁺ cells derived from naïve brains (D0) consisted mainly of Hom-MG (98.1%) (Figure 6.14 a,b). Whereas, a sparse number of cells was identified as Act-MG (1.4%), indicating an activated state of a small fraction of cells in the normal brain. It is consistent with the fact that microglia continuously survey the brain, reacting to and removing abnormalities to maintain homeostatic conditions. At D14, the number of Hom-MG decreased to 15.1%, whereas Act-MG constituted 35%, and the infiltrating cell populations encompassed 49.9 % of CD11b⁺ cells in glioma TME (Figure 6.14 b). At D21, the CD11b⁺ cells infiltrating from the periphery outnumbered microglia and constituted 68% of the myeloid population.

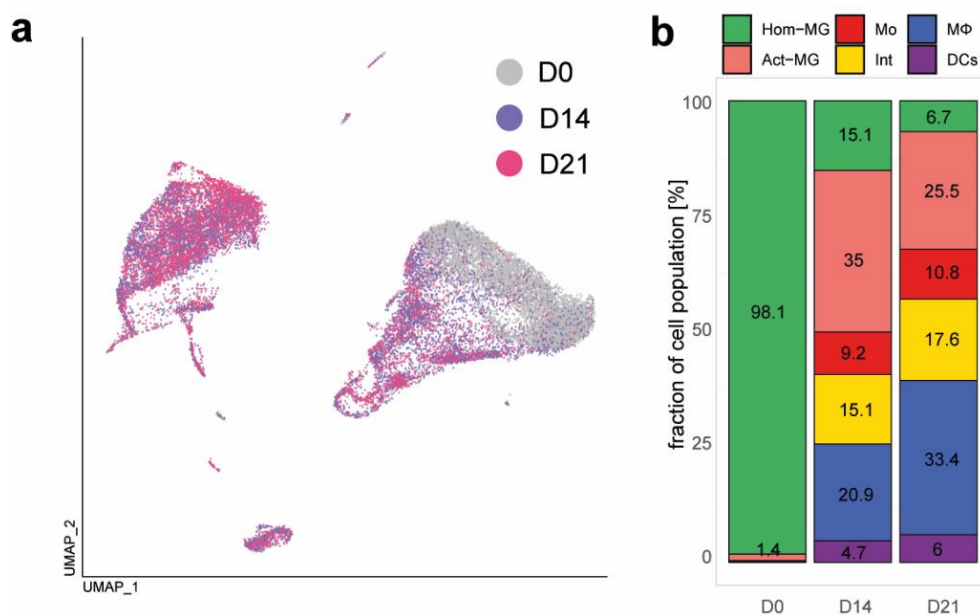


Figure 6.14 | Distribution of cells from each time point across defined populations. (a) UMAP plot showing distribution of cells from D0, D14 and D14 in all CD11b⁺ cells. (b) Stacked bar plot showing proportion of major identified cell population across all time points.

Importantly, out of the infiltrating populations, the MΦ was most abundant at D14 (20.9%) and its number increased at D21 (33.4%), whereas the proportion of Mo (D14= 9.2%, D21=10.8%) and Int (D14= 15.1%, D21=17.6%) appeared to be similar. DCs also constituted similar fraction of CD11b+ cells both at D14 (4.7%) and D21 (6%) (**Figure 6.14 b**). Thus, pointing to a constant inflow of monocytes and accumulation of the differentiated macrophages that outnumber activated microglia in the glioma TME.

6.15. SEPARATION OF THE MAJOR GAM POPULATIONS BY CITE-SEQ PROTEIN MARKERS

Since the MG clusters were demarcated by Tmem119 protein expression, and Mo/MΦ by CD49d and CD45 protein expression, the ability to separate microglia and monocytes/macrophages with those surface proteins was verified. To mimic flow cytometric analysis, the protein level of Tmem119/CD45 and Tmem119/CD49d was visualized with scatter plots (**Figure 6.15**). The Tmem119 was indeed highly expressed by MG, although the fraction of cells from the Act-MG clusters showed lower Tmem119 level that overlapped with the level expressed by the Mo/MΦ and DCs clusters. Still, MG could be separated from the Mo/MΦ and DCs while combining Tmem119 with CD45 or CD49d level. Gates set on the

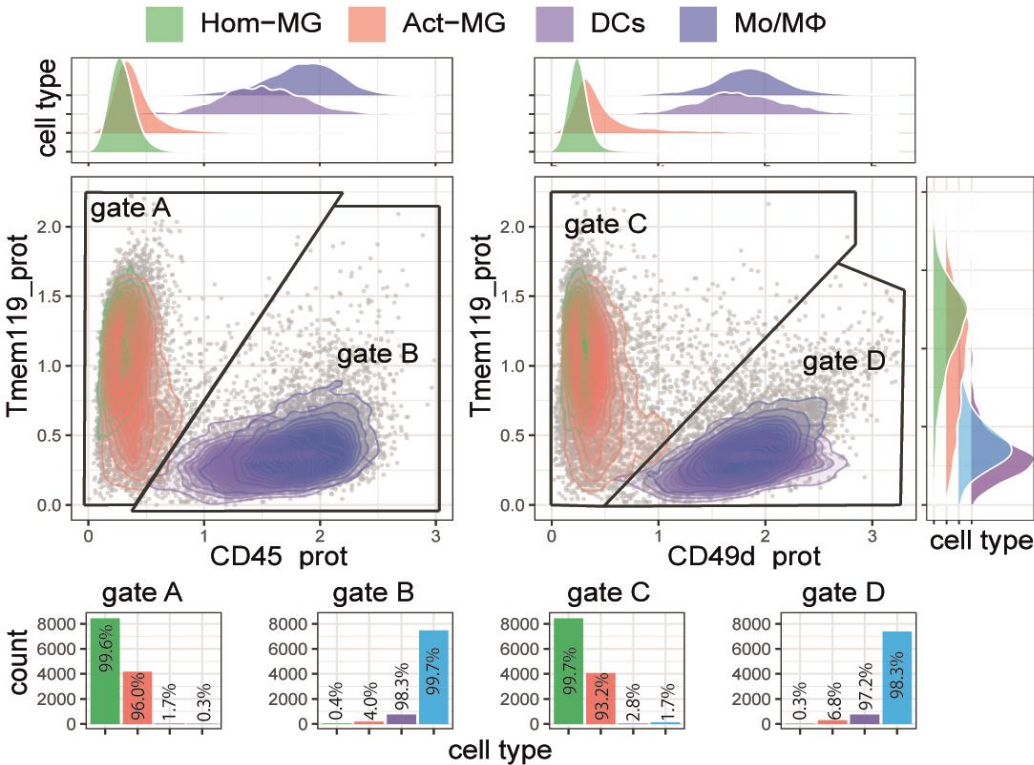


Figure 6.15 | Flow cytometric analysis mimicked with protein expression level from the CITE-seq analysis. Separation of the major identified cell populations with Tmem119/CD45 (left) and Tmem119/CD59d (right). Density plots presented on the top and very right demonstrate distribution of single protein level. Bar plots on the bottom show fraction of cell population within the defined gates. The values inside/above the bars show the percentage of cell from a given population (Hom-MG, Act-MG, DCs, Mo/MΦ) within a given gate.

Tmem119 vs CD45 scatter plot resulted in 99.6 % of Hom-MG and 96.0 % of Act-MG cells in the Tmem119^{hi}CD45^{lo} gate, and 99.7 % of Mo/MΦ and 98.3 % of DCs in the Tmem119^{lo}CD45^{hi} gate. Similar separation was obtained with the Tmem119 and CD49d (**Figure 6.15**).

Therefore, the validity of Tmem119, CD45d, and CD45 surface proteins as markers for the separation of the major populations within the myeloid cells infiltrating glioma was confirmed. Still, the CD49d^{hi}/CD45^{hi} population is very heterogeneous, as it encompasses monocytes, monocytes-to-macrophages intermediate and differentiated macrophages, as well as dendritic cells of myeloid origin.

6.16. FUNCTIONAL STATES OF HOMEOSTATIC AND TUMOR-ACTIVATED MICROGLIA

In order to perform a more in-depth characterization of the transcriptional profiles informing about the cell functional states, the top expressed genes of the clusters were explored (summarized in **Supplementary Figure 6**) in search of functional pathways. Additionally, transcriptional expression patterns identified in a recent scRNA-seq study employing the same murine glioma model⁷⁷ were examined (interferon-related, hypoxic, phagocytosis/lipid metabolism).

Microglial clusters were composed of 3 Hom-MG and 4 Act-MG clusters (**Figure 6.16 a**). Changes in the transcriptional patterns across all the microglial clusters were assessed by identification of highly expressed genes belonging to the same functional group or involved in the same biological process, that were subsequently used to calculate a score (average expression of all genes).

A total of six functional gene groups were defined for the microglial population which is summarized in **Figure 6.16 b**, and the expression level of each gene used for the calculation of the scores is demonstrated in **Supplementary Figure 7**. Homeostatic microglia appeared to exhibit two major transcriptional programs. First program, was characterized by high enrichment of “canonical microglia” genes: *Gpr34*, *Fcrls*, *P2ry12*, *Cx3cr1*, *Selplg*, *Olfml3*, *Tmem119*; and was expressed at the highest level by Hom-MG_1 (**Figure 6.16 a-c**). Second program, showed elevated expression of genes encoding transcription factors and co-activators: *Klf2*, *Klf4*, *Egr1*, *Cited2*, *Fos*, *Fosb*, *Atf3*, *Ier2*, *Jun*, *Junb*. The “transcription factor-related” transcriptional program was enriched predominantly in Hom-MG_3. Interestingly, the cluster Hom_MG-2 did not show specific gene expression, but had mixed expression of the “canonical microglia” and “transcription factor-related” program (**Figure 6.16 a-c**), demonstrating phenotypic spectrum rather than a strict functional specialization.

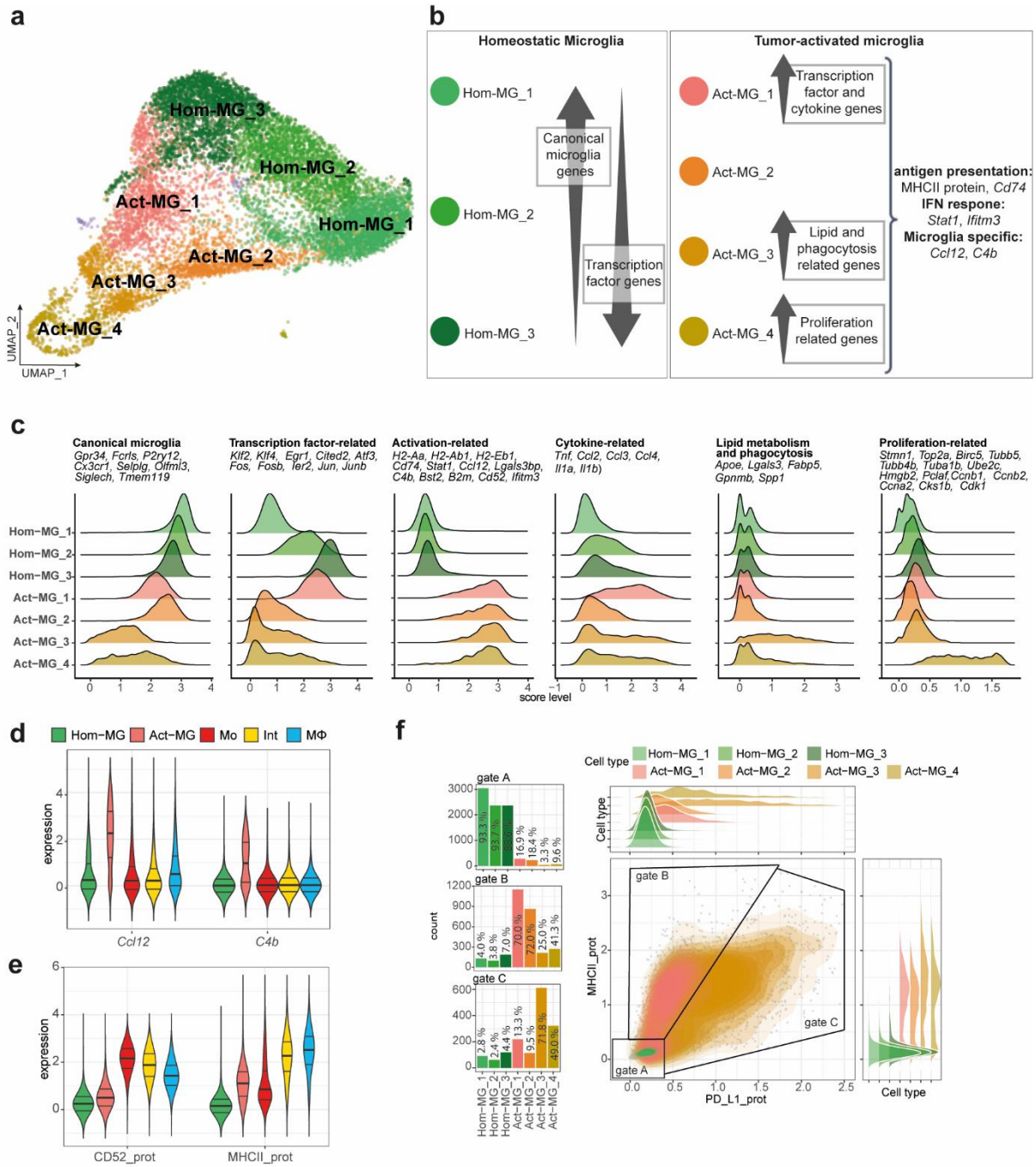


Figure 6.16 | Transcriptional programs of homeostatic and tumor-activated microglia. (a) UMAP demonstrating the microglia clusters. (b) Schematic representation of the transcriptional programs identified in Hom-MG and Act-MG populations. Illustration prepared with BioRender.com (c) Density plot demonstrating distribution of the expression level of scores used to describe each of the transcriptional programs. Scores were computed by calculating an average expression of genes included in the score. The expression levels of individual genes used for the score calculation are given in Supplementary Table 7. (d) Expression level of genes from the “tumor-induced activation” program, that were upregulated specifically by microglial cells from glioma TME. (e) Expression level of proteins from the CITE-seq protein panel, which encoding genes were found in the “tumor-induced activation” transcriptional program. (f) Scatter plot demonstrating separation of the MG subpopulations by MHCII and PD-L1 protein level.

The Act-MG clusters showed uniform upregulation of genes indicating the tumor-induced activation (“activation-related”) compared to Hom-MG clusters (Figure 6.16 c). The tumor-induced activation was evidenced by elevated expression of genes encoding MHC II: *H2-Aa*, *H2-Ab1*, *H2-Eb1* and factors playing a critical role in antigen presentation: *Cd74*, an invariant MHC II chain and chaperone involved in the complex assembly and transport¹⁴⁷, and *B2m* - beta-2 microglobulin, which is a component of the MHC class I complex. The tumor-induced genes included also elements of the interferon (IFN) pathway: a transcription factor involved in IFN-dependent signaling - *Stat1*, interferon induced transmembrane protein - *Ifitm3*, and the interferon inducible protein - *Bst2*; and other genes implicated in immune related functions: *Cd52*, which was found to block the production of inflammatory cytokines via inhibition of the toll-like receptor (TLR) and tumor necrosis factor (TNF) signaling¹³⁹, *Lgals3bp* implicated in cell-cell interaction and binding to Gal-3 that is highly expressed by infiltrating monocytes/macrophages, *Ccl12* encoding a cytokine attracting eosinophils, monocytes, and lymphocytes and *C4b* gene encoding a complement component 4b, being a part of the innate immune response.

Act-MG also exhibited specialized transcriptional programs. Act-MG_1 and a fraction of cells belonging to Act-MG_3 and Act-MG_4 clusters showed elevated expression of the “Cytokine-related” score encompassing: *Ccl2*, *Ccl3* and *Ccl4* genes encoding cytokines involved in the recruitment of monocytes and a variety of other immune cell types including NK, DCs, and T cells; *Il1a* and *Il1b* encoding proinflammatory interleukins, and tumor necrosis factor *Tnf* encoding a multifunctional cytokine involved in differentiation, proliferation and cell survival¹⁴⁸.

Act-MG_3 enriched genes related with “lipid metabolism and phagocytosis”: *Lgals3*, *Fabp5*, *Gpnmb*, and *Spp1*. Lipid-associated macrophages that perform lipid uptake in adipose tissue were found to express a transcriptional signature *Lgals1*, *Lgals3*, *Fabp4*, *Fabp5*, *Lipa*, *Lpl*, *Trem2*¹⁴⁹. Whereas, the *Spp1*⁺*Gpnmb*⁺ microglia cells that express a high level of lysosomal proteins were found in early postnatal brains in the axon tracts of corpus callosum indicating their increased phagocytotic activity^{150,151}. The defined “lipid-metabolism and phagocytosis-related” signature points to the role of those microglia in clearing lipid-rich molecules and debris.

Act-MG_4 showed specific over-expression of “proliferation-related” genes: *Stmn1* associated with microtubule disassembly; *Top2a*, *Hmg2b* and *Pclaf* involved in DNA organization during transcription and replication, *Birc5* blocking apoptotic cell death and

promoting proliferation¹⁵², *Ube2c* ubiquitinase required for the decomposition of mitotic cyclins and cell cycle progression¹⁵³, *Ccnb1*, *Ccnb2*, *Ccna2*, *Cks1b*, *Cdk1* encoding cyclins and cyclin associated proteins and *Tubb*, *Tubb4b*, *Tuba1b* coding for microtubule structural components.

The genes belonging to the “activation-related” transcriptional program were examined in search of the genes specifically induced by microglia and not expressed by monocytes/macrophages. *Ccl12* and *C4b* were found to be expressed at an increased level in Act-MG compared with Hom-MG, and those genes were not found to be expressed in any of the Mo/MΦ clusters (**Figure 6.16 d**). Additionally, the protein panel assessed in the CITE-seq analysis consisted of CD52 and MHCII that are encoded by the genes found in the “activation-related” transcriptional program (*Cd52* and *H2-Aa*, *H2-Ab1*, *H2-Eb1*). The protein expression was consistent with the gene expression pattern, as levels of both CD52 and MHCII were higher in Act-MG compared with Hom-MG (**Figure 6.16 e**). However, level of CD52 and MHCII was lower in Act-MG than in the Mo/MΦ subpopulations.

Therefore, comparing the identified transcriptional programs to the signatures reported by Antunes et al. 2021, the “interferon-related” signature was found as a part of the “activation-related” program, whereas the “lipid metabolism and phagocytosis-related” signature was recapitulated. A presence of the hypoxic signature was not confirmed, as the hypoxic genes were not co-expressed by the same cells but rather distributed over different clusters (**Supplementary Figure 8**).

Hom-MG and Act-MG were found to express distinct transcriptional programs, thus it was examined whether the MG subpopulations can be also distinguished by the protein level, using the CITE-seq protein panel. The MHCII and PD-L1 level best distinguished Hom-MG and Act-MG, and separated some of the Act-MG populations (**Figure 6.16 f**, **Supplementary Figure 9**). A vast majority of the Hom-MG populations were MHCII^{lo}/PD-L1^{lo}. Whereas Act-MG could be divided into MHCII^{hi}/PD-L1^{lo} enriched in cells from Act-MG_1 and Act-MG_2 clusters, and MHCII^{hi}/PD-L1^{hi} that consisted mainly cells from Act-MG_3 and Act-MG_4 clusters. Therefore, demonstrating that the tumor-induced activation of microglia is associated with the elevated level of MHCII protein and that certain subpopulations of microglia cells are capable of inducing expression of an immune checkpoint protein PD-L1 that exerts immunosuppressive properties.

6.17. FUNCTIONAL STATES OF MACROPHAGES IN GLIOMA TME

As described in section 6.13, cells identified as monocytes/macrophages could be divided into clusters expressing genes of non-classical monocytes (nc-Mo)⁷⁷, showing a high level of monocytic gene markers (Mo), demonstrating mixed expression of monocyte and macrophage genes (Int), and two clusters demarcated by expression of genes previously reported for macrophages (MΦ_1 and MΦ_2)^{38,77} (**Figure 6.17 a**). Consistently, Mo showed the highest level of Ly6C protein, which was decreased in Int and MΦ_2 and showed the lowest level in MΦ_1. Whereas, out of the proteins from the CITE-seq protein, the level of PD-L1 protein across the monocyte/macrophage clusters demonstrated an opposite pattern (**Supplementary Figure 9**).

PD-L1 (Programmed death-ligand 1) is one of the best known immune-checkpoint proteins, involved in the suppression of T cell activation and expansion. Evaluation of the Ly6C and PD-L1 levels across monocyte/macrophage clusters demonstrated a gradual decrease of the Ly6C and an increase of the PD-L1 level across the differentiation stages of the Mo-Int-MΦ subpopulations (**Figure 6.17 b**). The Ly6C^{hi} cells showed a low level of PD-L1 and those cells encompassed the vast majority of Mo and a high fraction of Int. Whereas, the cells expressing a high level of PD-L1 are Ly6C^{lo}, and encompass most cells from Int, MΦ_1, and MΦ_2 clusters. These observations point to the fact that monocytes are not capable of immunosuppression via PD-L1, but this property might be adapted during differentiation within the glioma TME.

To assess the transcriptomic profile of the two identified clusters of differentiated macrophages - MΦ_1 and MΦ_2, a differential expression (DE) analysis was performed. Each investigated cluster was compared to all other clusters in the Mo/MΦ and DCs group (**Figure 6.17 c**). The MΦ_1 was found to upregulate *Trem2* and *ApoE*. Trem2 is a triggering receptor expressed on myeloid cells, and the exact identities of its ligands remain unknown¹⁵⁴. However, lipids and lipoprotein complexes were shown to activate Trem2, and Apolipoprotein E (ApoE) is one of the best known Trem2 ligands^{155,156}. Trem2 has been recognized as a factor essential for initiation of the phenotype associated with phagocytosis and lipid metabolism in the disease-associated microglia in Alzheimer disease¹⁵⁷. Additionally, agglomerating evidence points to the tumor-supporting function of Trem2, as the macrophage Trem2 level positively correlated with tumor progression^{158,159}, and Trem2⁺ myeloid cells were shown to efficiently inhibit T cell proliferation *in vitro*¹⁶⁰. The top genes differentially upregulated by MΦ_1 included also genes of the complement system (*C1qa*, *C1qb*, *C1qc*). The complement

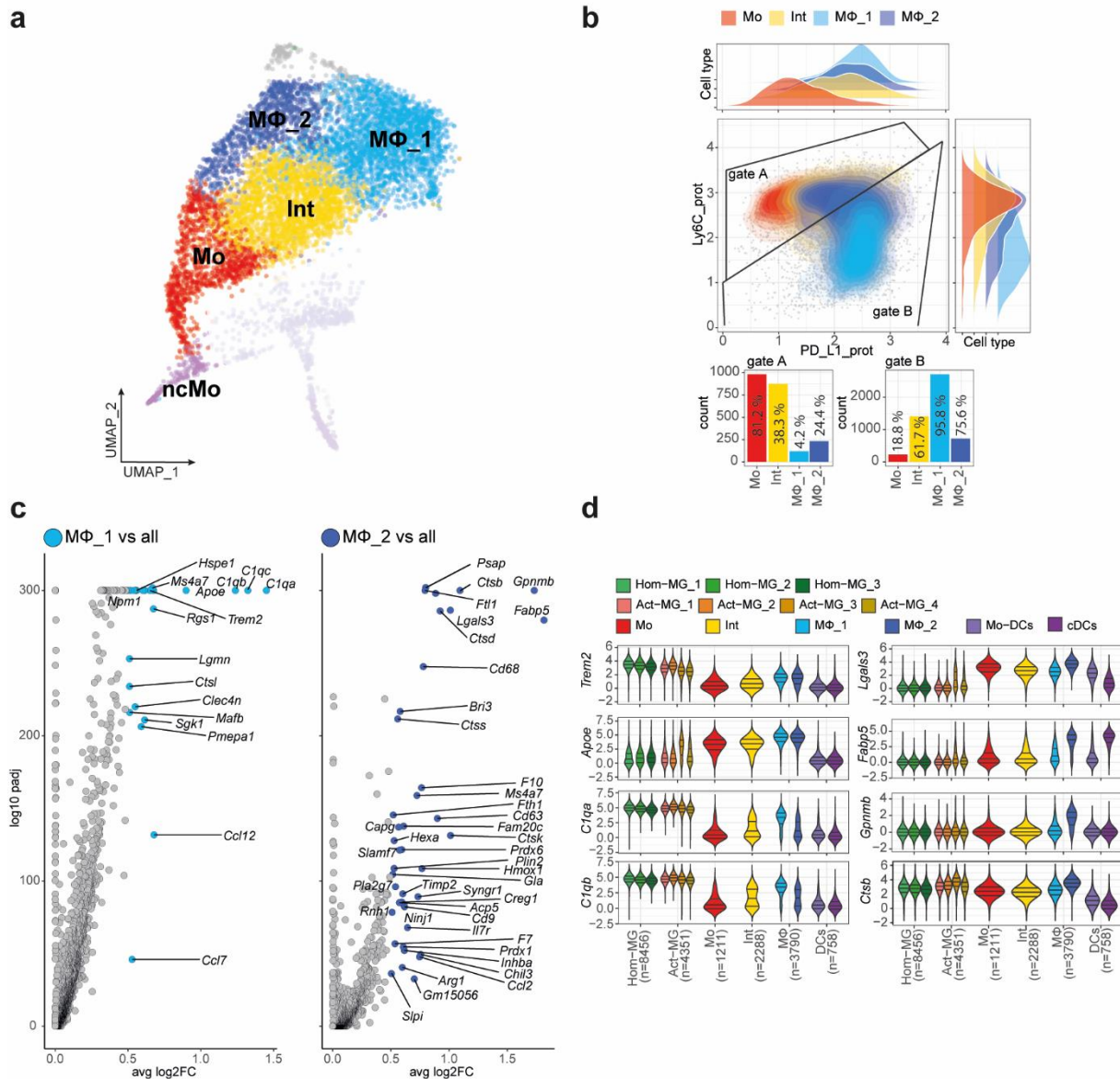


Figure 6.17 | Characterization of monocyte/macrophage subpopulations in glioma TME. (a) UMAP demonstrating the monocytes/macrophages clusters. Clusters described in section 6.17 (Mo-DCs, DCs) are greyed out. (b) Scatter plot demonstrating gradual changes in Ly6C and PD-L1 protein level across monocytes/macrophages in glioma TME. (c) “Half-volcano” plots depicting differentially upregulated genes in MΦ₁ and MΦ₂ clusters in comparison with all other clusters in monocytes/macrophages and DCs groups. Blue dots represent significantly upregulated genes (avg log₂FC > 0.5, p_{adj} < 0.05), and grey dots genes that did not pass the significance threshold. (d) Violin plots demonstrating expression level of selected differentially expressed genes in MΦ₁ (left) and MΦ₂ (right) in comparison to other identified cell populations.

system is a part of innate immunity, directed against pathogenic intruders and “non-self” cells that is involved in both eliciting inflammatory responses and preventing autoimmunity. The C1q-polarized macrophages and DCs were shown to enhance the production of anti-inflammatory interleukins IL-27 and IL-10, as well as upregulate the immune checkpoint proteins PD-L1 and PD-L2 and suppress induction of Th1 and Th17 proliferation^{161,162}.

The MΦ₂ macrophages upregulated *Lgals3*, *Fabp5*, *Gpnmb* - genes found in the “lipid metabolism and phagocytosis” transcriptional program enhanced by Act-MG₃, *CD9* gene found to be involved in immunosuppression, and genes encoding lysosomal hydrolases: *Ctss*, *Ctsb*, *Ctsd* (Figure 6.17 c).

Next, the expression level of the identified differentially expressed genes from two functional groups: “immunosuppression and support of tumor growth” - *Trem2*, *ApoE*, *Clqa*, *Clqb*; “lipid metabolism and phagocytosis” - *Lgals3*, *Fabp5*, *Gpnmb*, *Ctsb*; was assessed across all cell clusters (Figure 6.17 c). *Trem2*, *ApoE* were upregulated by both MΦ₁ and MΦ₂, whereas *Clqa* and *Clqb* was elevated only by MΦ₁ out of the infiltrating monocytes/macrophage population. Interestingly *Trem2* and *Clqa* were also highly upregulated by Hom-MG and Act-MG, pointing to their function under homeostatic conditions. In contrast, the “lipid metabolism and phagocytosis-related” signature was most pronounced in the MΦ₂, although the *Lgals3* expression was observed in all clusters of monocytes/macrophages group as well as in Mo-DCs (Figure 6.17 c).

Therefore, both clusters of the differentiated macrophages were found to express transcriptional patterns indicative of immunosuppressive properties. Whereas MΦ₂ showed also upregulation of the “lipid-metabolism and phagocytosis” genes, found also for Act-MG-3 cluster, although at lower level.

6.18. MONOCYTE-DERIVED DENDRITIC CELLS AMONG CD11b⁺ CELLS IN GLIOMA TME

The CITE-seq analysis was performed on FACS sorted of CD11b⁺ cells. CD11b is expressed on several subsets of dendritic cells¹⁴⁶. As mentioned in section 6.13, among cell clusters of infiltrating monocytes/macrophages (demarcated by a high level of the CD49d protein), clusters showing high level of *Ccr7* gene expression and MHCII protein were identified. Such expression pattern pointed to the possibility that the two clusters should be assigned as DCs (Figure 6.18 a).

Indeed, the two clusters showed distinctive expression of *Btla*, *Kit*, and *Dpp4* (Figure 6.18 b) genes that are found to be expressed across subsets of classical DCs (cDC)¹⁴⁶. One of the clusters was demarcated by an increased expression of *Fcgr1*, *Itgax*, and Ly6C protein that were found to reliably distinguish monocyte-derived DCs from conventional CD11b⁺ DCs (Figure 6.18c)^{163,164}. Whereas, the other cluster was demarcated by an increased expression of *Cd83* gene encoding a marker of mature dendritic cells, *Ly75* encoding CD209

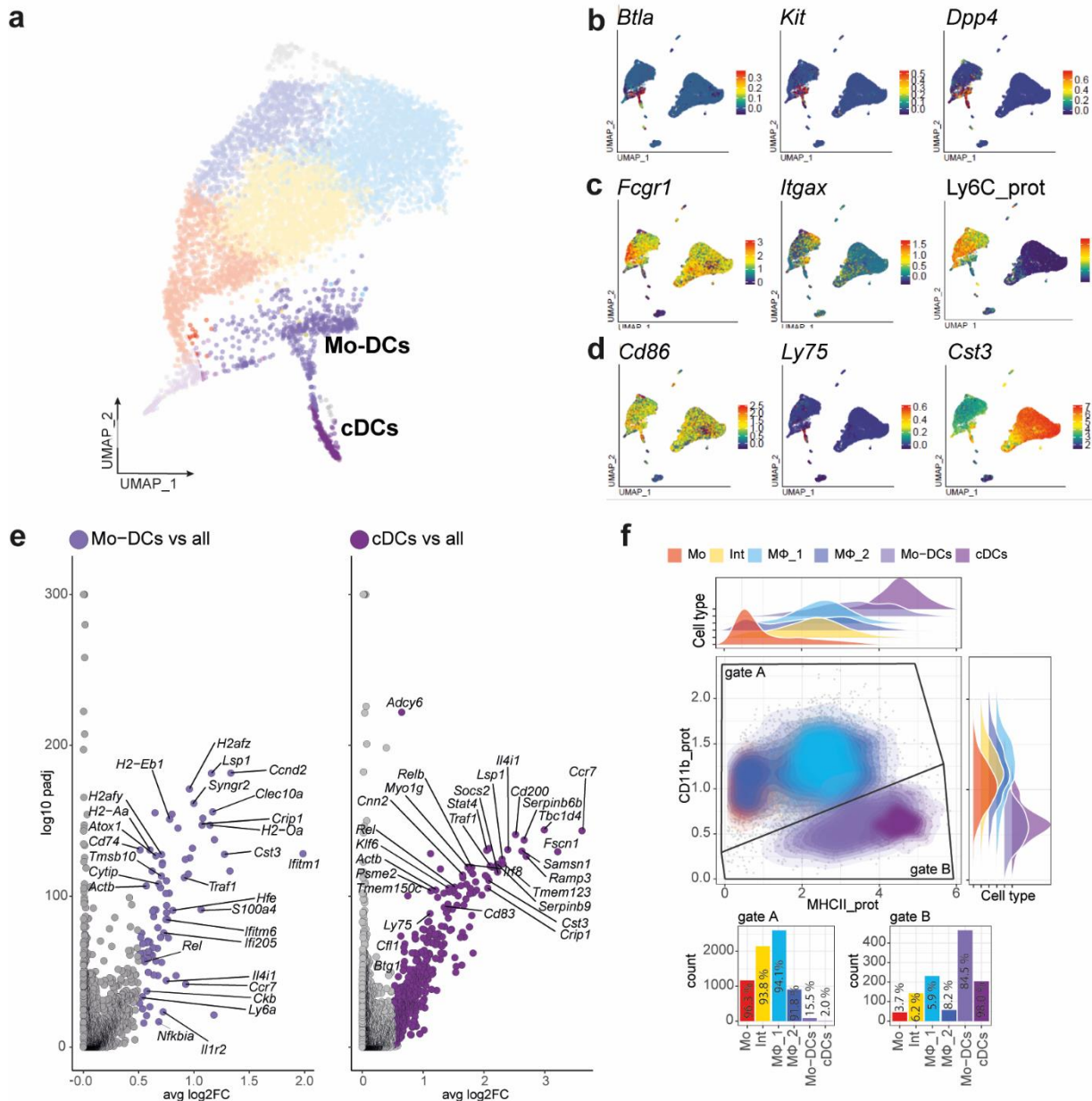


Figure 6.18 | Identification of monocyte-derived dendritic cells among CD11b+ cells in glioma TME. (a) UMAP plot demonstrating the Mo-DCs and DCs clusters. (b-d) Feature plots demonstrating expression level of genes enriched in (b) classical DCs, (c) monocyte-derived DCs (d) mature dendritic cells. (e) in comparison with all other clusters in monocytes/macrophages and DCs groups. Violet dots represent significantly upregulated genes ($\text{avg log}_2\text{FC} > 0.5$, $\text{p}_{\text{adj}} < 0.05$), and grey dots genes that did not pass the significance threshold.

and *Cst3* encoding Cystatin C that are found in conventional DCs including CD11b+ DCs (Figure 6.18d). Thus, those clusters may represent monocyte-derived DCs - Mo-DCs (*Fcgr1*⁺, *Ly6C*⁺) and CD11b+ conventional DCs – cDCs (*Ly75*⁺, *Cst3*⁺).

To determine the functional signatures of Mo-DCs and cDCs, the DE analysis was performed: each investigated cluster was compared to all other clusters in the Mo/MΦ and DCs group. The results were consistent with previous observations. Mo-DCs and cDCs showed

increased expression of the MHCII encoding genes: *H2-Eb1*, *H2-Aa*, *H2-Oa*, and *Cd74* (**Figure 6.18e**). Whereas, the chemokine receptor gene *Ccr7* was the most upregulated gene of the cDCs cluster. CCR7 is expressed by B-cells, subsets of T-cells, and mature DCs and is essential for directing DCs to the lymph nodes. The CCR7 interaction with its ligands (CCL19, CCL21) is one of the most important chemokine systems orchestrating DCs migration from affected tissue to the lymph nodes^{144,145}. Additionally, cDCs upregulated *Irf8* (Interferon Regulatory Factor-8), which is essential for the development of monocytes, plasmacytoid DCs, and type I conventional DCs and remains at a high level in the differentiated DCs¹⁶⁵, and *Stat4* (Signal transducer and activator of transcription 4) that is induced in DCs during maturation¹⁶⁶. Interestingly, Mo-DCs upregulated the interferon-response genes: *Ifitm1*, *Ifitm6*, *Ifi205* and *Ii4i1* that was not observed for the cDCs cluster (**Figure 6.18 e**).

To verify, whether the observed high level of MHCII protein in Mo-DCs and DCs is sufficient to discriminate those cells from the monocyte/macrophages, the flow cytometric analysis was mimicked with the use of MHCII and CD11b proteins from the CITE-seq protein panel. The level of MHCII indeed separated DCs from Mo, Int, and MΦ_{1/2} clusters. However, the MHCII level in Mo-DCs showed overlap with the Int and MΦ_{1/2} clusters. CD11b was found to be expressed in both Mo-DCs and cDCs, although at a lower level than in monocyte/macrophage clusters. Therefore, the combination of CD11b and MHCII protein level allowed separating CD11b^{hi}MHC^{lo/mid} clusters - Mo, Int, MΦ₁ and MΦ₂; from the CD11b^{lo}MHC^{hi} clusters - Mo-DCs and cDCs (**Figure 6.18 f**).

6.19. INTERFERON-RELATED VS TUMOR-SUPPORTIVE EXPRESSION PROFILES

Recent scRNA-seq analysis employing the same murine glioma model reported enrichment of several transcriptional programs (hypoxic, phagocytosis/lipid metabolism, IFN-related) in microglia and macrophage cells. The hypoxic signature was not recapitulated (**Supplementary Figure 8**), whereas the “lipid metabolism and phagocytosis” transcriptional program was identified in MΦ₂ in the DE analysis (section 6.16).

To perform a systematic analysis of the “IFN-related” signaling, the IFN response genes reported for microglia and macrophages were downloaded from the INTERFEROME database¹²⁵ (see Methods). Out of the 467 genes, which upregulation was reported to be induced by interferons in monocytes, macrophages or microglia, 453 were found to be expressed in the CITE-seq data set. Next, the 50 top expressed IFN-response genes were used for hierarchical clustering of cells from MG, Mo/MΦ, and DCs groups (**Figure 6.19 a**).

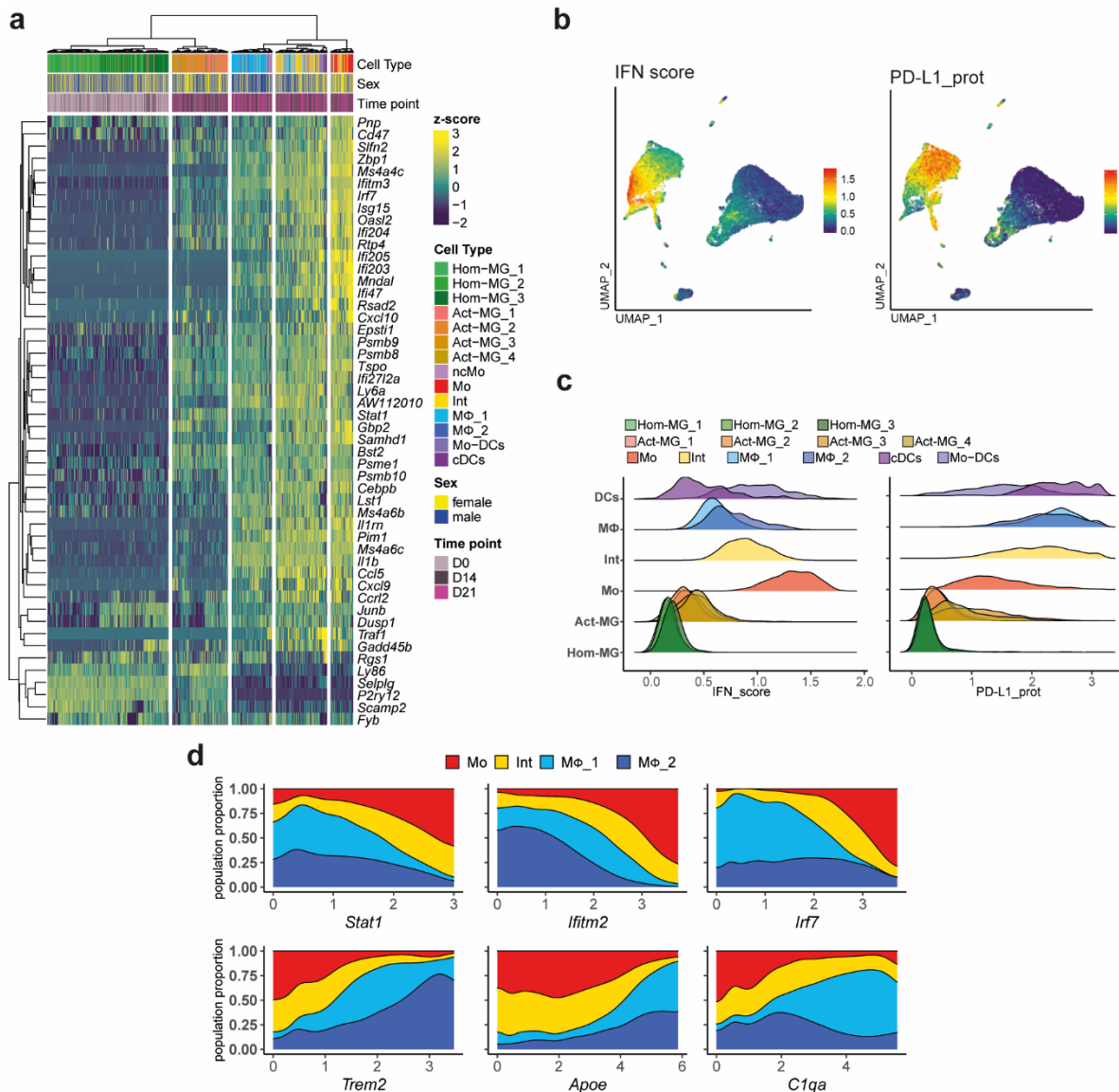


Figure 6.19 | Interferon-related vs tumor-supportive expression profile (a) Heatmap demonstrating expression pattern of the IFN-response genes (for genes selection see Methods). The dendrograms were generated with the ward.D2 method and ordered by a minimum distance. (b-c) Distribution of the IFN score and PD-L1 protein expression level on feature plots in all analyzed CD11b+ cells (b) and density plots across the major identified clusters (c). (d) Filled density plots of genes from “IFN-related signaling” (upper panel) and “immunosuppression and support of tumor growth” gene signatures (lower panel) showing gradual changes in proportion of Mo/MΦ cell clusters along increasing gene expression.

The hierarchical clustering organized cells from low-IFN-response to high-IFN-response expressing cells, in groups overlapping with the previously defined cell identities – Hom-MG, Act-MG, MΦ, Int, DCs, Mo. Thus demonstrating that the IFN-response genes were expressed at the lowest level in Hom-MG and increased in Act-MG. Whereas among the clusters of infiltrating cells, Mo showed the highest level of the IFN-response genes and their expression decreased gradually through DCs and Int to MΦ clusters. Next, the IFN score was calculated by averaging the expression level of genes encoding proteins belonging to interferon-induced transmembrane (IFITM), interferon response factor (IRF), and interferon-inducible (IFI)

protein families (for the full gene list see Methods). The IFN score expression pattern was consistent with the results of hierarchical clustering of the IFN-response genes. The score was the highest in Mo, and decreased gradually through Int to MΦ cluster (**Figure 6.19 b-c**). Similarly, a gradual decrease was noted comparing Mo-DCs and cDCs groups. In MG, the IFN score was elevated in Act-MG compared to Hom-MG and was most pronounced in Act-MG_3 and Act-MG_4. Still, the IFN score in Act-MG clusters was lower compared with all clusters from the Mo/MΦ group (**Figure 6.19 c**).

Interestingly, the distribution of the PD-L1 protein expression showed a pattern opposite to the IFN score – PD-L1 level was the lowest in Mo and the highest in MΦ and cDCs (**Figure 6.19 b-c**). Therefore, we examined whether the downregulation of the “IFN-related” signaling is associated with an increased expression of the genes involved in “immunosuppression and support of tumor growth” across monocyte-to-macrophage cell clusters. The distribution of cells from Mo, Int, MΦ_1 and MΦ_2 clusters was plotted along the expression level of *Stat1*, *Ifitm2*, and *Irf7* genes from “IFN-related” and *Trem2*, *Apoe* and *C1qa* from “immunosuppression and support of tumor growth” transcriptional program (**Figure 6.19d**). Indeed, the proportion of Mo increased towards increasing expression of *Stat1*, *Ifitm2*, and *Irf7*, suggesting that Mo is a major population expressing the “IFN-related” transcriptional program. In contrast, the MΦ_1 and MΦ_2 frequency increased along with an increasing expression of *Trem2*, *Apoe* and *C1qa*.

Such an expression pattern supports the notion that the monocyte-to-macrophage transition can be associated with profound changes in the expressed transcriptional program, reflected in diminished IFN-related signaling and enhanced tumor-supportive phenotype.

6.20. SEX DIFFERENCES IN MHCII EXPRESSION

Sex is an important prognostic marker in GBM patients influencing the incidence and disease outcomes⁸³. In this study, both scRNA-seq and CITE-seq were performed on male and female animals. The unsupervised cell clustering of scRNA-seq showed sex-dependent cell grouping in clusters composed mostly of the cells from glioma-bearing brains (Act-MG, Mo/MΦ), but not in clusters in which the majority of cells originated from the naïve brains (Hom-MG), pointing to differences in immune cell activation between male and female animals (**Figure 6.20 a**).

To investigate the sex-related differences, we performed a DE analysis on the scRNA-seq dataset and compared the transcriptomic profile across sexes in the Act-MG and

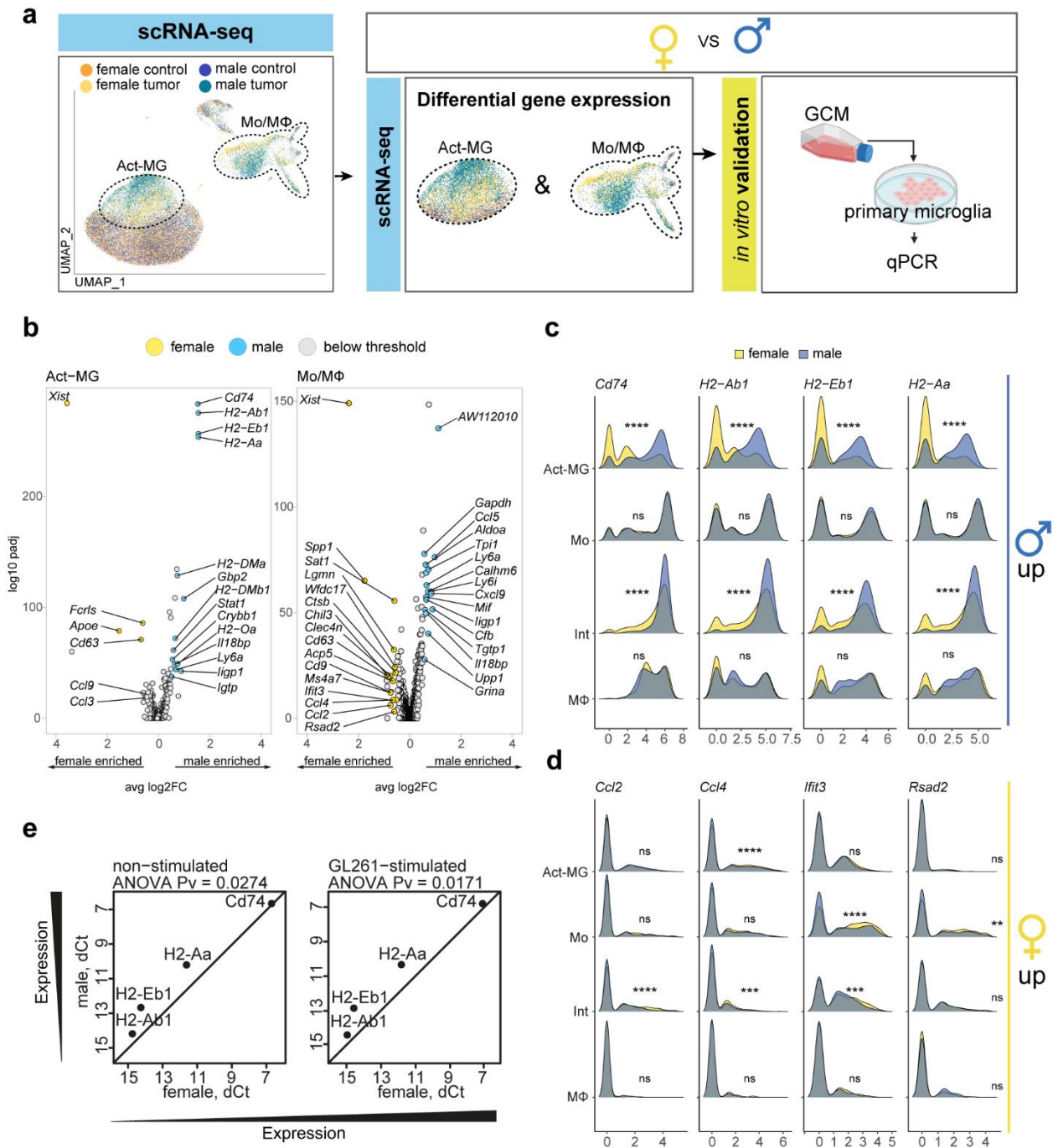


Figure 6.20 | Sex-related differences in MHCII expression (a) Illustration of the analytical approach. UMAP plot demonstrates the distribution of male and female cells across cell clusters, GCM – glioma conditioned medium. (b) Volcano plots depicting the results of DE analysis in the scRNA-seq data set across sexes in Act-MG and Mo/MΦ infiltrating gliomas. (c) Density plots demonstrating expression MHCII encoding genes upregulated genes by male-derived cells. (d) and expression of genes related with migration and IFN, upregulated by the female-derived cells. Kolmogorov-Smirnov test with Bonferroni correction, * $p_{val} \leq 1e-2$, ** $p_{val} \leq 1e-3$, *** $p_{val} \leq 1e-4$, **** $p_{val} \leq 1e-5$. (e) Gene expression analysis of MHCII and *Cd74* genes in murine primary microglia co-cultured with GL261 cells. Gene expression differences determined by qPCR are depicted as dCt with *Actb* as a house keeping gene

Mo/MΦ groups (**Figure 6.20 a**). The DE analysis indicated that male Act-MG highly upregulate *H2-Ab1*, *H2-Eb1*, *H2-Aa* coding for the components of MHCII and *Cd74* – encoding an invariant MHCII chain implicated in folding and trafficking of the MHCII protein (**Figure 6.20 b**). Female-derived cells showed higher expression of e.g. the cytokine encoding genes: *Ccl3*, *Ccl9* (Act-MG) and *Ccl2*, *Ccl4* (Mo/MΦ), as well as *Apoe* (Act-MG) and some of the IFN-related genes *Ifit3*, *Rsad2* (Mo/MΦ). Next, the expression of the selected DE genes was verified within individual subpopulations (**Figure 6.20 c,d**). The MHCII encoding genes showed a profound difference between males and females, not only in the Act-MG population but also in Int and MΦ (**Figure 6.20 c**). Regarding the genes expressed at higher level in female-derived cells, cytokine encoding genes were expressed at a slightly higher level in Act-MG (*Ccl4*) and Int (*Ccl2*, *Ccl4*). Whereas, *Ifit3* showed more profound changes, and more female cells with high *Ifit3* expression were found in Mo and Int subpopulations (**Figure 6.20 d**).

The sex difference in the expression of the MHCII encoding genes was verified in another model: male- and female-derived murine primary microglial cells that were co-cultured with GL261 cells (**Figure 6.20 e**). Expression levels of the selected genes were sex-dependent with higher expression in male- compared to female-derived cultures. Both GL261-stimulated and non-stimulated microglia derived from males showed increased MHCII encoding genes expression, which suggests an intrinsic capability of male microglia to overexpress the MHCII encoding genes that is detectable already in immature microglia.

6.21. MHCII AND IFN-RELATED SIGNATURES IN MALE VS FEMALE

The sex differences in the levels of MHCII and IFN response genes were evaluated in the pre-symptomatic and symptomatic glioma stages in the CITE-seq data set (**Figure 6.21 a**). UMAP showing the distribution of the female- and male-derived cells indicated a sex-directed cell grouping. The monocytic clusters showed the enrichment of female cells, and macrophage clusters of male cells. As has been already shown, the IFN score showed the highest level in Mo, whereas MHCII protein was elevated in DCs and MΦ clusters (**Figure 6.21 a**).

Expression of the MHCII protein is induced by the tumor. However, the dynamics of the MHCII induction differed between the sexes (**Figure 6.21 b**). In males, the MHCII level was high already on day 14 and remained stable on day 21. Contrastingly, females showed low MHCII expression at day 14, and although its level increased on day 21, it was still lower compared with males. The effect was observed both in MG and Mo/Φ (**Figure 6.21 b**). The distribution of the MHCII level across individual GAM subpopulations demonstrated that on

day 14 the sex differences are found in Hom-MG and Act-MG clusters, as well as in the clusters of infiltrating cells – Mo and MΦ₂. At day 21 the difference between sexes diminished due to increased level of MHCII in female cells, which resulted the lack of difference in Mo and MΦ₂, and less pronounced differences in Hom-MG and Act-MG. Importantly, the Hom-MG clusters on days 14 and 21, represent microglia cells that were derived from the tumor-bearing

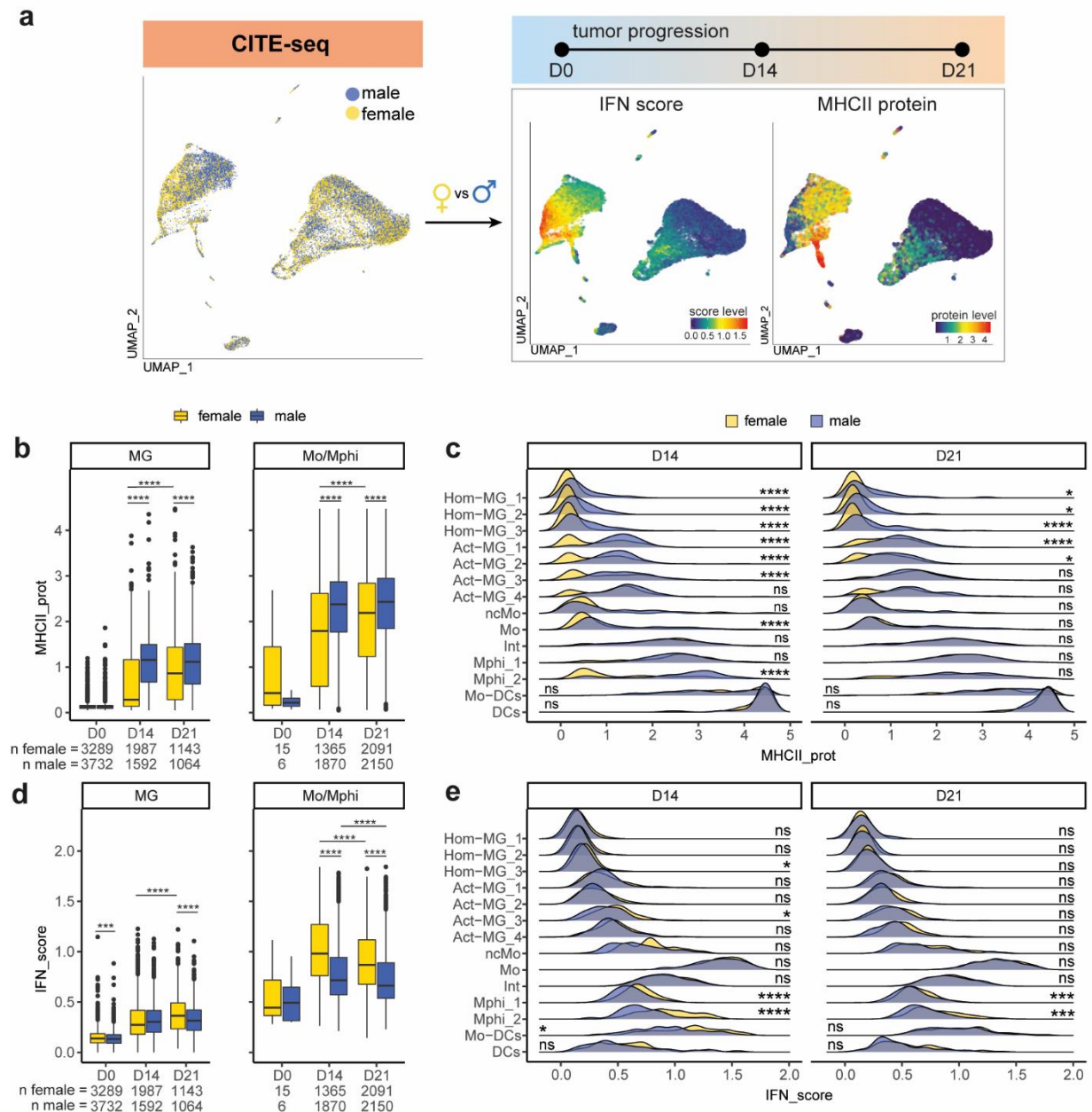


Figure 6.21 | Sex differences in MHCII and IFN response expression. (a) The sex differences were verified in CITEseq data set across two tumor stages. UMAP plots demonstrate the distribution of female- and male-derived cells, and the distribution of MHCII protein expression and IFN score level. (b,d) Boxplots depicting MHCII protein level (b) and IFN score level (d) across sexes and time points. Upper and lower hinges of the boxplots correspond to 25th and 75th percentile respectively, bar in the center represents median value and whiskers range from -1.5 to 1.5 of the *IQR*. Wilcoxon test with Bonferroni correction **** $p_{val} < 1e-5$ (c,e) Density plots demonstrating sex differences in MHCII and IFNscore across individual cell clusters. Kolmogorov-Smirnov test with Bonferroni correction, * $p_{val} \leq 1e-2$, ** $p_{val} \leq 1e-3$, *** $p_{val} \leq 1e-4$, **** $p_{val} \leq 1e-5$.

hemispheres and clustered together with the microglia derived from naïve brains. Hom-MG from D14 and D21 may encompass microglia that did not undergo full tumor-induced activation. The MHCII level in males was induced already in the fraction of cells from Hom-MG clusters and further upregulated in Act-MG. Contrastingly, in female cells the MHCII level was close to zero in Hom-MG clusters both at day 14 and 21; showed binomial distribution in Act-MG at day 14; and in Act-MG reached a similar level to male cells at day 21 (**Figure 6.21 c**). Therefore, suggesting delayed induction of MHCII by females, as compared to male microglia cells in response to the tumor.

The IFN score showed the opposite pattern, as females exhibited higher expression of the IFN response genes. In MG, the IFN score was at the same level on days 14 and 21 in males but increased in females. In Mo/MΦ the tumor-induced expression of the IFN response diminished in time in both sexes, but at both pre-symptomatic and symptomatic stages the female-derived cells showed higher IFN score level (**Figure 6.21 c**). Interestingly, although the IFN response genes were mostly enriched in the monocytic fraction, the sex difference in the IFN score was most pronounced in the clusters of differentiated macrophages - MΦ_1, MΦ_2. Comparing day 14 and 21, the difference between sexes diminished due to a decrease of the IFN score in female cells, although it was still significant in MΦ_1 and MΦ_2.

This observation indicates that the downregulation of the IFN-response genes that is associated with the monocyte-to-macrophage signature changes, might be delayed in females as compared with males.

6.22. SEX-RELATED DIFFERENCES IN GAM PROPORTIONS

As the sex-related differences were found in the IFN-response genes, a transcriptional signature that is enriched mostly in monocytes, we examined the contribution of individual cell types to the GAM population across sexes (**Figure 6.22 a**).

Indeed, the Mo population in females was two times more frequent as compared with males, at both glioma stages (**Figure 6.22 b**). Additionally, males exhibited a substantially higher proportion of MΦ that constituted over 30% of GAMs already at day 14 and their frequency increased to 45% at day 21. The MΦ frequency in females was much lower - 13% at day 14, and 27% at day 21 (**Figure 6.22 b**). To verify this observation, we employed public data sets from single-cell studies on immune cells from human GBM samples that consisted of both male and female patients.. In the CyTOF data set of Friebel et al (2020), the separation of microglia

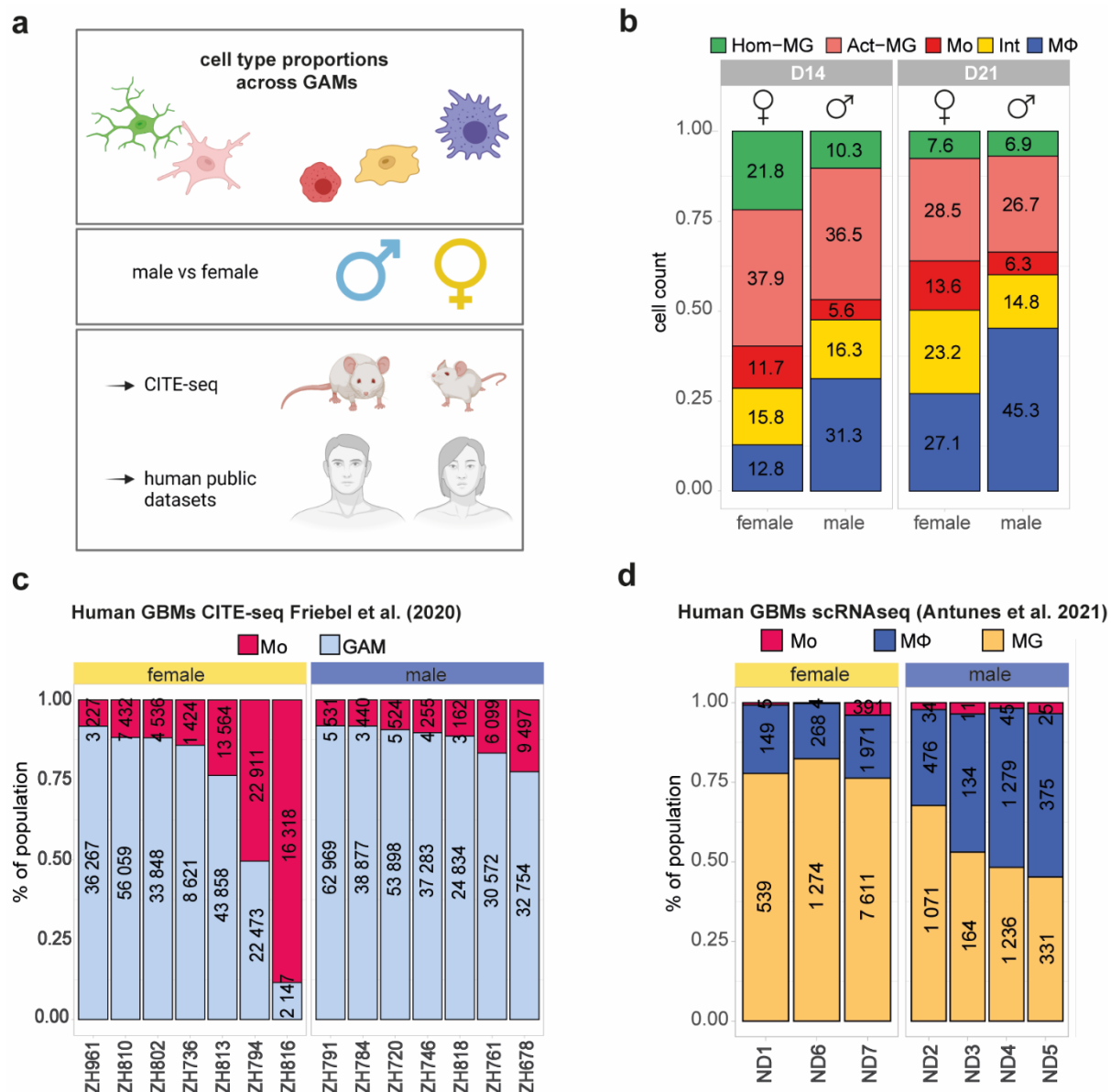


Figure 6.22 | Sex differences in monocyte-associated IFN score and monocyte proportion. (a) The proportions of distinct populations among GAMS across sexes were investigated in the CITE-seq and human public data sets (b) Proportion of the identified cell populations across sexes and time points in the CITE-seq data set (c) Proportion of Mo and GAMs (microglia and macrophages) calculated based on public CyTOF data set from human GBM (n=14) (Friebe et al. 2020). Numbers inside the bars represent a number of cells in each group. (d) Proportion of Mo, MΦ and MG calculated based on public scRNA-seq data set from primary human GBM (n=7) (Antunes et al. 2021). Numbers inside the bars represent number of cells in each group.

and differentiated macrophages was not possible since the authors included the CD49d (macrophage-enriched) in the analysis of only a subset of patient-derived samples. Therefore, the GAM population encompassing both microglia and macrophages was distinguished and compared with the Mo population. The Mo and GAMs proportion was assessed for male (n=7) and female (n=7) derived GBM samples (12 primary, 2 recurrent). The variation across female samples was high. Still, we found that 2 female patients had high Mo frequency, whereas in males the Mo frequency was rather low (Figure 6.22 c). The proportion of cell populations was

also verified for the scRNA-seq data set of Antunes et al. (2021) from primary GBM samples (n=7). The number of Mo identified by the authors was very low, impeding comparisons between sexes. Still, the proportion of M Φ was higher for males, whereas females showed a higher proportion of MG (**Figure 6.22 d**).

Thus, the results obtained from our murine glioma model and public human GBM data sets suggest that the number of monocytes and differentiated macrophages may differ between sexes. However, due to the low number of samples, this observation requires further verification.

7. Discussion

7.1. DISSECTING THE COMPOSITION OF MYELOID INFILTRATES IN GLIOMA TME

One of the important outcomes of this study is a demonstration that the results of scRNA-seq and CITE-seq analyses of the CD11b⁺ cells from naïve and tumor-bearing brains show high reproducibility. However, comparing the results of scRNA-seq and CITE-seq analyses we found that the inclusion of protein markers improves the identification and characterization of cell types, which is particularly important in the case of cells sharing many myeloid markers.

Transcriptomic and proteomic studies of the same cells/tissues showed that the mRNA and protein levels are not always corresponding. In fact, around 50% of expressed mRNA molecules are poorly represented at the protein level⁶⁶. In the present study, the accordance of the transcript and its surface protein level was good for *Tmem119*/Tmem119, *Ly6c2*/Ly6C and *Cd52*/CD52, while there was no such good agreement for *Itgam*/CD11b, *Ptprc*/CD45, *Itga4*/CD49d, *Cd74*/CD74, *H2-Aa*/MHCII, *Cd274*/PD-L1. Therefore, the application of the designed protein panel in the CITE-seq allowed revising the previously proposed protein markers for separation of monocytes, macrophages, and microglia.

Dissecting the CNS resident, microglial GAMs from GAMs infiltrating from the periphery was one of the main goals in this study. We confirmed that Tmem119 demarcated microglia and CD49d was found exclusively on monocytes/macrophages in glioma TME, which is in agreement with previous cell lineage tracing and CyTOF studies^{39,59,61}. Surprisingly, the CD45 level also reliably discriminated monocytes/macrophages from other GAMs in glioma TME, despite prior criticisms and suggestions that CD45 could be upregulated in the activated microglia⁵⁵.

An important finding of this study is that the *Lgals3* and the encoded protein Gal-3 are expressed predominantly in monocytes/macrophages, which was shown with scRNA-seq and confirmed by flow cytometry and IHC analyses. Unfortunately, only the intracellular staining of Gal-3 allowed discriminating monocytes/macrophages from microglia, thus it could not be validated with CITE-seq and antibodies detecting surface markers. Additionally, the high level of MHCII allowed demarcating the subpopulation of dendritic cells in glioma TME that were likely derived from infiltrating monocytes. The application of CITE-seq confirmed the expression of PD-L1 by GAMs and indicated that the differentiated macrophages are the main

source of this immune checkpoint protein in glioma TME, pointing to the important role of this population in immunosuppression.

7.2. THE UNEXPECTED HETEROGENEITY OF MICROGLIA IN THE HEALTHY BRAIN

Microglia are the most abundant immune system cells of the CNS^{167,168}. The predominance of microglia among CD11b⁺ cells has been confirmed in the presented analysis. Under physiological conditions microglia (which we described as homeostatic microglia, **Hom-MG**) exhibit the transcriptional heterogeneity that resulted in the discrimination of the specialized subpopulations. The two major transcriptional programs identified were “**canonical microglia**” with the enriched expression of core microglia genes (*Tmem119*, *Gpr34*, *Fcrls*, *P2ry12*, *Cx3cr1*, *Selplg*, *Olfml3*) and “**transcription factor-related**” showing a high expression level of genes encoding transcription factors and their co-factors (*Klf2*, *Klf4*, *Egr1*, *Cited2*, *Fos*, *Fosb*, *Atf3*, *Ier2*, *Jun*, *Junb*). Interestingly, the defined transcriptional programs showed gradual changes between clusters, and besides these two microglia subpopulations, we found a cluster of microglia that showed an intermediate level of both programs. Thus, pointing to the dynamics of the microglial expression pattern. It is assumed that the variability in transcriptional programs may reflect discrete functional states of microglia. However, we cannot exclude a possibility that the observed transcriptional diversity of microglia reflects differences in microglia origin from various brain structures, as the CD11b⁺ cells were isolated from whole-brain and spatial information was lost due to homogenization.

The previously published deep scRNA-seq study of microglia at different life stages and from various brain regions demonstrated that microglia from adult mice belong to two functional groups characterized by expression of homeostatic microglia genes and immediate response genes¹⁵¹. These defined gene expression patterns largely overlapped with the transcriptional programs determined in our analysis. The authors speculated that the immediate early genes e.g. *Fos* and *Egr1* that are readily upregulated in response to an external stimulus, may be induced by a sorting procedure. Thus, it remains to be determined whether the “transcription factor-related” expression pattern demarcates transcriptionally active microglia predisposed to rapidly react to pathological disturbances or this program is an experimental artifact.

In addition, interesting cell clusters with the characteristics of early and progenitor microglia have been detected. These cells expressed *Csf1*, *Ifit3*, *Mcm5*, *Dab2*, *Cxcr2* genes. CSF1 is a cytokine necessary for microglia maintenance, proliferation, and differentiation.

Whereas CXC chemokine receptor 2 (CXCR2) expressed on microglia may ensure cell mobility in case of a rapid translocation to a damaged site is needed.

The presence of early and progenitor microglia may be a reservoir for self-sustaining cells as microglia do not renew from hemopoietic cells and maintain a stable population during a lifetime. Elmore et al. (2014) reported that pharmacological depletion of microglia with a CSF1R inhibitor triggers the mobilization of dormant microglial progenitors in the CNS allowing rapid repopulation and that the repopulating microglia originated from the proliferation of the latent progenitors ¹⁶⁹.

7.3. MYELOID CELL HETEROGENEITY IN THE GLIOMA MICROENVIRONMENT

The second main aim of this study was to provide functional characteristics of a given myeloid cell type infiltrating the glioma TME. We demonstrate that the presence of tumor cells greatly increases the diversity of myeloid cells in the brain.

First, we found that microglia undergo a tumor-induced activation, giving rise to a population described as activated microglia (**Act-MG**). Act-MG downregulated canonical microglial genes compared with Hom-MG. The phenomenon of reduction of canonical microglia genes has been previously described in the disease-associated microglia in Alzheimer disease ¹⁵⁷. In glioma TME, Act-MG upregulated the genes/proteins involved in “**antigen presentation**” and “**IFN response**”, as well as showed a specific increase of the *Ccl12* and *C4b* gene expression. Microglial cells activated several, specialized transcriptional patterns. As a result, four subpopulations of the tumor-activated microglia were distinguished: Act-MG_1 augmenting the “**transcription factor-related**” program similar to the one found in homeostatic microglia and the “**cytokine-related**” program; Act_MG_2 that showed induced expression of the common Act-MG genes; Act-MG_3 upregulating genes involved in “**lipid metabolism and phagocytosis**” and Act-MG_4 demarcated by the “**proliferation-related**” genes. The identification of microglia (Act-MG_4) expressing the proliferation-related genes (i.e. *Ube2c*, *Top2a*, *Stmn1*, *Ccna2*, *Cdk1*, and *Tubb5*, *Ccnb1*, *Ccnb2*) may indicate the source of those microglia cells. The increase in activated microglia can result from local proliferation, rather than microglia migration from other sites of the CNS. In addition, we found an increased level of PD-L1 in Act-MG that was limited to cells belonging to the Act-MG_3 and Act-MG_4.

Besides the increasing heterogeneity of resident microglia, the tumor-bearing brains showed the profound infiltration of myeloid cells from the periphery. The infiltrating populations encompassed monocytes/macrophages (**Mo/MΦ**), and the monocyte-derived

CD11b⁺ dendritic cells (DCs). The Mo/MΦ population exhibited specialized transcriptional programs that only to some extent overlapped with the tumor-induced expression detected in microglia. The transcriptional patterns common for Act-MG and Mo/MΦ (“**antigen presentation**”, “**IFN-response**”, “**lipid and phagocytosis-related**”) were found to be induced at a substantially higher level in cells from the Mo/MΦ population. Increased expression of the “**antigen presentation**” genes represent a functional activation of myeloid cells that are professional antigen processing and presenting cells in the CNS. Upregulation of “**lipid metabolism and phagocytosis**” transcriptional program likely reflects the increased phagocytic activity of Act-MG and Mo/MΦ that is necessary to remove dying neurons and glial cells, and to modulate the extracellular matrix to facilitate tumor migration and invasion. The increases of the phagocytic properties of microglia have been observed in microglia-glioma co-cultures *in vitro* ^{32,50}.

Additionally, Mo/MΦ and DCs exhibited an enhanced expression of genes characterizing the “**tumor support and immunosuppression**” phenotype, which is reflected by upregulation of genes known to promote glioma progression: *Trem2*, *ApoE*, *Clqa*, *Clqb*, *Cd9*; highly elevated levels of the immunosuppressive factors: the immune checkpoint PD-L1 protein and *Il1rn*, *Il18bp* genes encoding the inhibitors of pro-inflammatory cytokines. TREM2 (triggering receptor expressed on myeloid cells-2) cooperates with CSF-1 in supporting macrophage survival and proliferation ⁸⁰. ApoE (apolipoprotein E) is a ligand of TREM2. *Cd9* encodes the tetraspanin CD9 protein that can interact with other tetraspanins and with different transmembrane and intracellular proteins ¹⁷⁰. The complement system C1q protein is a part of innate immunity and its deficiency is associated with autoimmune diseases ¹⁷¹.

7.4. IDENTIFICATION OF SUBPOPULATIONS REFLECTING MONOCYTE-TO-MACROPHAGE TRANSITION

In this study, thanks to a precise identification of transcriptional programs in the Mo/MΦ infiltrating from the periphery to the tumor, we found transcriptional changes indicative of the monocyte-to-macrophage transition within the glioma TME. Based on gene expression profiles the cell clusters were assigned to three differentiation stages: monocytes (**Mo**), intermediate monocytes/macrophages (**Int**), and differentiated macrophages (**MΦ_1** and **MΦ_2**). Monocytes were likely cells freshly entering the brain parenchyma and retaining their monocytic, immature characteristics.

Our observation of the MDM transition occurring in the glioma TME is consistent with the previous reports on human GBMs and a murine glioma model. Friebel et al. (2020) showed

continuous changes in the expression of monocyte to macrophage protein markers in the CyTOF study on human gliomas and brain metastases ⁷². Antunes et al. (2021) also identified the monocytes, monocyte-to-macrophage intermediates and differentiated macrophages in the scRNA-seq analysis of human GBM samples and GL261 murine gliomas ⁷⁷. The authors found that CCR2 deficiency blocks monocyte recruitment to the glioma microenvironment, resulting in depletion of a vast majority of monocytes and the reduction of the macrophage proportion by about 30%. Still, the number of remaining differentiated macrophages in glioma TME was substantial, pointing to a Ccr2-independent macrophage accumulation. We demonstrated that CD49d is expressed at a similar level in infiltrating MDMs and CD11b⁺ DCs. CD49d is an integrin involved in leukocytes migration to the brain under pathological conditions ¹⁷². Akkari et al (2020) showed that the CD49d blockade inhibited the monocyte recruitment to the glioma TME and reduced the number of differentiated macrophages by half ¹⁷³. This implies alternative mechanisms of the MDM recruitment.

Interestingly, we demonstrated that the monocyte-to-macrophage transition is associated with a switch of the transcriptional program. Monocytes displayed the enrichment of the “IFN-response” transcriptional pattern that diminished in the Int population and was expressed at a low level in the MΦ_{1/2} subpopulations. Whereas the “tumor support and immunosuppression” genes showed the opposite changes, as that program was expressed at a very low level in Mo, increased in Int and showed the highest expression in MΦ_{1/2} subpopulations. The MΦ₂ population was additionally characterized by upregulation of the “lipid metabolism and phagocytosis” transcriptional program. Those transcriptional changes suggest that monocytes in TME are likely cells freshly entering into the brain parenchyma and retaining their monocytic, immature characteristics and expressing many inflammatory genes suggestive of their anti-tumor activity. The anti-tumor activity is gradually lost in the glioma TME, as the signature of differentiated macrophages is associated with increased expression of immunosuppressive factors.

The identified transcriptional patterns in GAMs to some extent overlap with the results of a scRNA-seq study on murine GL261 gliomas and human GBMs ⁷⁷. Antunes et al. (2021) showed the interferon-related and phagocytosis/lipid-related expression patterns that were induced at a higher level in the fraction of MDMs compared with microglia. Additionally, some of the interferon response genes (*Rsad2*, *Cxcl10*) showed the enrichment in monocyte and monocyte-to-macrophage transitory populations. The authors showed the presence of the “hypoxic signature”, which was reported in previous scRNA-seq studies on human GBMs ^{73,76}.

In the present study, the genes of the “hypoxic signature” were not co-expressed by the same cells but rather showed the enrichment across different cell clusters.

7.5. IMPLICATIONS OF THE “INTERFERON-RELATED” GENE EXPRESSION

Type I interferons are cytokines involved in the activation of immune cells in the response to pathogenic stimuli, which may exert anti-tumor action e.g. via induction of the pro-inflammatory activation of macrophages, apoptosis of T_{regs}, or inhibition of angiogenesis¹⁷⁴. Interferons have been considered as potential adjuvants in anti-cancer therapies. However, clinical trials showed minor benefits as compared to the established treatments⁷⁸. Bulk RNA-seq studies identified expression profiles related to the IFN response in human GBMs¹⁷⁵, and an increased “interferon signature” was associated with a worse patient prognosis¹⁷⁶. Such association is surprising, as interferons were shown to exert an anti-tumor effect in multiple studies¹⁷⁴.

Type I interferons induce strong changes in transcription e.g. via enhancing expression of genes encoding interferon-induced transmembrane (IFITM), interferon-induced protein with tetratricopeptide repeats (IFIT), interferon response factor (IRF) families, and other downstream genes. In the present and other studies, the expression of the interferon-response genes was much higher in infiltrating MDMs (or their subpopulations) compared to microglia^{60,77}. The abundance of MDMs was negatively correlated with a patient prognosis in contrast to microglia^{38,55,72}, and the IDH-mut gliomas that are characterized by better survival showed a minor MDM infiltration^{60,72}. Thus, the increased “interferon signature” found in bulk GBM datasets might be in fact an indicator of the increased monocyte infiltration that is associated with the high accumulation of the tumor-supportive macrophages. This issue cannot be resolved employing bulk RNA-seq methods. However, an increasing number of the scRNA-seq data on human gliomas might provide better resolution of the MDM subpopulations and their specific roles in tumor progression.

7.6. THE IMMUNOSUPPRESSIVE ROLE OF DIFFERENTIATED MACROPHAGES

We demonstrate that the populations of differentiated macrophages (MΦ₁, MΦ₂) exhibit the highest level of the immunosuppressive immune checkpoint protein PD-L1 and *Il1rn*, *Il18bp* genes. Additionally, the MΦ populations are characterized by the enriched expression of genes such as *Trem2*, *Apoe*, *Cd9*, *C1qa*, *C1qb*, *Gbnmp*, *Lgals3*, *Fabp5* that recently have been to be implicated in tumor progression.

Expression of *TREM2* was positively correlated with tumor growth, and the protein has been implicated in promoting the immunosuppressive TME⁷⁹. *TREM2* cooperates with CSF-1 in sustaining macrophage survival and proliferation⁸⁰. ApoE is the best documented ligand of *TREM2*⁸¹ and CD9 is recognized as an anti-inflammatory marker of monocytes and macrophages⁸². Expression patterns of the “lipid metabolism and phagocytosis” genes such as *Gpnmb* (*transmembrane Glycoprotein Nmb*), *Lgals3* (*Galectin-3*) and *Fabp5* (*Fatty Acid Binding Protein 5*), suggest their involvement in inflammation, cell-matrix adhesion, and lipid metabolism, respectively.

C1qa and *C1qb* encode chains of the complement component 1q (C1q), a constituent of the classic complement pathway. The balance of the complement system components might be lost in the tumor-bearing organisms¹⁷⁷. C1q deficiency ultimately leads to the development of an autoimmune disease systemic lupus erythematosus (SLE)¹⁷⁸. Stimulation of human peripheral blood mononuclear cells with C1q complexes *in vitro* reduced expression of the IFN-response genes¹⁷¹.

Therefore, the transcriptomic profile of differentiated macrophages, together with the highest level of the immune checkpoint protein PD-L1, suggest a key role of this myeloid population in the induction of the immunosuppressive environment within glioma TME.

7.7. CELL TYPE VERSUS CELL STATE

Cell type identification is one of the challenges in the analysis of the single-cell sequencing data that has a major influence on biological interpretation and for which no standards have been yet established. Cell identities are typically assigned to clusters - groups of cells with similar transcriptomic profiles, obtained as a result of clustering. Clustering is, by definition, an unsupervised method, although the number of obtained cell clusters can be controlled.

The most common approach of cell type annotation is an expert-guided identification, employing cell type marker panels and subsequent exploration of the data in search for genes/proteins characterizing a given cluster or groups of clusters. We have demonstrated in the present study that the same cell type (i.e. microglia) may express distinct transcriptional programs elicited by tumor-induced activation (Hom-MG and Act-MG). We found that activated cells within the tumor microenvironment can, in fact, express several transcriptional programs e.g. Act-MG are enriched in “cytokine-related”, “antigen presentation”, “IFN- response” and “phagocytosis and lipid-related” transcriptional patterns. A variety of the identified transcriptional programs can result from a transient activation of a particular program

or different spatial localization of cells and their exposure to specific stimuli e.g. a tumor edge, tumor core, hypoxia, proximity to blood vessels. Several studies (including ours) demonstrated that myeloid cells exhibit substantial transcriptomic differences depending on their localization/distance to the tumor ^{73,179}. Consistently, the proportion of microglia to macrophages differs between a tumor core and a tumor edge. Thus, it remains to be elucidated to what extent the transcriptional programs of myeloid cells reflect their activation in specific regions of the glioma TME.

The same transcriptional programs can be shared between different cell types, and show gradual changes e.g. we found that the “interferon response” was highly upregulated in Mo and decreased through the Int to the MΦ population, which is consistent with losing the pro-inflammatory phenotype by monocytes and acquiring the immunosuppressive phenotype during maturation of macrophages in the glioma TME. While these phenomena are difficult to be verified in cells isolated from tumor samples, the kinetics of transcriptional changes during tumor progression could be observed in animal models and provides experimental support for monocyte to macrophage transition instructed by tumor-derived stimuli.

Altogether, the acquired results show that a cell type and cell state can be perceived as two layers of information that are not necessarily enclosed in the single-cell clusters. Importantly, cell type might be usually annotated with the use of the established markers, excluding novel populations that have not been yet described. Whereas, cell state is rather a collection of transcriptional changes indicative of functional specialization. As shown in this study, the transcript level does not necessarily correspond to the protein level. Thus, the cell state annotation should rely on a group of functionally similar genes, rather than single gene markers. The application of such strategy could improve the reproducibility between single-cell studies.

7.8. SEX DIFFERENCES IN GAM RESPONSES

Sex differences in tumor incidence (male-to-female ratio of 1.6:1 and 2:1 in mesenchymal GBMs), variations in transcriptomes, and patient outcomes of adult GBM patients have been previously reported ⁸³. Sex-specific disease outcomes can be related to immune functions, because the efficacy of cancer immunotherapy in humans has been shown to depend on sex, with better outcomes in males ⁸⁷.

Previous bulk RNA-seq and proteomic studies demonstrated that in naïve mice, male microglia show the enrichment of inflammation and antigen presentation-related genes,

whereas female microglia have higher neuroprotective capacity^{95,97}. Until now, sex differences have been largely unexplored in animal studies of glioma immunobiology.

In this work, we demonstrate for the first time the sex-dependent differences in responses of GAMs to the tumor. This notion is supported by several findings. First, the antigen presentation components were expressed at higher levels in myeloid cells (especially Act-MG, Int, MΦ) derived from male glioma-bearing brains. The observation, first made in the scRNA-seq analysis, has been verified by CITE-seq and qPCR in primary microglia exposed to glioma in *in vitro* co-cultures. The differences were found both at the RNA level of MHCII encoding genes (*Cd74*, *H2-Aa*, *H2-Ab1*, *H2-Eb1*) and at the protein level (MHCII complex).

Secondly, the interferon-response genes showed the enrichment in MΦ populations from female brains with glioma. Interestingly, the sex differences in both MHCII level and the interferon response were most pronounced at the pre-symptomatic glioma stage (14 days post-implantation) and diminished at the symptomatic stage (21 days post-implantation).

Third, the contribution of the differentiated macrophages to the GAM population was higher in males. In females, MΦ constituted 13% and 31% of GAMs at 14 and 21 day post-implantation, respectively. Whereas in males MΦ constituted 27% of GAMs already at day 14, and their proportion increased to 45% at day 21. Additionally, females showed a two times higher proportion of monocytes compared to males.

Public data sets were employed to validate this finding. In the re-analysis of CyTOF data from human GBMs, the proportion of monocytes was found to achieve high values in females, which was not observed in males⁷². Whereas males showed a bigger fraction of macrophages compared with females in the scRNA-seq data from human primary GBMs⁷⁷. A limited number of human studies with a relatively low number of subjects of both sexes makes it difficult to compare male and female gliomas. As the number of patients in the re-analyzed data sets was quite low, this observation requires further verification.

Nevertheless, all observed sex differences consistently indicate a more persistent pro-inflammatory response in females as compared with the male counterparts. This difference is reflected by the variety of the transcriptional programs that change with the tumor progression and a lower accumulation of the immuno-suppressive macrophages, despite a higher number of infiltrating monocytes.

7.9. CLINICAL IMPLICATIONS OF THE MYELOID CELL DIVERSITY

Understanding of the myeloid cell diversity within glioma TME and dissecting population-specific functions might greatly enhance a quest for immune-therapeutics aiming at reactivation of the host antitumor response.

The immune checkpoint blockade (ICB) therapies have been successful at reactivation of the T cell-mediated immunity and improved patients outcomes in various cancers, including melanoma and non-small cell lung cancer. However, ICB failed to increase survival of GBM patients¹⁸⁰, likely due to a reduced ability of cytotoxic T lymphocytes to enter and act in the immunosuppressive, tumor-bearing brain parenchyma.

In malignant gliomas, microglia and monocytes/macrophages are the predominant immune cell populations. However, only the frequency of monocytes/macrophages negatively correlates with a patient's survival, whereas the abundance of microglia does not show such correlation³⁹. We demonstrated in this study that monocytes/macrophages localize predominantly in the tumor core and outnumber microglia at the symptomatic stage of glioma growth. In addition, differentiated macrophages that accumulate in the tumor niche were found to be the major source of the immunosuppressive and tumor-supportive factors. Thus, drugs blocking monocyte infiltration or depleting differentiated macrophages may have clinical potential.

Pharmacological GAMs depletion has been already tested in animal studies, resulting in attenuated tumor growth^{34,181}. Colony stimulating factor 1 receptor (CSF1R) is essential for survival of microglia and MDMs. Treatment with a CSF1R inhibitor (PLX3397, Pexidartinib) showed a good efficacy in preclinical studies¹⁸². In GBM patients, Pexidartinib efficiently reduced the number of circulating monocytes and showed good CNS penetration, however it failed to show anti-glioma efficacy¹⁸³. This lack of effectiveness could be ascribed to a high expression of CSF2/GM-CSF by glioma cells, which stimulates macrophage proliferation and thus may compensate for the CSF1R inhibition¹⁸⁴.

In this study, CD49d was shown to be uniformly expressed by all monocyte/macrophages and CD11b⁺ DCs. CD49d and CD29 form an integrin dimer VLA-4 (very late antigen 4) that is an adhesion molecule involved in lymphocyte homing to the inflamed brain¹⁷². In a study employing transgenic mouse gliomas, the CD49d blockade was found to interfere with the MDM infiltration to glioma, without affecting the number of circulating monocytes, and to reduce the number of differentiated macrophages in glioma TME by a half¹⁷³. The anti-CD49d antibody, Natalizumab, is an approved drug for the treatment of relapsing-remitting multiple

sclerosis. Thus, knowing the drug safety, pharmacokinetics and side effects, the repurposing for glioma treatment might be feasible in a shorter time.

Still, in order to induce a successful reactivation of immune system cells in GBM patients, combination of therapies that will target multiple routes of immunosuppression, might be required. Inter-patient variability might also be an important factor, thus the development of the immune infiltrate diagnostic markers could help to “tailor” an immuno-modulating therapy to the patient immune environment.

8. Summary and conclusions

In this study, we implemented single-cell omics approaches: scRNA-seq and CITE-seq, and demonstrated that myeloid cells exhibit profound heterogeneity in glioma TME. The observed diversity can be ascribed to: (1) contribution of distinct cell types (microglia, MDMs, DCs), (2) occurrence of cells of the same type but at different differentiation stages, (3) expression of specialized transcriptomic programs that can be either shared across different cell types or enriched in a given population.

The following conclusions can be drawn based on the results of this dissertation:

- I. Microglia and infiltrating myeloid cells (MDMs and DCs) can be reliably distinguished using protein markers: Tmem119 (microglia) and CD49d, CD45, intracellular Gal-3 (MDMs and DCs).
- II. In glioma TME, microglia and MDMs exhibit diverse transcriptional programs that are:
 - i. common: “Antigen presentation”, “Lipid metabolism and phagocytosis”
 - ii. microglia-enriched: “Cytokine-related”, “Proliferation-related”
 - iii. MDMs-enriched: “IFN-related”, “Immunosuppression and tumor support”
- III. Microglia and MDMs show distinct localization with a respect to the tumor (microglia – adjacent brain parenchyma, MDMs – tumor core) and substantial differences regarding the tumor-induced activation: stronger expression of the identified transcriptional programs in MDMs.
- IV. MDMs exhibit transcriptional and surface protein changes indicative of a monocyte-to-macrophage transition in glioma TME. The transition is connected with the downregulation of the interferon-response genes and upregulation of the immunosuppressive PD-L1 protein and genes implicated in supporting tumor growth.
- V. Monocytes are found both at the pre-symptomatic and symptomatic stages at the same frequency, whereas differentiated macrophages show increasing proportion and constitute the most abundant myeloid population at the symptomatic stage.
- VI. Sex impacts the glioma-induced responses of myeloid cells. In males, GAMs show an elevated level of MHCII, while females have the increased expression of the interferon-response genes. The differences might be due to a higher proportion of monocytes found in females and delayed monocyte-to-macrophage transition.

In summary, malignant gliomas are inevitably lethal tumors with very limited therapeutic options. The failure of novel therapeutics observed in clinical trials is largely due to a substantial inter and intra-tumor heterogeneity. The immune cells contribute to this complexity shaping the glioma microenvironment, influencing tumor progression and its response to therapy. Dissection of functions of individual components of the immune microenvironment in malignant gliomas may help to resolve this complexity and pave ways to design therapies tailored to specific immune phenotypes.

List of symbols and abbreviations

I. Abbreviations

2-HG	2-hydroxyglutarate
α -KG	alpha ketoglutarate
Ab-oligo	antibody-oligonucleotide conjugate
AC	astrocyte
Act-MG	tumor-activated microglia
Act-MG	tumor-activated microglia
ANOVA	analysis of variance
APC	antigen presentation cells
BM	bone marrow
CD	cluster of differentiation
cDC1	classical dendritic cells 1
cDC2	classical dendritic cells 2
cDCs	conventional dendritic cells
cDNA	complementary DNA
CITEseq	Cellular Indexing of Transcriptomes and Epitopes by sequencing
CNS	central nervous system
CytoF	Cytometry by Time-Of-Flight
DAPI	4',6-diamidino-2-phenylindole
DCs	dendritic cells
DMEM	Dulbecco's Modified Eagle Medium
EMP	erythromyeloid progenitors
FACS	Fluorescence Activated Cell Sorting
FBS	fetal bovine serum
GAM	glioma associated microglia and macrophages
GBM	glioblastoma multiforme
G-CIMP	glioma CpG island methylator phenotype
GEM	gel-bead in emulsion
Hom-MG	homeostatic microglia
Hom-MG	homeostatic microglia
HSC	hematopoietic stem cells
HTO	hashtag-oligo barcode
ICB	immune checkpoint blockade
ICB	immune checkpoint blockade
IDH	isocitrate dehydrogenase
IFN	interferon
IFN	interferon
Int	monocyte/macrophage intermediate
Luc	luciferase
MDM	monocyte-derived macrophages

MDMs	monocyte-derived macrophages
MDSC	myeloid derived suppressor cells
MES	mesenchymal
MG	microglia
MG	microglia
Mo	monocytes
Mo/MΦ	monocytes/macrophages
Mo-DCs	monocyte-derived dendritic cells
mRNA	messenger RNA
MΦ	macrophages
NK cells	natural killer cells
NPC	neural progenitor cell
OPC	oligodendrocyte progenitor cell
PBS	Phosphate buffered saline
PCA	principal component analysis
PCR	polymerase chain reaction
PFA	paraformaldehyde
REAP-seq	RNA expression and protein sequencing assay
RNA	ribonucleic acid
scRNA-seq	single cell RNA sequencing
SDS-PAGE	sodium dodecyl sulphate–polyacrylamide gel electrophoresis
TCGA	The Cancer Genome Atlas
tdT	tandem dimer Tomato
TME	tumor microenvironment
TME	tumor microenvironment
Tregs	T regulatory lymphocytes
tSNE	t-Distributed Stochastic Neighbor Embedding
UMAP	Uniform Manifold Approximation and Projection
UMI	unique molecular identifier
WHO	world health organization

II. Gene symbols

Throughout the manuscript, gene symbols for mouse are given with first letter in upper-case (e.g. *Tmem119*) and for human with all letters in upper-case (e.g. *TMEM119*). If not specified otherwise, the gene symbols in the abbreviation list are given with use of the formatting for mouse genes,

<i>Actb</i>	Actin beta
<i>Adam8</i>	A disintegrin and metalloproteinase domain 8
<i>Apoe</i>	Apolipoprotein E
<i>Ascl1</i>	Achaete-Scute Family BHLH transcription factor 1
<i>Atf3</i>	Activating transcription factor 3
<i>Atrx</i>	Alpha-thalassemia/mental Retardation, X-linked

<i>B2m</i>	Beta-2 microglobulin
<i>Birc5</i>	Baculoviral IAP repeat-containing 5
<i>Bnip3</i>	BCL2 Interacting Protein 3
<i>Bst2</i>	Bone marrow stromal cell antigen 2
<i>Btla</i>	B and T lymphocyte associated
<i>C1qa</i>	Complement component 1, q subcomponent, alpha polypeptide
<i>C1qb</i>	Complement component 1, q subcomponent, beta polypeptide
<i>C1qc</i>	Complement component 1, q subcomponent, C chain
<i>C4b</i>	Complement component 4B1
<i>Ccl12</i>	Chemokine (C-C motif) ligand 12
<i>Ccl2</i>	C-C Motif Chemokine Ligand 2
<i>Ccl3</i>	C-C Motif Chemokine Ligand 3
<i>Ccl4</i>	C-C Motif Chemokine Ligand 9
<i>Ccl9</i>	C-C Motif Chemokine Ligand 5
<i>Ccna2</i>	Cyclin A2
<i>Ccnb1</i>	Cyclin B1
<i>Ccnb2</i>	Cyclin B2
<i>Ccr2</i>	Chemokine (C-C motif) receptor 2
<i>Ccr7</i>	Chemokine (C-C motif) receptor 7
<i>Cd3d</i>	Cluster of Differentiation 3d
<i>Cd9</i>	Cluster of Differentiation 9
<i>Cd24a</i>	Cluster of Differentiation 24a
<i>Cd274</i>	Cluster of Differentiation 274
<i>Cd44</i>	Cluster of Differentiation 44
<i>Cd52</i>	Cluster of Differentiation 52
<i>Cd74</i>	Cluster of Differentiation 44
<i>Cd80</i>	Cluster of Differentiation 80
<i>Cd81</i>	Cluster of Differentiation 74
<i>Cd83</i>	Cluster of Differentiation 80
<i>Cd86</i>	Cluster of Differentiation 86
<i>Cdk1</i>	Cyclin-dependent kinase 1
<i>Cdk4</i>	Cyclin-dependent kinase 4
<i>Cdkn2a</i>	Cyclin dependent kinase inhibitor 2A
<i>Chi3l1</i>	Cyclin Dependent Kinase 4
<i>Cited2</i>	<i>Cyclin Dependent Kinase Inhibitor 2a</i>
<i>Cks1b</i>	Chitinase 3 Like 1
<i>Crip1</i>	Cysteine-rich protein 1
<i>Csf1r</i>	Colony stimulating factor 1 receptor
<i>Csf1</i>	Colony stimulating factor 1
<i>Cst3</i>	Cystatin C
<i>Ctsb</i>	Cathepsin B
<i>Ctsd</i>	Cathepsin D
<i>Ctss</i>	Cathepsin S
<i>Cx3cr2</i>	Chemokine (C-X3-C motif) receptor 1
<i>Cxcl10</i>	Chemokine (C-X-C motif) ligand 10
<i>Dab2</i>	Cisabled 2, mitogen-responsive phosphoprotein
<i>Dcx</i>	Doublecortin
<i>Dll3</i>	Delta like canonical Notch ligand 3

<i>Dpp4</i>	Dipeptidylpeptidase 4
<i>Egfr</i>	Epidermal growth factor receptor
<i>Egr1</i>	Early growth response 1
<i>Emilin2</i>	Elastin microfibril interfacier 2
<i>F13a1</i>	Coagulation factor XIII, A1 subunit
<i>Fabp5</i>	Fatty Acid Binding Protein 5
<i>Fcgr1</i>	Fc receptor, IgG, high affinity I
<i>Fcrls</i>	Fc receptor-like S
<i>Fos</i>	FBJ osteosarcoma oncogene
<i>Fosb</i>	FBJ osteosarcoma oncogene B
<i>Gapdh</i>	Glyceraldehyde-3-Phosphate Dehydrogenase
<i>Gpnmb</i>	Glycoprotein Nmb
<i>Gpr34</i>	G Protein-Coupled Receptor 34
<i>Gpr84</i>	G Protein-Coupled Receptor 84
<i>H2-Aa</i>	Histocompatibility 2, class II antigen A, alpha
<i>H2-Ab1</i>	Histocompatibility 2, class II antigen A, beta 1
<i>H2-Eb1</i>	Histocompatibility 2, class II antigen E, beta 1
<i>H2-K1</i>	Histocompatibility 2, K1, K region
<i>H2-Oa</i>	Histocompatibility 2, O region alpha locus
<i>Hexb</i>	Hexosaminidase B
<i>Hif1a</i>	Hypoxia Inducible Factor 1 Subunit Alpha
<i>Hilpda</i>	Hypoxia Inducible Lipid Droplet Associated
<i>Hmgb2</i>	High mobility group box 2
<i>Hp</i>	Haptoglobin
<i>Idh1</i>	Isocitrate dehydrogenase 1
<i>Idh2</i>	Isocitrate dehydrogenase 2
<i>Ier2</i>	Immediate early response 2
<i>Ifi205</i>	Interferon activated gene 205
<i>Ifi27</i>	Interferon alpha inducible protein 27
<i>Ifit2</i>	Interferon induced protein with tetratricopeptide repeats 2
<i>Ifit3</i>	Interferon induced protein with tetratricopeptide repeats 3
<i>Ifitm1</i>	Interferon induced transmembrane protein 1
<i>Ifitm2</i>	Interferon induced transmembrane protein 2
<i>Ifitm3</i>	Interferon induced transmembrane protein 3
<i>Ifitm6</i>	Interferon induced transmembrane protein 6
<i>Il18b</i>	Interleukin 1 beta
<i>Il1a</i>	Interleukin 1 alpha
<i>Il1b</i>	Interleukin 1 beta
<i>Il1rn</i>	Interleukin 1 receptor antagonist
<i>Il4I1</i>	Interleukin 4 induced 1
<i>Irf7</i>	Interferon regulatory factor 7
<i>Isg15</i>	Interferon-stimulated protein, 15 KDa
<i>Itga4</i>	Integrin alpha 4
<i>Itgax</i>	Integrin alpha X
<i>Jun</i>	Jun proto-oncogene
<i>Junb</i>	Jun B proto-oncogene
<i>Klf2</i>	Kruppel-like factor 2
<i>Klf4</i>	Kruppel-like factor 4

<i>Klrb1C</i>	Killer cell lectin-like receptor subfamily B member 1C
<i>K-ras</i>	Kirsten rat sarcoma virus
<i>Lgals3</i>	Lectin, galactose binding, soluble 3
<i>Lglas3bp</i>	Lectin, galactose binding, soluble 3 binding protein
<i>Lpl</i>	Lipoprotein Lipase
<i>Ly6c3</i>	Lymphocyte antigen 6 complex, locus C2
<i>Ly6i</i>	Lymphocyte antigen 6 complex, locus I
<i>Ly75</i>	Lymphocyte antigen 75
<i>Mcm5</i>	Minichromosome maintenance complex component 5
<i>Mertk</i>	MER proto-oncogene, tyrosine kinase
<i>Mgl2</i>	Macrophage galactose N-acetyl-galactosamine specific lectin 2
<i>Mif</i>	Macrophage migration inhibitory factor
<i>Mrc1</i>	Mannose receptor, C type 1
<i>Ms4A7</i>	Membrane-spanning 4-domains, subfamily A, member 7
<i>Myc</i>	Myc proto-oncogene
<i>Ncam1</i>	Neural cell adhesion molecule 1
<i>Ncr1</i>	Natural cytotoxicity triggering receptor 1
<i>Nf1</i>	Neurofibromatosis 1
<i>Nkx-2</i>	NK2 Homeobox 2
<i>Olfml3</i>	Olfactomedin-like 3
<i>Olig2</i>	Oligodendrocyte Transcription Factor 2
<i>P2ry12</i>	Purinergic Receptor P2Y, G-Protein Coupled, 12
<i>P2ry13</i>	Purinergic Receptor P2Y, G-Protein Coupled, 13
<i>Pclaf</i>	PCNA clamp associated factor
<i>Pdcd1lg2</i>	Programmed cell death 1 ligand 2
<i>Pdgfra</i>	<i>Platelet derived growth factor receptor alpha</i>
<i>Pf4</i>	Platelet factor 4
<i>Pten</i>	Phosphatase And Tensin Homolog
<i>Ptprc</i>	Protein Tyrosine Phosphatase Receptor Type C
<i>Rsad2</i>	Radical S-Adenosyl Methionine Domain Containing 2
<i>S100a11</i>	S100 calcium binding protein A11
<i>S100a6</i>	S100 calcium binding protein A6
<i>Sell</i>	Selectin, lymphocyte
<i>Selplg</i>	Selectin, platelet (p-selectin) ligand
<i>Sox</i>	SRY-box transcription factor
<i>Sparc</i>	Secreted Protein Acidic And Cysteine Rich
<i>Spp1</i>	Secreted phosphoprotein 1
<i>Stat1</i>	Signal transducer and activator of transcription 1
<i>Stat4</i>	Signal transducer and activator of transcription 4
<i>Stmn1</i>	Stathmin 1
<i>Tcf4</i>	Transcription factor 4
<i>Tert</i>	Telomerase reverse transcriptase
<i>Tgfb1</i>	Transforming growth factor, beta induced
<i>Tgm2</i>	Transglutaminase 2
<i>Tmem119</i>	Transmembrane Protein 119
<i>Tnf</i>	Tumor necrosis factor
<i>Top2A</i>	Topoisomerase (DNA) II alpha
<i>TP54</i>	Tumor Protein 53 (human)

<i>p54</i>	Tumor protein 53 (mouse)
<i>Trem2</i>	Triggering receptor expressed on myeloid Cells 2
<i>Tuba1b</i>	Tubulin, alpha 1B
<i>Tubb4b</i>	Tubulin, beta 4B class IVB
<i>Tubb5</i>	Tubulin, beta 5 class I
<i>Ube2c</i>	Ubiquitin-conjugating enzyme E2C
<i>Usp15</i>	Ubiquitin specific peptidase 15
<i>Vcan</i>	Versican
<i>Vegfa</i>	Vascular endothelial growth factor A

III. Protein symbols

Throughout the manuscript, protein symbols for mouse are given with first letter in upper-case (e.g. *Tmem119*) and for human with all letters in upper-case (e.g. *TMEM119*). If not specified otherwise, the protein symbols in the abbreviation list are given with use of the formatting for mouse protein symbols.

<i>Cadm1</i>	Cell adhesion molecule 1
<i>Ccl2</i>	C-C motif chemokine ligand 2
<i>Ccl19</i>	C-C motif chemokine ligand 19
<i>Ccl21</i>	C-C motif chemokine ligand 21
<i>Ccl22</i>	C-C motif chemokine ligand 22
<i>Ccr2</i>	C-C motif chemokine receptor 2
<i>Ccr7</i>	C-C motif chemokine receptor 7
<i>CD11b</i>	Cluster of Differentiation 11 b
<i>CD39</i>	Cluster of Differentiation 39
<i>CD45</i>	Cluster of Differentiation 45
<i>CD49d</i>	Cluster of Differentiation 209
<i>CD210</i>	Cluster of Differentiation 49 d
<i>Csf1</i>	Colony stimulating factor 1
<i>Csf1R</i>	Colony stimulating factor 1 receptor
<i>Ctla4</i>	Cytotoxic T-Lymphocyte associated protein 4
<i>Cx3Cr1</i>	CX3C chemokine receptor 1
<i>Cystatin C</i>	Cystatin C
<i>Gal-3</i>	Galectin 3
<i>Gpmnb</i>	Transmembrane glycoprotein NMB
<i>Hla</i>	Human Leukocyte Antigen (human)
<i>Iba1</i>	Ionized calcium binding adaptor molecule 1
<i>Ifi</i>	Interferon gamma inducible
<i>Ifitm</i>	Interferon induced transmembrane protein
<i>Il-1B</i>	Interleukin 1 beta
<i>Il-2</i>	Interleukin 2
<i>Il-4</i>	Interleukin 4
<i>Il-10</i>	Interleukin 10

Il-27	Interleukin 27
Il-35	Interleukin 35
Inos	inducible Nitric Oxide Synthase
Irf7	Interferon regulatory factor 7
Isg15	Interferon stimulated gene 15
Lag-3	Lymphocyte-activation gene 3
MHC	Major histocompatibility complex
p54	Tumor protein p53
PD-2	Programmed Cell Death 1
PD-L1	Programmed Cell Death Ligand 1
PD-L2	Programmed Cell Death Ligand 2
Pge2	Prostaglandin E2
Ras	Rat sarcoma virus
Spp1	Osteopontin
Stat1	Signal transducer and activator of transcription 1
TGF- β	Transforming growth factor beta
Tigit	T cell immunoreceptor with Ig and ITIM domains
Tim-3	T-Cell Immunoglobulin And Mucin Domain-Containing Protein 3
Tmem119	Transmembrane Protein 119
TNF- α	Tumour necrosis factor alpha
Trem2	Triggering receptor expressed on myeloid cells 2
Usp18	Ubl carboxyl-terminal hydrolase 18

References

1. Ostrom, Q. T. *et al.* CBTRUS statistical report: Primary brain and other central nervous system tumors diagnosed in the United States in 2013-2017. *Neuro. Oncol.* **22**, (2020).
2. Louis, D. N. *et al.* The 2007 WHO classification of tumours of the central nervous system. *Acta Neuropathologica* vol. 114 97–109 (2007).
3. Louis, D. N. *et al.* The 2016 World Health Organization Classification of Tumors of the Central Nervous System: a summary. *Acta Neuropathologica* vol. 131 803–820 (2016).
4. Koshy, M. *et al.* Improved survival time trends for glioblastoma using the SEER 17 population-based registries. *J. Neurooncol.* **107**, (2012).
5. Lin, Z. *et al.* Establishment of age group classification for risk stratification in glioma patients. *BMC Neurol.* **20**, (2020).
6. Lukas, R. V. *et al.* Newly diagnosed glioblastoma: A review on clinical management. *ONCOLOGY (United States)* vol. 33 91–100 (2019).
7. Ceccarelli, M. *et al.* Molecular Profiling Reveals Biologically Discrete Subsets and Pathways of Progression in Diffuse Glioma. *Cell* **164**, 550–563 (2016).
8. Yan, H. *et al.* IDH1 and IDH2 Mutations in Gliomas. *N. Engl. J. Med.* **360**, 765–773 (2009).
9. Turcan, S. *et al.* IDH1 mutation is sufficient to establish the glioma hypermethylator phenotype. *Nature* **483**, (2012).
10. Kaminska, B., Czapki, B., Guzik, R., Król, S. K. & Gielniewski, B. Consequences of IDH1/2 mutations in gliomas and an assessment of inhibitors targeting mutated IDH proteins. *Molecules* vol. 24 (2019).
11. Houillier, C. *et al.* IDH1 or IDH2 mutations predict longer survival and response to temozolomide in low-grade gliomas. *Neurology* **75**, 1560–1566 (2010).
12. Lewandowska, M. A. *et al.* An analysis of the prognostic value of IDH1 (isocitrate dehydrogenase 1) mutation in Polish glioma patients. *Mol. Diagnosis Ther.* **18**, 45–53 (2014).
13. Parsons, D. W. *et al.* An integrated genomic analysis of human glioblastoma multiforme. *Science (80-.)*. **321**, (2008).
14. Balss, J. *et al.* Analysis of the IDH1 codon 132 mutation in brain tumors. *Acta Neuropathol.* **116**, (2008).
15. Verhaak, R. G. W. *et al.* Integrated Genomic Analysis Identifies Clinically Relevant Subtypes of Glioblastoma Characterized by Abnormalities in PDGFRA, IDH1, EGFR, and NF1. *Cancer Cell* **17**, 98–110 (2010).
16. Wang, Q. *et al.* Tumor Evolution of Glioma-Intrinsic Gene Expression Subtypes Associates with Immunological Changes in the Microenvironment. *Cancer Cell* **32**, 42–56.e6 (2017).
17. Their, J. P. Epithelial-mesenchymal transitions in tumor progression. *Nature Reviews Cancer* vol. 2 (2002).
18. Patel, A. P. *et al.* Single-cell RNA-seq highlights intratumoral heterogeneity in primary glioblastoma. *Science (80-.)*. **344**, 1396–1401 (2014).
19. Sottoriva, A. *et al.* Intratumor heterogeneity in human glioblastoma reflects cancer evolutionary dynamics. *Proc. Natl. Acad. Sci. U. S. A.* **110**, (2013).
20. Nduom, E. K., Weller, M. & Heimberger, A. B. Immunosuppressive mechanisms in glioblastoma. *Neuro. Oncol.* **17**, vii9–vii14 (2015).
21. Nakano, Y., Kuroda, E., Kito, T., Yokota, A. & Yamashita, U. Induction of macrophagic prostaglandin E2 synthesis by glioma cells. *J. Neurosurg.* **104**, 574–582

- (2006).
22. Golán, I., De La Fuente, L. R. & Costoya, J. A. NK cell-based glioblastoma immunotherapy. *Cancers (Basel)*. **10**, (2018).
 23. Kozłowska, A. K. *et al.* Resistance to cytotoxicity and sustained release of interleukin-6 and interleukin-8 in the presence of decreased interferon- γ after differentiation of glioblastoma by human natural killer cells. *Cancer Immunol. Immunother.* **65**, 1085–1097 (2016).
 24. Wang, H. *et al.* Different T-cell subsets in glioblastoma multiforme and targeted immunotherapy. *Cancer Letters* vol. 496 134–143 (2021).
 25. Chongsathidkiet, P. *et al.* Sequestration of T cells in bone marrow in the setting of glioblastoma and other intracranial tumors. *Nat. Med.* **24**, 1459–1468 (2018).
 26. Woroniecka, K. *et al.* T-cell exhaustion signatures vary with tumor type and are severe in glioblastoma. *Clin. Cancer Res.* **24**, 4175–4186 (2018).
 27. Tawbi, H. A. *et al.* Combined Nivolumab and Ipilimumab in Melanoma Metastatic to the Brain. *N. Engl. J. Med.* **379**, 722–730 (2018).
 28. Hendriks, L. E. L. *et al.* Outcome of Patients with Non–Small Cell Lung Cancer and Brain Metastases Treated with Checkpoint Inhibitors. *J. Thorac. Oncol.* **14**, 1244–1254 (2019).
 29. Simmons, G. W. *et al.* Neurofibromatosis-1 heterozygosity increases microglia in a spatially and temporally restricted pattern relevant to mouse optic glioma formation and growth. *J. Neuropathol. Exp. Neurol.* **70**, 51–62 (2011).
 30. Tirosch, I. *et al.* Single-cell RNA-seq supports a developmental hierarchy in human oligodendroglioma. *Nature* **539**, 309–313 (2016).
 31. Gieryng, A., Pszczolkowska, D., Walentynowicz, K. A., Rajan, W. D. & Kaminska, B. *Immune microenvironment of gliomas*. vol. 97 498–518 (United States & Canadian Academy of Pathology USCAP, Inc, 2017).
 32. Ellert-Miklaszewska, A. *et al.* Molecular definition of the pro-tumorigenic phenotype of glioma-activated microglia. *Glia* **61**, 1178–1190 (2013).
 33. Mieczkowski, J. *et al.* Down-regulation of IKK β expression in glioma-infiltrating microglia/macrophages is associated with defective inflammatory/immune gene responses in glioblastoma. *Oncotarget* (2015) doi:10.18632/oncotarget.5310.
 34. Sliwa, M. *et al.* The invasion promoting effect of microglia on glioblastoma cells is inhibited by cyclosporin A. *Brain* **130**, 476–489 (2007).
 35. Wesolowska, A. *et al.* Microglia-derived TGF- β as an important regulator of glioblastoma invasion - An inhibition of TGF- β -dependent effects by shRNA against human TGF- β type II receptor. *Oncogene* (2008) doi:10.1038/sj.onc.1210683.
 36. Szulzewsky, F. *et al.* Glioma-associated microglia/macrophages display an expression profile different from M1 and M2 polarization and highly express Gpnmb and Spp1. *PLoS One* **10**, e0116644 (2015).
 37. Gabrusiewicz, K. *et al.* Glioblastoma-infiltrated innate immune cells resemble M0 macrophage phenotype. *JCI insight* **1**, 1–32 (2016).
 38. Venteicher, A. S. *et al.* Decoupling genetics, lineages, and microenvironment in IDH-mutant gliomas by single-cell RNA-seq. *Science (80-.)*. **355**, eaai8478 (2017).
 39. Müller, S. *et al.* Single-cell profiling of human gliomas reveals macrophage ontogeny as a basis for regional differences in macrophage activation in the tumor microenvironment. *Genome Biol.* **18**, 234 (2017).
 40. Gomez Perdiguero, E. *et al.* Tissue-resident macrophages originate from yolk-sac-derived erythro-myeloid progenitors. *Nature* (2015) doi:10.1038/nature13989.
 41. Ginhoux, F. *et al.* Fate mapping analysis reveals that adult microglia derive from primitive macrophages. *Science (80-.)*. **330**, 841–845 (2010).

42. Schulz, C. *et al.* A lineage of myeloid cells independent of myb and hematopoietic stem cells. *Science* (80-.). **335**, 86–90 (2012).
43. Boisset, J. C. *et al.* In vivo imaging of haematopoietic cells emerging from the mouse aortic endothelium. *Nature* (2010) doi:10.1038/nature08764.
44. Orkin, S. H. & Zon, L. I. Hematopoiesis: An Evolving Paradigm for Stem Cell Biology. *Cell* (2008) doi:10.1016/j.cell.2008.01.025.
45. Orkin, S. H. Diversification of haematopoietic stem cells to specific lineages. *Nature Reviews Genetics* (2000) doi:10.1038/35049577.
46. Lavin, Y. *et al.* Tissue-resident macrophage enhancer landscapes are shaped by the local microenvironment. *Cell* **159**, 1312–1326 (2014).
47. Gosselin, D. *et al.* An environment-dependent transcriptional network specifies human microglia identity. *Science* (80-.). **356**, 1248–1259 (2017).
48. Gieryng, A. *et al.* Immune microenvironment of experimental rat C6 gliomas resembles human glioblastomas. *Sci. Rep.* **7**, 17556 (2017).
49. Szulzewsky, F. *et al.* Human glioblastoma-associated microglia/monocytes express a distinct RNA profile compared to human control and murine samples. *Glia* **64**, 1416–1436 (2016).
50. Walentynowicz, K. A. *et al.* In search for reliable markers of glioma-induced polarization of microglia. *Front. Immunol.* **9**, 1–13 (2018).
51. Li, W. & Graeber, M. B. The molecular profile of microglia under the influence of glioma. *Neuro-Oncology* (2012) doi:10.1093/neuonc/nos116.
52. Sedgwick, J. D. *et al.* Isolation and direct characterization of resident microglial cells from the normal and inflamed central nervous system. *Proc. Natl. Acad. Sci.* (1991) doi:10.1073/pnas.88.16.7438.
53. Ford, A. L., Goodsall, A. L., Hickey, W. F. & Sedgwick, J. D. Normal adult ramified microglia separated from other central nervous system macrophages by flow cytometric sorting. Phenotypic differences defined and direct ex vivo antigen presentation to myelin basic protein-reactive CD4+ T cells compared. *J. Immunol.* **154**, 4309 LP – 4321 (1995).
54. Hussain, S. F. The role of human glioma-infiltrating microglia/macrophages in mediating antitumor immune responses. *Neuro. Oncol.* (2006) doi:10.1215/15228517-2006-008.
55. Müller, A., Brandenburg, S., Turkowski, K., Müller, S. & Vajkoczy, P. Resident microglia, and not peripheral macrophages, are the main source of brain tumor mononuclear cells. *Int. J. Cancer* **137**, 278–288 (2015).
56. Chen, Z. *et al.* Cellular and molecular identity of tumor-associated macrophages in glioblastoma. *Cancer Res.* **77**, 2266–2278 (2017).
57. Gabrusiewicz, K. *et al.* Characteristics of the alternative phenotype of microglia/macrophages and its modulation in experimental gliomas. *PLoS One* **6**, e23902 (2011).
58. Parkhurst, C. N. *et al.* Microglia promote learning-dependent synapse formation through brain-derived neurotrophic factor. *Cell* (2013) doi:10.1016/j.cell.2013.11.030.
59. Bowman, R. L. *et al.* Macrophage Ontogeny Underlies Differences in Tumor-Specific Education in Brain Malignancies. *Cell Rep.* **17**, 2445–2459 (2016).
60. Klemm, F. *et al.* Interrogation of the Microenvironmental Landscape in Brain Tumors Reveals Disease-Specific Alterations of Immune Cells. *Cell* **181**, 1643-1660.e17 (2020).
61. Bennett, M. L. *et al.* New tools for studying microglia in the mouse and human CNS. *Proc. Natl. Acad. Sci. U. S. A.* **113**, E1738–E1746 (2016).
62. Zrzavy, T. *et al.* Loss of ‘homeostatic’ microglia and patterns of their activation in

- active multiple sclerosis. *Brain* (2017) doi:10.1093/brain/awx113.
63. Spiteri, A. G. *et al.* High-parameter cytometry unmasks microglial cell spatio-temporal response kinetics in severe neuroinflammatory disease. *J. Neuroinflammation* **18**, (2021).
 64. Papalexis, E. & Satija, R. Single-cell RNA sequencing to explore immune cell heterogeneity. *Nature Reviews Immunology* vol. 18 35–45 (2018).
 65. Yao, Y. *et al.* CyTOF supports efficient detection of immune cell subsets from small samples. *J. Immunol. Methods* **415**, 1–5 (2014).
 66. Stoeckius, M. *et al.* Simultaneous epitope and transcriptome measurement in single cells. *Nat. Methods* (2017) doi:10.1038/nmeth.4380.
 67. Ståhl, P. L. *et al.* Visualization and analysis of gene expression in tissue sections by spatial transcriptomics. *Science* vol. 353 78–82 (2016).
 68. Vickovic, S. *et al.* High-definition spatial transcriptomics for in situ tissue profiling. *Nat. Methods* **16**, (2019).
 69. Ochocka, N. & Kaminska, B. Microglia diversity in healthy and diseased brain: Insights from single-cell omics. *International Journal of Molecular Sciences* vol. 22 1–26 (2021).
 70. Kaminska, B., Ochocka, N. & Segit, P. Single-Cell Omics in Dissecting Immune Microenvironment of Malignant Gliomas—Challenges and Perspectives. *Cells* vol. 10 (2021).
 71. Berghoff, A. S. *et al.* Correlation of immune phenotype with IDH mutation in diffuse glioma. *Neuro. Oncol.* **19**, 1460–1468 (2017).
 72. Friebel, E. *et al.* Single-Cell Mapping of Human Brain Cancer Reveals Tumor-Specific Instruction of Tissue-Invading Leukocytes. *Cell* **181**, 1626-1642.e20 (2020).
 73. Darmanis, S. *et al.* Single-Cell RNA-Seq Analysis of Infiltrating Neoplastic Cells at the Migrating Front of Human Glioblastoma. *Cell Rep.* **21**, 1399–1410 (2017).
 74. Foltz, G. D., Pulchalski, R. B. & Shah, N. Ivy Glioblastoma Atlas Project.
 75. Darmanis, S. *et al.* Single-Cell RNA-Seq Analysis of Infiltrating Neoplastic Cells at the Migrating Front of Human Glioblastoma. *Cell Rep.* **21**, 1399–1410 (2017).
 76. Sankowski, R. *et al.* Mapping microglia states in the human brain through the integration of high-dimensional techniques. *Nat. Neurosci.* **22**, 2098–2110 (2019).
 77. Pombo Antunes, A. R. *et al.* Single-cell profiling of myeloid cells in glioblastoma across species and disease stage reveals macrophage competition and specialization. *Nat. Neurosci.* **24**, (2021).
 78. Parker, B. S., Rautela, J. & Hertzog, P. J. Antitumour actions of interferons: Implications for cancer therapy. *Nature Reviews Cancer* vol. 16 (2016).
 79. Deczkowska, A., Weiner, A. & Amit, I. The Physiology, Pathology, and Potential Therapeutic Applications of the TREM2 Signaling Pathway. *Cell* vol. 181 (2020).
 80. Ulland, T. K. *et al.* TREM2 Maintains Microglial Metabolic Fitness in Alzheimer’s Disease. *Cell* **170**, (2017).
 81. Gratuze, M., Leyns, C. E. G. & Holtzman, D. M. New insights into the role of TREM2 in Alzheimer’s disease. *Molecular Neurodegeneration* vol. 13 (2018).
 82. Brosseau, C., Colas, L., Magnan, A. & Brouard, S. CD9 tetraspanin: A new pathway for the regulation of inflammation? *Frontiers in Immunology* vol. 9 (2018).
 83. Yang, W. *et al.* Sex differences in GBM revealed by analysis of patient imaging, transcriptome, and survival data. *Sci. Transl. Med.* **11**, eaao5253 (2019).
 84. Trifiletti, D. M. *et al.* Prognostic Implications of Extent of Resection in Glioblastoma: Analysis from a Large Database. *World Neurosurg.* **103**, 330–340 (2017).
 85. Colen, R. R., Wang, J., Singh, S. K., Gutman, D. A. & Zinn, P. O. Glioblastoma: Imaging genomic mapping reveals sex-specific oncogenic associations of cell death.

- Radiology* vol. 275 215–227 (2015).
86. Kfoury, N. *et al.* Cooperative p16 and p21 action protects female astrocytes from transformation. *Acta Neuropathol. Commun.* **6**, 12 (2018).
 87. Conforti, F. *et al.* Cancer immunotherapy efficacy and patients' sex: a systematic review and meta-analysis. *Lancet Oncol.* **19**, 737–746 (2018).
 88. Talal, N. Sex steroid hormones and systemic lupus erythematosus. *Arthritis Rheum.* **24**, 1054–1056 (1981).
 89. Ortona, E. *et al.* Sex-based differences in autoimmune diseases. *Ann. Ist. Super. Sanita* **52**, 205–212 (2016).
 90. Klein, S. L. & Flanagan, K. L. Sex differences in immune responses. *Nature Reviews Immunology* vol. 16 626–638 (2016).
 91. Agostino, P. *et al.* Sex hormones modulate inflammatory mediators produced by macrophages. in *Annals of the New York Academy of Sciences* vol. 876 426–429 (1999).
 92. Bobjer, J., Katrinaki, M., Tsatsanis, C., Lundberg Giwercman, Y. & Giwercman, A. Negative Association between Testosterone Concentration and Inflammatory Markers in Young Men: A Nested Cross-Sectional Study. *PLoS One* **8**, (2013).
 93. Musabak, U. *et al.* Gonadotropin treatment restores in vitro interleukin-1 β and tumour necrosis factor- α production by stimulated peripheral blood mononuclear cells from patients with idiopathic hypogonadotropic hypogonadism. *Clin. Exp. Immunol.* **132**, 265–270 (2003).
 94. Page, S. T. *et al.* Effect of medical castration on CD4+CD25+ T cells, CD8+ T cell IFN- γ expression, and NK cells: A physiological role for testosterone and/or its metabolites. *Am. J. Physiol. - Endocrinol. Metab.* **290**, (2006).
 95. Guneykaya, D. *et al.* Transcriptional and Translational Differences of Microglia from Male and Female Brains. *Cell Rep.* **24**, 2773-2783.e6 (2018).
 96. Lenz, K. M., Nugent, B. M., Haliyur, R. & McCarthy, M. M. Microglia are essential to masculinization of brain and behavior. *J. Neurosci.* **33**, 2761–2772 (2013).
 97. Villa, A. *et al.* Sex-Specific Features of Microglia from Adult Mice. *Cell Rep.* **23**, 3501–3511 (2018).
 98. Rall, D. P. Studies on the Chemotherapy of Experimental Brain Tumors: Development of an Experimental Model. *Cancer Res.* **30**, 2394–2400 (1970).
 99. Szatmári, T. *et al.* Detailed characterization of the mouse glioma 261 tumor model for experimental glioblastoma therapy. *Cancer Sci.* **97**, 546–553 (2006).
 100. Blaszczyk-Thurin, M., O, I. & Ertl, H. C. J. An experimental vaccine expressing wild-type p53 induces protective immunity against glioblastoma cells with high levels of endogenous p53. *Scand. J. Immunol.* **56**, (2002).
 101. Holland, E. C. *et al.* Combined activation of Ras and Akt in neural progenitors induces glioblastoma formation in mice. *Nat. Genet.* **25**, 55–57 (2000).
 102. Guha, A., Feldkamp, M. M., Lau, N., Boss, G. & Pawson, A. Proliferation of human malignant astrocytomas is dependent on Ras activation. *Oncogene* **15**, 2755–2765 (1997).
 103. Plautz, G. E., Touhalisky, J. E. & Shu, S. Treatment of murine gliomas by adoptive transfer of ex vivo activated tumor-draining lymph node cells. *Cell. Immunol.* **178**, 101–107 (1997).
 104. Natsume, A., Mizuno, M., Ryuke, Y. & Yoshida, J. Antitumor effect and cellular immunity activation by murine interferon- β gene transfer against intracerebral glioma in mouse. *Gene Ther.* **6**, 1626–1633 (1999).
 105. Taghian, A. *et al.* Intrinsic radiation sensitivity may not be the major determinant of the poor clinical outcome of glioblastoma multiforme. *Int. J. Radiat. Oncol. Biol. Phys.* **25**,

- 243–249 (1993).
106. Taghian, A. *et al.* In vivo radiation sensitivity of glioblastoma multiforme. *Int. J. Radiat. Oncol. Biol. Phys.* **32**, 99–104 (1995).
 107. Khalsa, J. K. *et al.* Immune phenotyping of diverse syngeneic murine brain tumors identifies immunologically distinct types. *Nat. Commun.* **11**, (2020).
 108. Tang, F. *et al.* mRNA-Seq whole-transcriptome analysis of a single cell. *Nat. Methods* **6**, (2009).
 109. Hashimshony, T., Wagner, F., Sher, N. & Yanai, I. CEL-Seq: Single-Cell RNA-Seq by Multiplexed Linear Amplification. *Cell Rep.* **2**, 666–673 (2012).
 110. Islam, S. *et al.* Highly multiplexed and strand-specific single-cell RNA 5' end sequencing. *Nat. Protoc.* **7**, 813–828 (2012).
 111. Klein, A. M. *et al.* Droplet barcoding for single-cell transcriptomics applied to embryonic stem cells. *Cell* **161**, (2015).
 112. Macosko, E. Z. *et al.* Highly parallel genome-wide expression profiling of individual cells using nanoliter droplets. *Cell* **161**, (2015).
 113. Zheng, G. X. Y. *et al.* Massively parallel digital transcriptional profiling of single cells. *Nat. Commun.* **8**, 14049 (2017).
 114. Peterson, V. M. *et al.* Multiplexed quantification of proteins and transcripts in single cells. *Nat. Biotechnol.* (2017) doi:10.1038/nbt.3973.
 115. Hawkins, T. DNA purification and isolation using magnetic particles. *US Patent* 5,989,071 (1999).
 116. Stoeckius, M. *et al.* Cell Hashing with barcoded antibodies enables multiplexing and doublet detection for single cell genomics. *Genome Biol.* **19**, (2018).
 117. Stuart, T. *et al.* Comprehensive Integration of Single-Cell Data. *Cell* **177**, 1888–1902.e21 (2019).
 118. Butler, A., Hoffman, P., Smibert, P., Papalexi, E. & Satija, R. Integrating single-cell transcriptomic data across different conditions, technologies, and species. *Nat. Biotechnol.* **36**, 411–420 (2018).
 119. Tirosh, I. *et al.* Dissecting the multicellular ecosystem of metastatic melanoma by single-cell RNA-seq. *Science* **352**, 189–96 (2016).
 120. Van Der Maaten, L. & Hinton, G. Visualizing data using t-SNE. *J. Mach. Learn. Res.* **9**, 2579–2625 (2008).
 121. McInnes, L., Healy, J., Saul, N. & Großberger, L. UMAP: Uniform Manifold Approximation and Projection. *J. Open Source Softw.* **3**, 861 (2018).
 122. Yu, G., Wang, L. G., Han, Y. & He, Q. Y. ClusterProfiler: An R package for comparing biological themes among gene clusters. *Omi. A J. Integr. Biol.* **16**, 284–287 (2012).
 123. 10x Genomics. Barcode Whitelist for Custom Feature Barcoding conjugates (Document CG000193) RevA.
https://assets.ctfassets.net/an68im79xiti/2jfcmwtryKsMq4AQqQcIS/539b681f94d6d5e1f3815d1817ce5448/CG000193_Barcode_Whitelist_forCustom_Feature_Barcoding_conjugates_RevA.txt.
 124. 10x Genomics. Cell Surface Protein Labeling for Single Cell RNA Sequencing Protocols RevB. *Demonstrated Protocol*
https://assets.ctfassets.net/an68im79xiti/6p0emIeLO8bsxinEbKgcF/275a5752f4e4347f75a1f649bd824463/CG000149_DemonstratedProtocol_CellSurfaceProteinLabeling_RevB.pdf.
 125. Rusinova, I. *et al.* INTERFEROME v2.0: An updated database of annotated interferon-regulated genes. *Nucleic Acids Res.* **41**, (2013).
 126. Schuyler, R. P. *et al.* Minimizing Batch Effects in Mass Cytometry Data. *Front.*

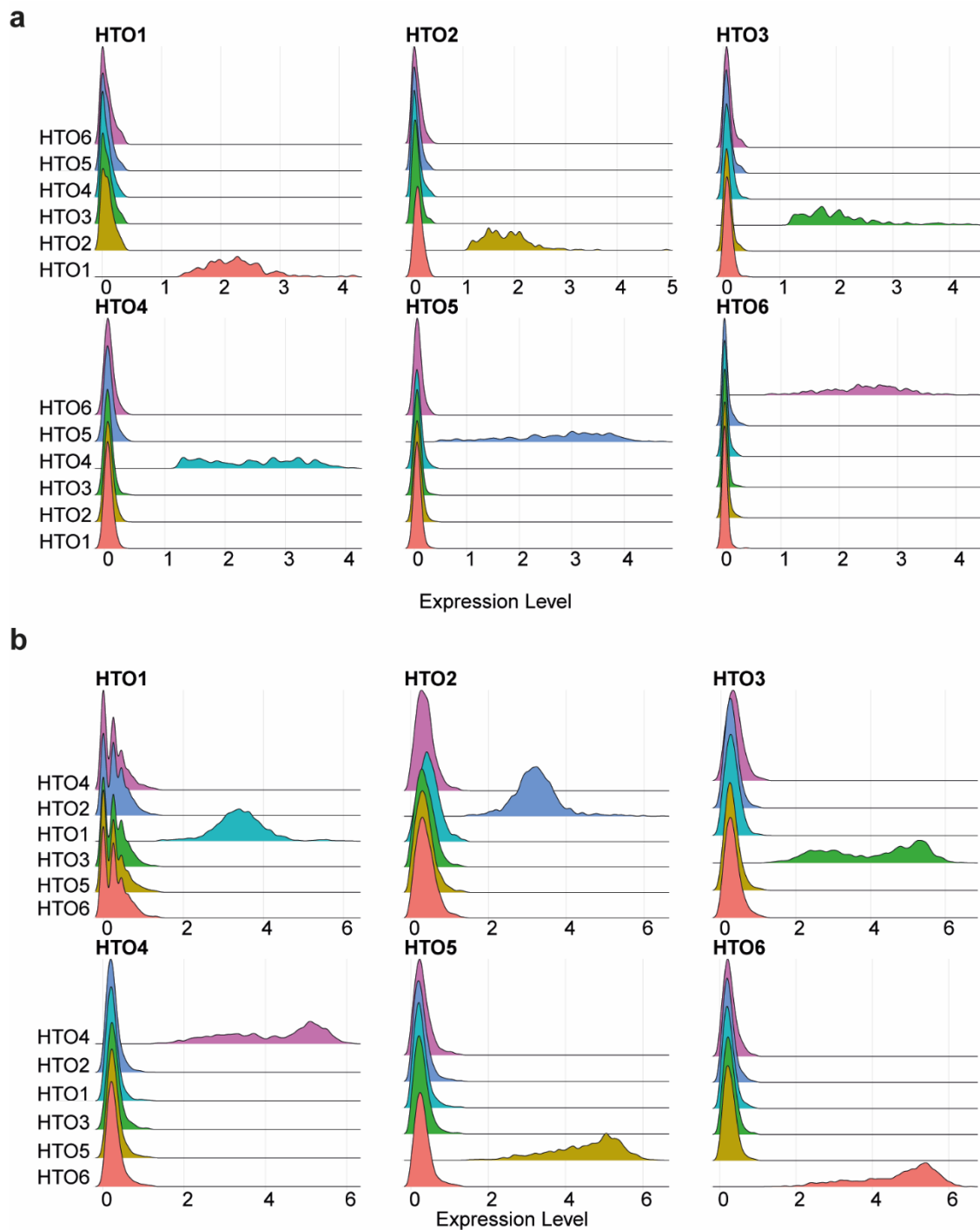
- Immunol.* **10**, (2019).
127. Nowicka, M. *et al.* CyTOF workflow: differential discovery in high-throughput high-dimensional cytometry datasets. *F1000Research* **6**, 748 (2019).
 128. Levine, J. H. *et al.* Data-Driven Phenotypic Dissection of AML Reveals Progenitor-like Cells that Correlate with Prognosis. *Cell* **162**, 184–197 (2015).
 129. Valero-Mora, P. M. ggplot2: Elegant Graphics for Data Analysis. *J. Stat. Softw.* **35**, (2010).
 130. Gu, Z., Eils, R. & Schlesner, M. Complex heatmaps reveal patterns and correlations in multidimensional genomic data. *Bioinformatics* **32**, 2847–2849 (2016).
 131. Oh, T. *et al.* Immunocompetent murine models for the study of glioblastoma immunotherapy. *Journal of Translational Medicine* vol. 12 107 (2014).
 132. What is the maximum number of cells that can be profiled?
<https://kb.10xgenomics.com/hc/en-us/articles/360001378811-What-is-the-maximum-number-of-cells-that-can-be-profiled->.
 133. Matcovitch-Natan, O. *et al.* Microglia development follows a stepwise program to regulate brain homeostasis. *Science (80-.)*. **353**, aad8670 (2016).
 134. Kawai, K. *et al.* CD11b-mediated migratory property of peripheral blood B cells. *J. Allergy Clin. Immunol.* **116**, 192–197 (2005).
 135. McFarland, H. I., Nahill, S. R., Maciaszek, J. W. & Welsh, R. M. CD11b (Mac-1): a marker for CD8+ cytotoxic T cell activation and memory in virus infection. *J. Immunol.* **149**, 1326–33 (1992).
 136. Hickman, S. E. *et al.* The microglial sensome revealed by direct RNA sequencing. *Nat. Neurosci.* **16**, 1896–1905 (2013).
 137. Van Hove, H. *et al.* A single-cell atlas of mouse brain macrophages reveals unique transcriptional identities shaped by ontogeny and tissue environment. *Nat. Neurosci.* **22**, 1021–1035 (2019).
 138. Murphy, K., Janeway, Charles Alderson, J., Travers, P. & Walport, M. J. S. *Janeway's Immunobiology*. (New York : Garland Science, 2012).
 139. Zhao, Y. *et al.* The immunological function of CD52 and its targeting in organ transplantation. *Inflammation Research* vol. 66 571–578 (2017).
 140. Przanowski, P., Loska, S., Cysewski, D., Dabrowski, M. & Kaminska, B. ISG'ylation increases stability of numerous proteins including Stat1, which prevents premature termination of immune response in LPS-stimulated microglia. *Neurochem. Int.* **112**, 227–233 (2018).
 141. Goldmann, T. *et al.* USP 18 lack in microglia causes destructive interferonopathy of the mouse brain. *EMBO J.* **34**, 1612–1629 (2015).
 142. Farhad, M., Rolig, A. S. & Redmond, W. L. The role of Galectin-3 in modulating tumor growth and immunosuppression within the tumor microenvironment. *OncImmunity* vol. 7 e1434467 (2018).
 143. MacKinnon, A. C. *et al.* Regulation of Alternative Macrophage Activation by Galectin-3. *J. Immunol.* **180**, 2650–2658 (2008).
 144. Riol-Blanco, L. *et al.* The Chemokine Receptor CCR7 Activates in Dendritic Cells Two Signaling Modules That Independently Regulate Chemotaxis and Migratory Speed. *J. Immunol.* **174**, (2005).
 145. Saban, D. R. The chemokine receptor CCR7 expressed by dendritic cells: A key player in corneal and ocular surface inflammation. *Ocular Surface* vol. 12 (2014).
 146. Merad, M., Sathe, P., Helft, J., Miller, J. & Mortha, A. The dendritic cell lineage: Ontogeny and function of dendritic cells and their subsets in the steady state and the inflamed setting. *Annual Review of Immunology* vol. 31 563–604 (2013).
 147. Schröder, B. The multifaceted roles of the invariant chain CD74 - More than just a

- chaperone. *Biochimica et Biophysica Acta - Molecular Cell Research* vol. 1863 (2016).
148. Wang, X. & Lin, Y. Tumor necrosis factor and cancer, buddies or foes? *Acta Pharmacologica Sinica* vol. 29 1275–1288 (2008).
 149. Jaitin, D. A. *et al.* Lipid-Associated Macrophages Control Metabolic Homeostasis in a Trem2-Dependent Manner. *Cell* **178**, 686-698.e14 (2019).
 150. Hammond, T. R. *et al.* Single-Cell RNA Sequencing of Microglia throughout the Mouse Lifespan and in the Injured Brain Reveals Complex Cell-State Changes. *Immunity* **50**, (2019).
 151. Li, Q. *et al.* Developmental Heterogeneity of Microglia and Brain Myeloid Cells Revealed by Deep Single-Cell RNA Sequencing. *Neuron* **101**, 207-223.e10 (2019).
 152. Xu, L., Yu, W., Xiao, H. & Lin, K. BIRC5 is a prognostic biomarker associated with tumor immune cell infiltration. *Sci. Rep.* **11**, (2021).
 153. Yu, H., King, R. W., Peters, J. M. & Kirschner, M. W. Identification of a novel ubiquitin-conjugating enzyme involved in mitotic cyclin degradation. *Curr. Biol.* **6**, 455–466 (1996).
 154. Cannon, J. P., O’Driscoll, M. & Litman, G. W. Specific lipid recognition is a general feature of CD300 and TREM molecules. *Immunogenetics* **64**, 39–47 (2012).
 155. Yeh, F. L., Wang, Y., Tom, I., Gonzalez, L. C. & Sheng, M. TREM2 Binds to Apolipoproteins, Including APOE and CLU/APOJ, and Thereby Facilitates Uptake of Amyloid-Beta by Microglia. *Neuron* **91**, 328–340 (2016).
 156. Atagi, Y. *et al.* Apolipoprotein E is a ligand for triggering receptor expressed on myeloid cells 2 (TREM2). *J. Biol. Chem.* **290**, 26043–26050 (2015).
 157. Keren-Shaul, H. *et al.* A Unique Microglia Type Associated with Restricting Development of Alzheimer’s Disease. *Cell* **169**, 1276-1290.e17 (2017).
 158. Wang, X. Q. *et al.* Overexpression of TREM2 enhances glioma cell proliferation and invasion: A therapeutic target in human glioma. *Oncotarget* **7**, 2354–2366 (2016).
 159. Zhang, X., Wang, W., Li, P., Wang, X. & Ni, K. High TREM2 expression correlates with poor prognosis in gastric cancer. *Hum. Pathol.* **72**, 91–99 (2018).
 160. Yao, Y. *et al.* TREM-2 serves as a negative immune regulator through Syk pathway in an IL-10 dependent manner in lung cancer. *Oncotarget* **7**, 29620–29634 (2016).
 161. Clarke, E. V., Weist, B. M., Walsh, C. M. & Tenner, A. J. Complement protein C1q bound to apoptotic cells suppresses human macrophage and dendritic cell-mediated Th17 and Th1 T cell subset proliferation. *J. Leukoc. Biol.* **97**, (2015).
 162. Fraser, D. A., Laust, A. K., Nelson, E. L. & Tenner, A. J. C1q Differentially Modulates Phagocytosis and Cytokine Responses during Ingestion of Apoptotic Cells by Human Monocytes, Macrophages, and Dendritic Cells. *J. Immunol.* **183**, (2009).
 163. Tamoutounour, S. *et al.* Origins and functional specialization of macrophages and of conventional and monocyte-derived dendritic cells in mouse skin. *Immunity* **39**, 925–938 (2013).
 164. Plantinga, M. *et al.* Conventional and Monocyte-Derived CD11b+ Dendritic Cells Initiate and Maintain T Helper 2 Cell-Mediated Immunity to House Dust Mite Allergen. *Immunity* **38**, (2013).
 165. Sichen, D. *et al.* IRF8 Transcription Factor Controls Survival and Function of Terminally Differentiated Conventional and Plasmacytoid Dendritic Cells, Respectively. *Immunity* **45**, (2016).
 166. Fukao, T. *et al.* Inducible Expression of Stat4 in Dendritic Cells and Macrophages and Its Critical Role in Innate and Adaptive Immune Responses. *J. Immunol.* **166**, (2001).
 167. Mrdjen, D. *et al.* High-Dimensional Single-Cell Mapping of Central Nervous System Immune Cells Reveals Distinct Myeloid Subsets in Health, Aging, and Disease. *Immunity* **48**, (2018).

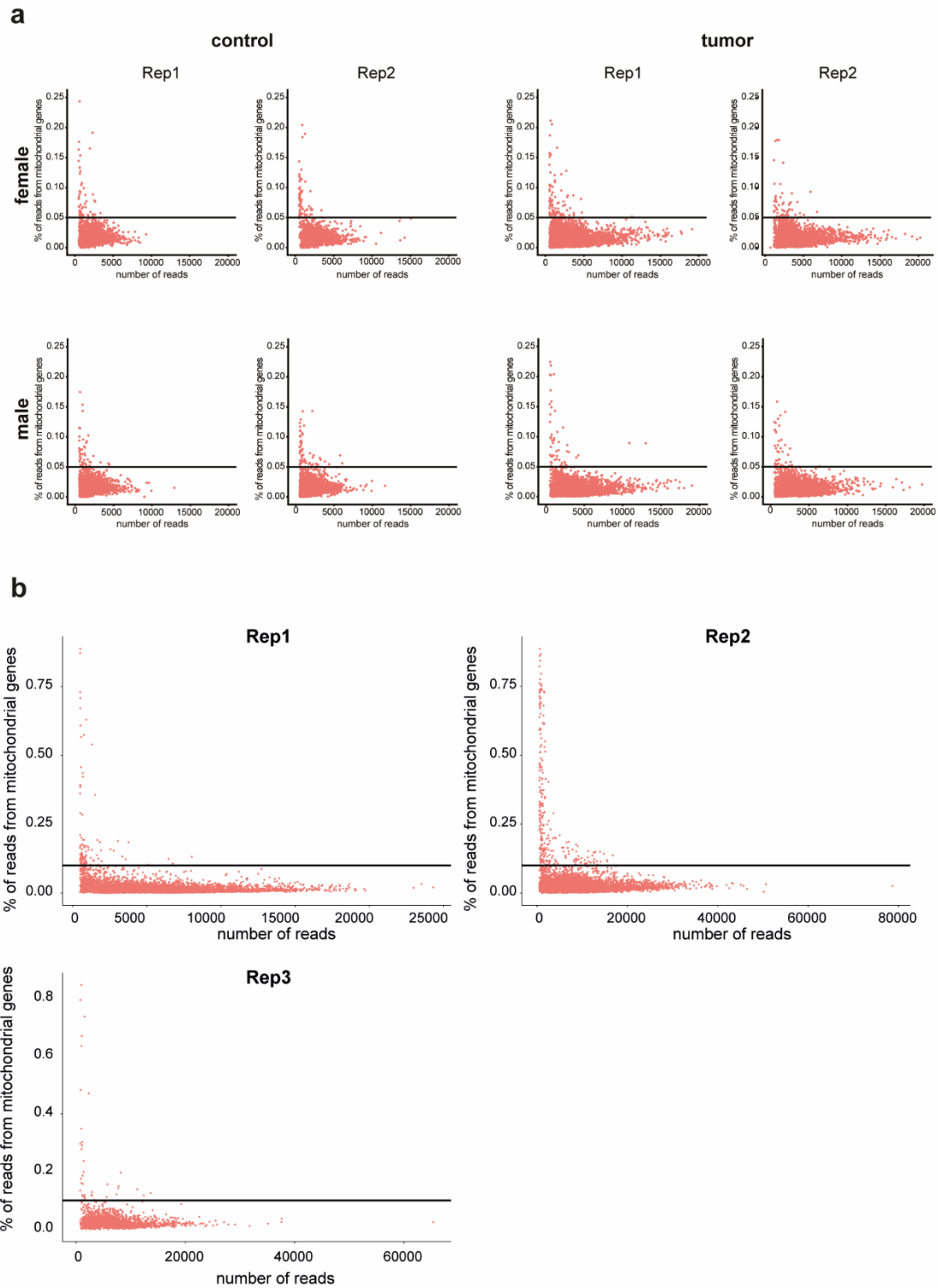
168. Van Hove, H. *et al.* A single-cell atlas of mouse brain macrophages reveals unique transcriptional identities shaped by ontogeny and tissue environment. *Nat. Neurosci.* **22**, 1021–1035 (2019).
169. Elmore, M. R. P. *et al.* Colony-stimulating factor 1 receptor signaling is necessary for microglia viability, unmasking a microglia progenitor cell in the adult brain. *Neuron* **82**, 380–397 (2014).
170. Reyes, R., Cardeños, B., Machado-Pineda, Y. & Cabañas, C. Tetraspanin CD9: A key regulator of cell adhesion in the immune system. *Frontiers in Immunology* vol. 9 (2018).
171. Santer, D. M., Wiedeman, A. E., Teal, T. H., Ghosh, P. & Elkon, K. B. Plasmacytoid Dendritic Cells and C1q Differentially Regulate Inflammatory Gene Induction by Lupus Immune Complexes. *J. Immunol.* **188**, (2012).
172. Yednock, T. A. *et al.* Prevention of experimental autoimmune encephalomyelitis by antibodies against $\alpha 4\beta 1$ integrin. *Nature* **356**, 63–66 (1992).
173. Akkari, L. *et al.* Dynamic changes in glioma macrophage populations after radiotherapy reveal CSF-1R inhibition as a strategy to overcome resistance. *Sci. Transl. Med.* **12**, (2020).
174. Jorgovanovic, D., Song, M., Wang, L. & Zhang, Y. Roles of IFN- γ in tumor progression and regression: A review. *Biomarker Research* vol. 8 (2020).
175. Roura, A. J. *et al.* Identification of the immune gene expression signature associated with recurrence of high-grade gliomas. *J. Mol. Med.* **99**, 241–255 (2021).
176. Zhu, C. *et al.* Development and validation of an interferon signature predicting prognosis and treatment response for glioblastoma. *Oncoimmunology* **8**, (2019).
177. Zhao, P. *et al.* The imbalance in the complement system and its possible physiological mechanisms in patients with lung cancer. *BMC Cancer* **19**, (2019).
178. Stojan, G. & Petri, M. Anti-C1q in systemic lupus erythematosus. *Lupus* **25**, (2016).
179. Müller, S. *et al.* Single-cell profiling of human gliomas reveals macrophage ontogeny as a basis for regional differences in macrophage activation in the tumor microenvironment. *Genome Biol.* (2017) doi:10.1186/s13059-017-1362-4.
180. Reardon, D. A. *et al.* Effect of Nivolumab vs Bevacizumab in Patients with Recurrent Glioblastoma: The CheckMate 143 Phase 3 Randomized Clinical Trial. *JAMA Oncol.* **6**, 1003–1010 (2020).
181. Gabrusiewicz, K. *et al.* Macrophage Ablation Reduces M2-Like Populations and Jeopardizes Tumor Growth in a MAFIA-Based Glioma Model. *Neoplasia (United States)* **17**, (2015).
182. Yan, D. *et al.* Inhibition of colony stimulating factor-1 receptor abrogates microenvironment-mediated therapeutic resistance in gliomas. *Oncogene* **36**, 6049–6058 (2017).
183. Butowski, N. *et al.* Orally administered colony stimulating factor 1 receptor inhibitor PLX3397 in recurrent glioblastoma: An Ivy Foundation Early Phase Clinical Trials Consortium phase II study. *Neuro. Oncol.* **18**, 557–564 (2016).
184. Pyonteck, S. M. *et al.* CSF-1R inhibition alters macrophage polarization and blocks glioma progression. *Nat. Med.* **19**, (2013).
185. Sousa, C., Biber, K. & Michelucci, A. Cellular and molecular characterization of microglia: A unique immune cell population. *Frontiers in Immunology* vol. 8 198 (2017).
186. Masuda, T. *et al.* Spatial and temporal heterogeneity of mouse and human microglia at single-cell resolution. *Nature* **566**, 388–392 (2019).
187. Haage, V. *et al.* Comprehensive gene expression meta-analysis identifies signature genes that distinguish microglia from peripheral monocytes/macrophages in health and

- glioma. *Acta Neuropathol. Commun.* **7**, 20 (2019).
188. Jordão, M. J. C. *et al.* Neuroimmunology: Single-cell profiling identifies myeloid cell subsets with distinct fates during neuroinflammation. *Science (80-.)*. **363**, eaat7554 (2019).
 189. Goldmann, T. *et al.* Origin, fate and dynamics of macrophages at central nervous system interfaces. *Nat. Immunol.* **17**, 797–805 (2016).
 190. Ziegler-Heitbrock, L. *et al.* Nomenclature of monocytes and dendritic cells in blood. *Blood* vol. 116 e74–e80 (2010).
 191. Fleming, T. J., Fleming, M. L. & Malek, T. R. Selective expression of Ly-6G on myeloid lineage cells in mouse bone marrow. RB6-8C5 mAb to granulocyte-differentiation antigen (Gr-1) detects members of the Ly-6 family. *J. Immunol.* **151**, 2399–408 (1993).
 192. Musumeci, A., Lutz, K., Winheim, E. & Krug, A. B. What makes a PDC: Recent advances in understanding plasmacytoid DC development and heterogeneity. *Frontiers in Immunology* vol. 10 1222 (2019).
 193. Crinier, A. *et al.* High-Dimensional Single-Cell Analysis Identifies Organ-Specific Signatures and Conserved NK Cell Subsets in Humans and Mice. *Immunity* **49**, 971-986.e5 (2018).

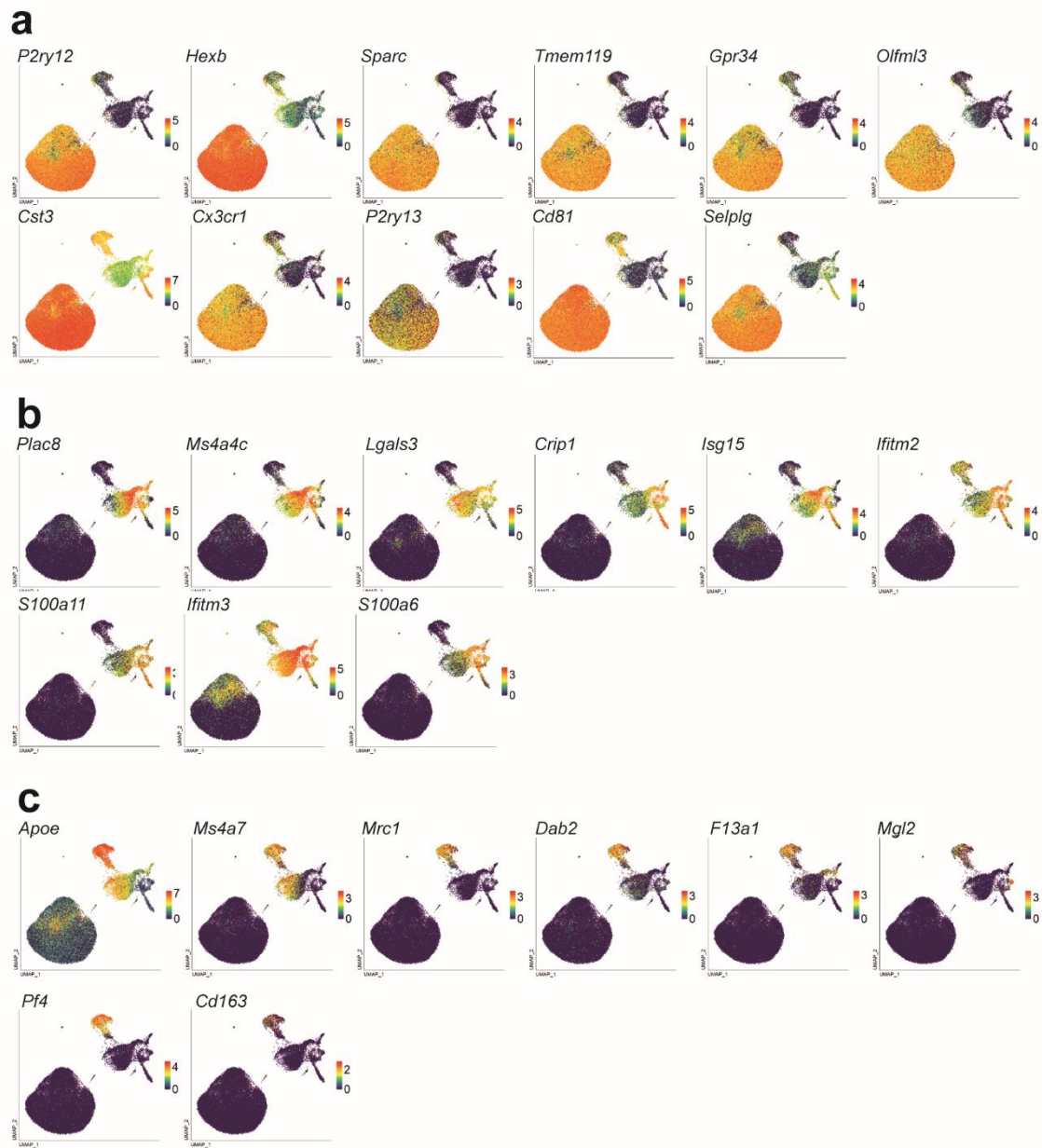
Supplementary figures



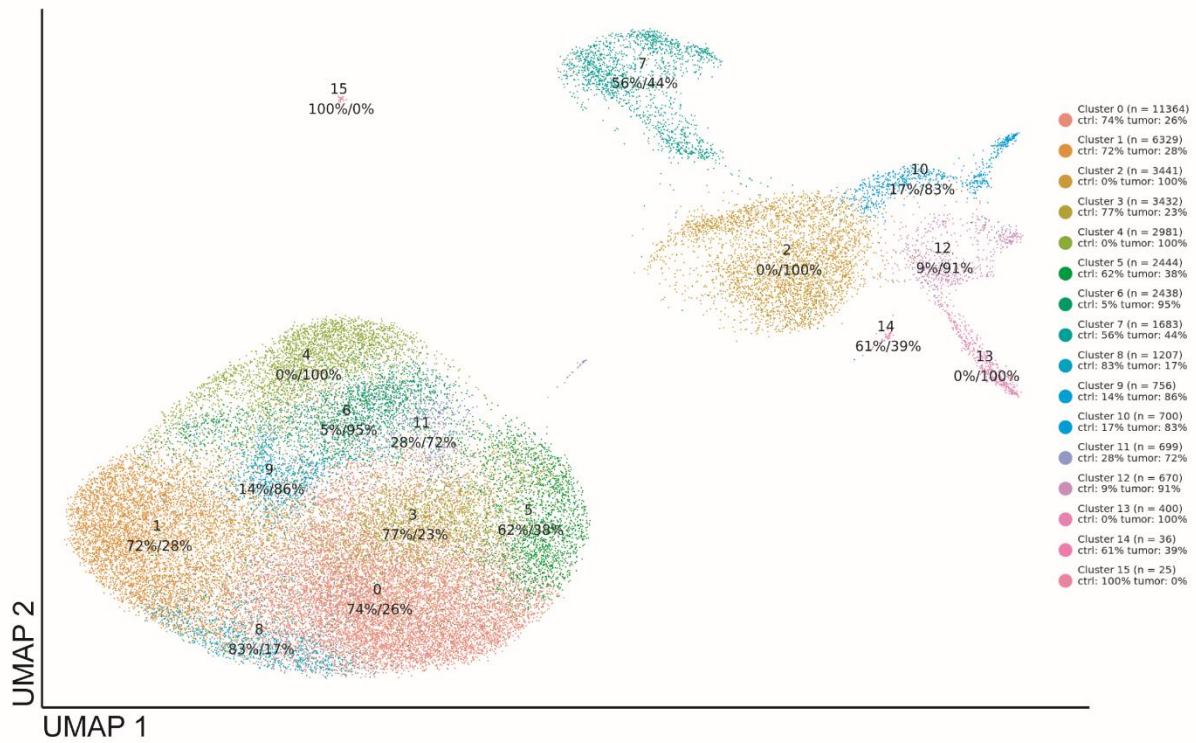
Supplementary Figure 1 | Ridge plots demonstrating separation of the CITE-seq samples with the HTO barcodes in replicate 2 (**a**) and replicate 3 (**b**). Replicate 1 is shown in the Figure 6.6 c.



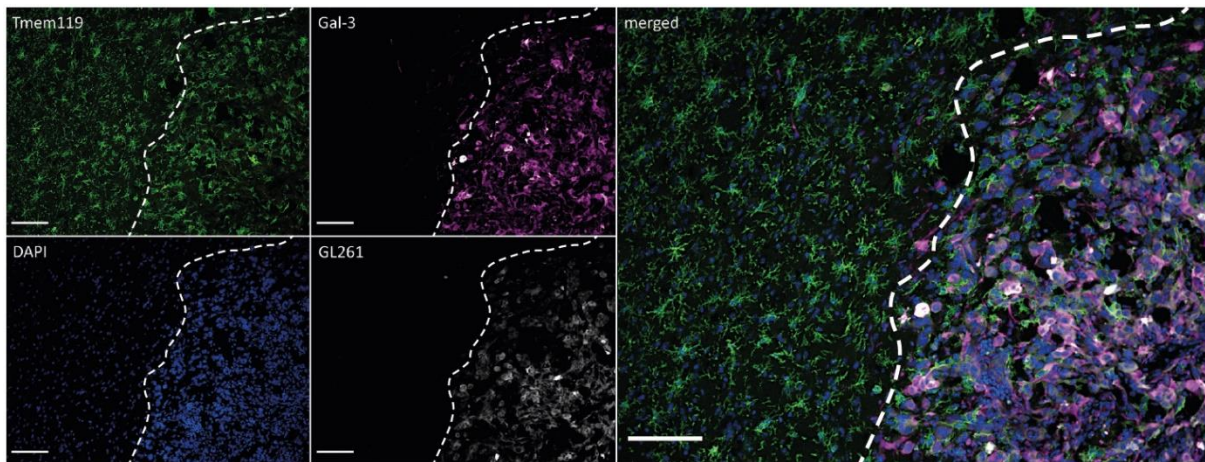
Supplementary Figure 2 | Scatter plots demonstrating obtained percentage of reads aligned to the mitochondrial genes, compared to the number of total reads in the **(a)** scRNA-seq and **(b)** CITE-seq. Horizontal line indicates an adapted filtering threshold (cells having $>5\%$ - scRNA-seq, $>10\%$ CITE-seq mitochondrial reads were excluded from the analysis).



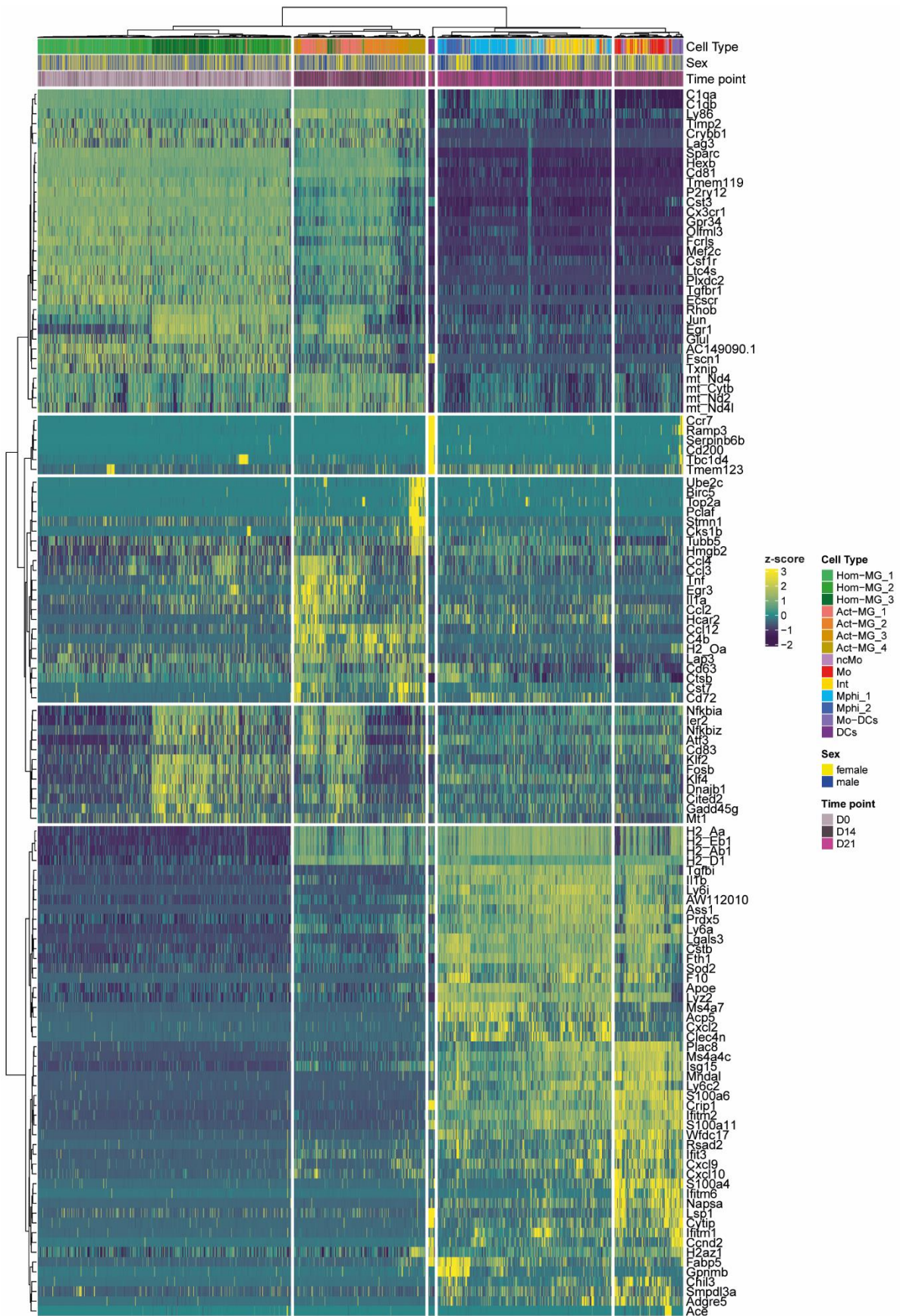
Supplementary Figure 3 | Feature plots demonstrating expression of top highly expressed genes of MG, Mo/M Φ and BAMs groups.



Supplementary Figure 4 | UMAP plot demonstrating clusters of the re-clustered groups (MG, Mo/MΦ and BAMs) for combined conditions.

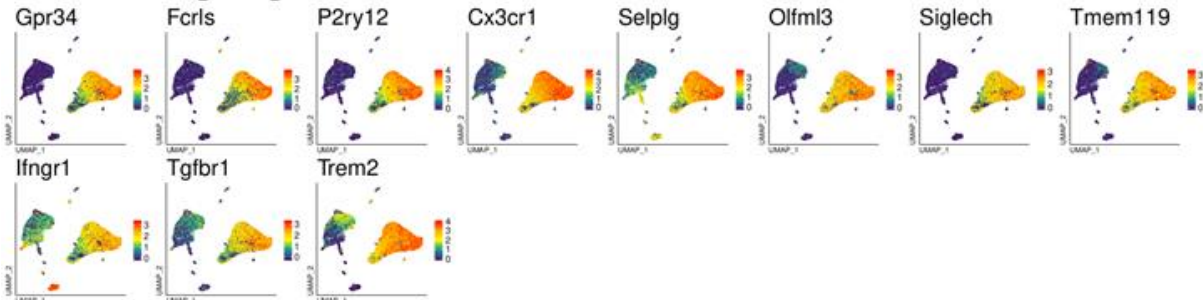


Supplementary Figure 5 | Immunohistochemical staining for microglia (Tmem119+) and Mo/MΦ (Gal-3+) shows the localization of specific immune cells within the tumor and its surroundings in male animal (for female see Figure 6.9e); a dashed line marks the tumor edge; scale – 100 μm.

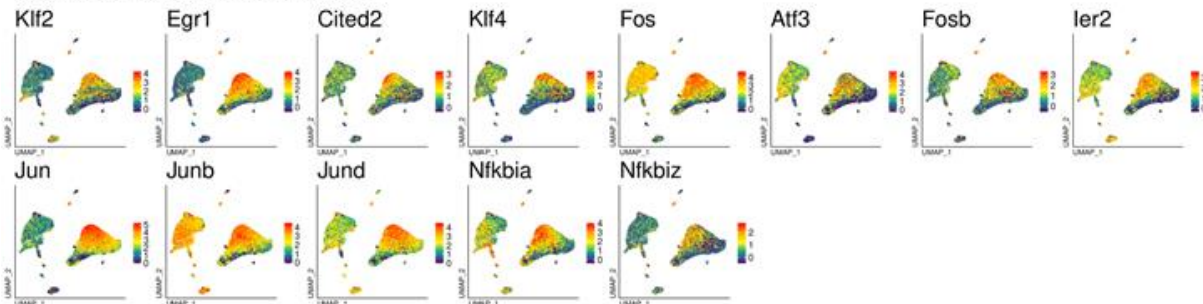


Supplementary Figure 6 | Heatmap of the top expressed genes in cell cluster from the major identified cell populations in the CITE-seq analysis.

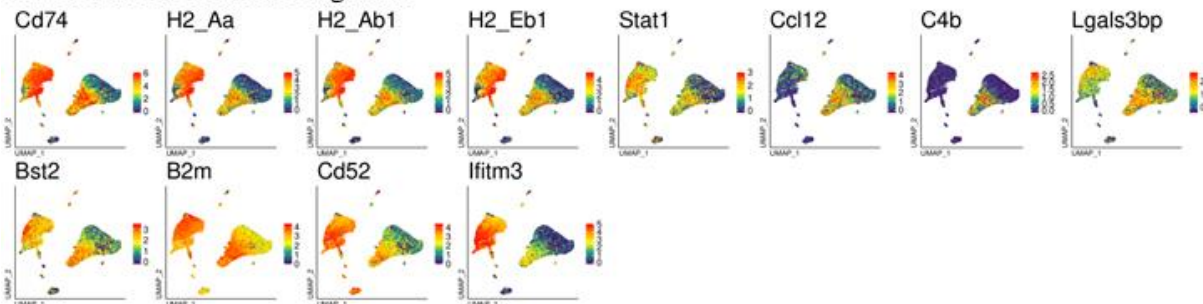
Canonical microglia signature



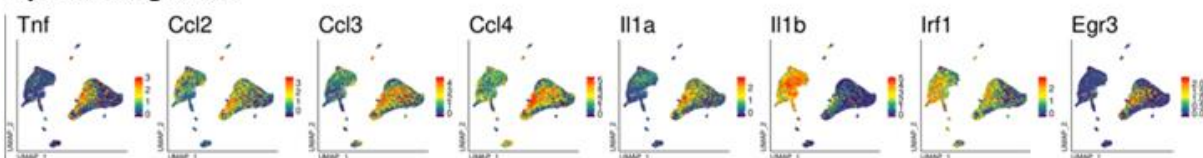
Transcription Factor signature



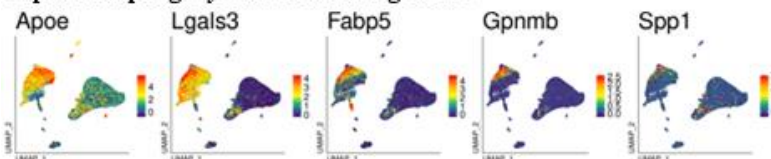
Tumor-induced activation signature



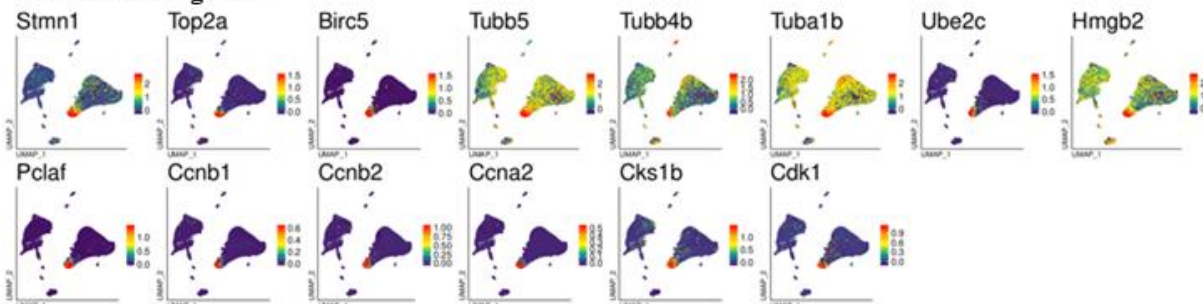
Cytokines signature



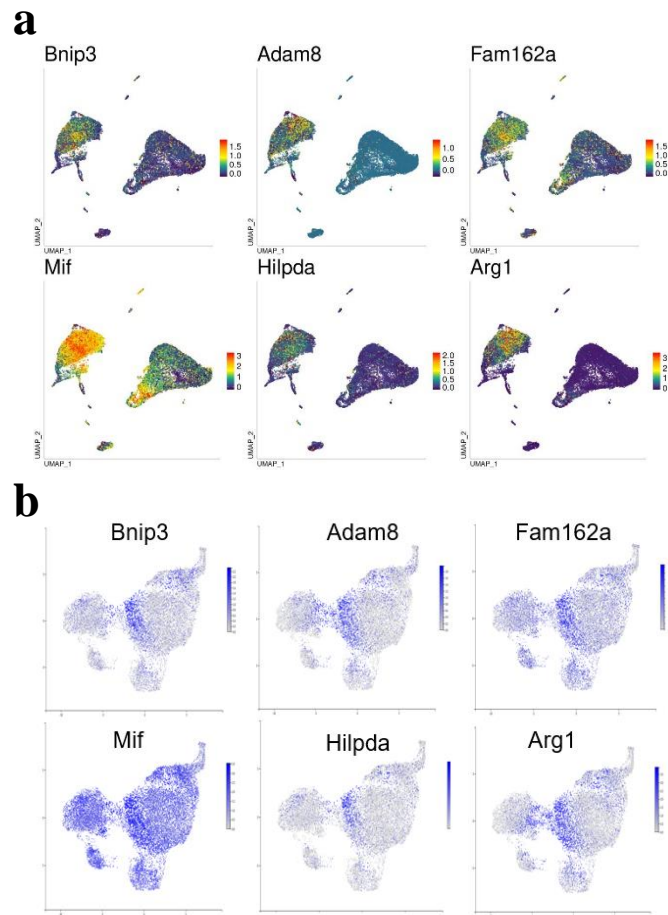
Lipid and phagocytosis-related signature



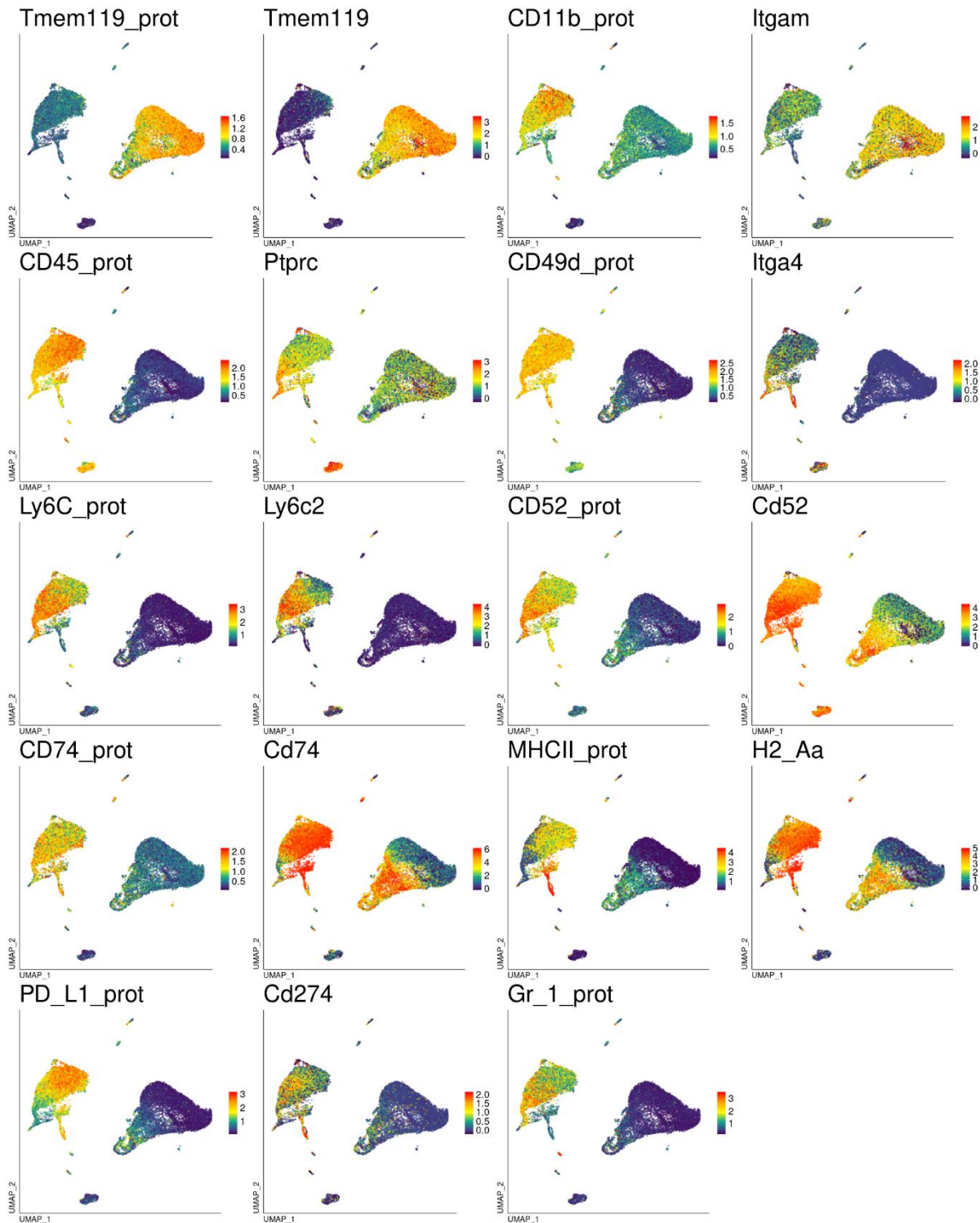
Proliferation signature



Supplementary Figure 7 | Feature plots demonstrating the distribution of expression level of each gene contained in the transcriptional microglia scores in Figure 6.15c, across all the CD11b+ cells included in the CITE-seq analysis.



Supplementary Figure 8 | Feature plots demonstrating the distribution of expression level of genes belonging to “hypoxia” signature reported by Antunes et al . 2021 in **(a)** our CITE-seq a data set **(b)** scRNA-seq from murine glioma TAM data set from Antunes et al. (2021). The feature plots for the Antunes et al. (2021) data set were produced using the interactive web page provided by the authors <https://www.brainimmuneatlas.org/> .



Supplementary Figure 9 | Feature plots depicting expression level of all proteins from the CITE-seq protein panel along with the expression level of the encoding genes. For Gr-1 only protein expression is shown, as the gene *Ly6g* gene was not found to be expressed in the CITE-seq dataset.

Supplementary material

Supplementary Table 1 | List of the literature-based markers used to create an immune marker panel for characterization of cell identity of clusters obtained in scRNA-seq and CITE-seq analysis.

Gene	Target group	Ref.	Gene	Target group	Ref.
<i>Ptprc</i>	hematopoietic cells	138	<i>Fpr3</i>	macrophages	39
<i>Itgam</i>	myeloid cells	138	<i>Kynu</i>	macrophages	39
<i>Cd14</i>	myelomonocytic cells	138	<i>S100a11</i>	macrophages	39
<i>Tmem119</i>	microglia	61,185,186	<i>S100a6</i>	macrophages	39
<i>Cx3cr1</i>	microglia	185	<i>Tgm2</i>	GAMs	50
<i>P2ry12</i>	microglia	61,185	<i>Gpnmb</i>	GAMs	50
<i>P2ry13</i>	microglia	61,185	<i>Emilin2</i>	macrophages in high-grade glioma	187
<i>Gpr34</i>	microglia	61,185	<i>Gda</i>	macrophages in high-grade glioma	187
<i>Olfml3</i>	microglia	185	<i>Hp</i>	macrophages in high-grade glioma	187
<i>Selplg</i>	microglia	185,186	<i>Sell</i>	macrophages in high-grade glioma	187
<i>Sparc</i>	microglia	185	<i>Cd163</i>	Border Associated Macrophages	188
<i>Fcrls</i>	microglia	61,185	<i>Mrc1</i>	Border Associated Macrophages	188,189
<i>Siglech</i>	microglia	185	<i>Lyve1</i>	Border Associated Macrophages	188
<i>Slc2a5</i>	microglia	185,186	<i>Siglec1</i>	Border Associated Macrophages	188
<i>Pf4</i>	microglia progenitors	133	<i>Ly6c1</i>	monocytes	190
<i>F13a1</i>	microglia progenitors	133	<i>Ly6c2</i>	monocytes	190
<i>Lyz2</i>	microglia progenitors	133	<i>Ccr2</i>	classical monocytes	190
<i>Ifit3</i>	microglia progenitors	133	<i>Spn</i>	non-classical monocytes	190
<i>Mcm5</i>	early microglia	133	<i>Ace</i>	non-classical monocytes	77
<i>Dab2</i>	early microglia	133	<i>Ear2</i>	non-classical monocytes	77
<i>Cxcr2</i>	pre-microglia	133	<i>Ly6g</i>	Granulocytes	191
<i>Scd2</i>	pre-microglia	133	<i>Cd24a</i>	granulocytes/ dendritic cells	191
<i>Psat1</i>	pre-microglia	133	<i>Itgax</i>	dendritic cells	192
<i>Csf1</i>	pre-microglia	133	<i>Bst2</i>	plasmacytoid dendritic cells	192
<i>Crybb1</i>	pre-microglia	133	<i>Ncam1</i>	NK cells	193
<i>Fcrls</i>	pre-microglia	133	<i>Klrb1c</i>	NK cells	193
<i>Selplg</i>	adult microglia	133	<i>Klrk1</i>	NK cells	193
<i>Mafb</i>	adult microglia	133	<i>Ncr1</i>	NK cells	193
<i>Pmepal</i>	adult microglia	133	<i>Cd2</i>	T-cells, NK cells	138
<i>Cd14</i>	adult microglia	133	<i>Cd3d</i>	T cells	138
<i>Lpl</i>	disease associated microglia	157	<i>Cd3e</i>	T cells	138
<i>Cst7</i>	disease associated microglia	133,157	<i>Cd3g</i>	T cells	138
<i>Itga4</i>	macrophages	39,59	<i>Cd4</i>	helper T cell	138
<i>Tgfb</i>	macrophages	38,39	<i>Cd8a</i>	cytotoxic T cells	138
<i>Ifitm2</i>	macrophages	38,39	<i>Cd8b1</i>	cytotoxic T cells	138
<i>Ifitm3</i>	macrophages	38	<i>Cd19</i>	B-cells	138
<i>Tagln2</i>	macrophages	38	<i>Ms4a1</i>	B-cells	138
<i>F13a1</i>	macrophages	38	<i>Sdc1</i>	B-cells	138

Supplementary Table 2 | List of up to top 30 differentially expressed genes in the MG clusters presented on Figure 6.7. Each page corresponds to an individual condition (male control, male tumor, female control, female tumor).

male control							
condition	cluster	Gene.name	avg_logFC	condition	cluster	Gene.name	avg_logFC
m_ctrl	MG1	<i>P2ry12</i>	0.29	m_ctrl	MG3	<i>Zscan26</i>	0.69
m_ctrl	MG1	<i>Cst3</i>	0.29	m_ctrl	MG3	<i>Skil</i>	0.58
m_ctrl	MG1	<i>Crybb1</i>	0.27	m_ctrl	MG3	<i>Abhd2</i>	0.52
m_ctrl	MG1	<i>Pros1</i>	0.26	m_ctrl	MG3	<i>Pdcd4</i>	0.51
m_ctrl	MG2	<i>Fos</i>	1.54	m_ctrl	MG3	<i>Dpysl2</i>	0.49
m_ctrl	MG2	<i>Egr1</i>	1.53	m_ctrl	MG3	<i>Cdk6</i>	0.45
m_ctrl	MG2	<i>Jun</i>	1.52	m_ctrl	MG3	<i>Tubb5</i>	0.43
m_ctrl	MG2	<i>Ier2</i>	1.32	m_ctrl	MG3	<i>Dusp3</i>	0.41
m_ctrl	MG2	<i>Dusp1</i>	1.32	m_ctrl	MG3	<i>Kdm6b</i>	0.37
m_ctrl	MG2	<i>Jund</i>	1.28	m_ctrl	MG3	<i>Gm2a</i>	0.36
m_ctrl	MG2	<i>Btg2</i>	1.28	m_ctrl	MG3	<i>Klf13</i>	0.35
m_ctrl	MG2	<i>Klf2</i>	1.21	m_ctrl	MG3	<i>Supt16</i>	0.34
m_ctrl	MG2	<i>Atf3</i>	1.20	m_ctrl	MG3	<i>Prune2</i>	0.33
m_ctrl	MG2	<i>Junb</i>	1.15	m_ctrl	MG3	<i>Nav3</i>	0.28
m_ctrl	MG2	<i>Socs3</i>	1.05	m_ctrl	MG3	<i>Gatad1</i>	0.27
m_ctrl	MG2	<i>Zfp36</i>	1.05	m_ctrl	pre-MG	<i>Ccl4</i>	2.62
m_ctrl	MG2	<i>Nfkbia</i>	1.04	m_ctrl	pre-MG	<i>Id2</i>	2.06
m_ctrl	MG2	<i>Ccl4</i>	1.02	m_ctrl	pre-MG	<i>Ccl3</i>	1.98
m_ctrl	MG2	<i>Ier5</i>	1.00	m_ctrl	pre-MG	<i>Lgals3</i>	1.78
m_ctrl	MG2	<i>Cited2</i>	0.94	m_ctrl	pre-MG	<i>Cd83</i>	1.60
m_ctrl	MG2	<i>Rhob</i>	0.88	m_ctrl	pre-MG	<i>Lpl</i>	1.49
m_ctrl	MG2	<i>Ubc</i>	0.85	m_ctrl	pre-MG	<i>Cd63</i>	1.45
m_ctrl	MG2	<i>Ccl3</i>	0.84	m_ctrl	pre-MG	<i>C5ar1</i>	1.43
m_ctrl	MG2	<i>Ppp1r15a</i>	0.72	m_ctrl	pre-MG	<i>Cstb</i>	1.23
m_ctrl	MG2	<i>Gm26532</i>	0.72	m_ctrl	pre-MG	<i>Csf1</i>	1.17
m_ctrl	MG2	<i>Klf6</i>	0.69	m_ctrl	pre-MG	<i>Mt1</i>	1.17
m_ctrl	MG2	<i>Tsc22d3</i>	0.68	m_ctrl	pre-MG	<i>Cxcl16</i>	1.15
m_ctrl	MG2	<i>Dnajb1</i>	0.67	m_ctrl	pre-MG	<i>Gpr84</i>	1.11
m_ctrl	MG2	<i>Gadd45g</i>	0.63	m_ctrl	pre-MG	<i>Mif</i>	1.09
m_ctrl	MG2	<i>Rgs1</i>	0.62	m_ctrl	pre-MG	<i>Plaur</i>	1.07
m_ctrl	MG2	<i>Fosb</i>	0.60	m_ctrl	pre-MG	<i>Cd9</i>	1.07
m_ctrl	MG2	<i>Sgk1</i>	0.54	m_ctrl	pre-MG	<i>Tlr2</i>	1.06
m_ctrl	MG2	<i>Tagap</i>	0.54	m_ctrl	pre-MG	<i>Slc15a3</i>	1.04
m_ctrl	MG2	<i>Ptma</i>	0.45	m_ctrl	pre-MG	<i>Tnf</i>	1.02
m_ctrl	MG3	<i>Bmp2k</i>	1.23	m_ctrl	pre-MG	<i>Cadm1</i>	1.02
m_ctrl	MG3	<i>Bhlhe41</i>	1.22	m_ctrl	pre-MG	<i>Plek</i>	1.00
m_ctrl	MG3	<i>Slc39a1</i>	1.09	m_ctrl	pre-MG	<i>Ctsb</i>	0.98
m_ctrl	MG3	<i>Zfp691</i>	0.99	m_ctrl	pre-MG	<i>Spp1</i>	0.96
m_ctrl	MG3	<i>Notch2</i>	0.96	m_ctrl	pre-MG	<i>Ninj1</i>	0.96
m_ctrl	MG3	<i>Ncoa3</i>	0.89	m_ctrl	pre-MG	<i>Thbs1</i>	0.96
m_ctrl	MG3	<i>Actb</i>	0.83	m_ctrl	pre-MG	<i>Gadd45b</i>	0.94
m_ctrl	MG3	<i>Ptafr</i>	0.80	m_ctrl	pre-MG	<i>Pkm</i>	0.93
m_ctrl	MG3	<i>Nfia</i>	0.78	m_ctrl	pre-MG	<i>Sdc4</i>	0.92
m_ctrl	MG3	<i>Gm32036</i>	0.72	m_ctrl	pre-MG	<i>Cst7</i>	0.91
m_ctrl	MG3	<i>C5ar2</i>	0.71	m_ctrl	pre-MG	<i>Nfkbia</i>	0.90

male tumor							
condition	cluster	Gene.name	avg_logFC	condition	cluster	Gene.name	avg_logFC
m_tumor	MG1	<i>P2ry12</i>	1.18	m_tumor	MG2	<i>Jun</i>	2.00
m_tumor	MG1	<i>Fcrls</i>	1.18	m_tumor	MG2	<i>Egr1</i>	1.84
m_tumor	MG1	<i>Gpr34</i>	1.08	m_tumor	MG2	<i>Ier2</i>	1.61
m_tumor	MG1	<i>Ecsr</i>	1.04	m_tumor	MG2	<i>Klf2</i>	1.61
m_tumor	MG1	<i>Ltc4s</i>	0.97	m_tumor	MG2	<i>Jund</i>	1.52
m_tumor	MG1	<i>Sox4</i>	0.83	m_tumor	MG2	<i>Rhob</i>	1.34
m_tumor	MG1	<i>Slc2a5</i>	0.81	m_tumor	MG2	<i>Btg2</i>	1.33
m_tumor	MG1	<i>Tmem119</i>	0.79	m_tumor	MG2	<i>Ier5</i>	1.28
m_tumor	MG1	<i>Olfml3</i>	0.78	m_tumor	MG2	<i>Fos</i>	1.26
m_tumor	MG1	<i>Sparc</i>	0.77	m_tumor	MG2	<i>Dusp1</i>	1.15
m_tumor	MG1	<i>Pmp22</i>	0.70	m_tumor	MG2	<i>Atf3</i>	1.09
m_tumor	MG1	<i>Syng1</i>	0.68	m_tumor	MG2	<i>Junb</i>	1.07
m_tumor	MG1	<i>Ctsd</i>	0.65	m_tumor	MG2	<i>Dnajb1</i>	1.00
m_tumor	MG1	<i>Serpine2</i>	0.62	m_tumor	MG2	<i>Zfp36</i>	0.96
m_tumor	MG1	<i>Ldhd</i>	0.62	m_tumor	MG2	<i>Nfkb1a</i>	0.93
m_tumor	MG1	<i>Fscn1</i>	0.59	m_tumor	MG2	<i>Cited2</i>	0.90
m_tumor	MG1	<i>Lrba</i>	0.56	m_tumor	MG2	<i>Ccl3</i>	0.90
m_tumor	MG1	<i>Cd81</i>	0.56	m_tumor	MG2	<i>Tsc22d3</i>	0.89
m_tumor	MG1	<i>Ctsl</i>	0.56	m_tumor	MG2	<i>Ccl4</i>	0.89
m_tumor	MG1	<i>Ifi27</i>	0.54	m_tumor	MG2	<i>Ppp1r15a</i>	0.80
m_tumor	MG1	<i>Pros1</i>	0.50	m_tumor	MG2	<i>Sgk1</i>	0.75
m_tumor	MG1	<i>Cd9</i>	0.50	m_tumor	MG2	<i>Gm26532</i>	0.71
m_tumor	MG1	<i>Crybb1</i>	0.49	m_tumor	MG2	<i>Klf6</i>	0.67
m_tumor	MG1	<i>Bmp2k</i>	0.47	m_tumor	MG2	<i>Il1a</i>	0.65
m_tumor	MG1	<i>Tmem37</i>	0.45	m_tumor	MG2	<i>Fosb</i>	0.60
m_tumor	MG1	<i>Lag3</i>	0.45	m_tumor	MG2	<i>Gadd45g</i>	0.59
m_tumor	MG1	<i>Thrsp</i>	0.44	m_tumor	MG2	<i>Icam1</i>	0.56
m_tumor	MG1	<i>Tmem176b</i>	0.44	m_tumor	MG2	<i>Tagap</i>	0.50
m_tumor	MG1	<i>Upk1b</i>	0.42	m_tumor	MG2	<i>Socs3</i>	0.49
m_tumor	MG1	<i>Cadm1</i>	0.42	m_tumor	MG2	<i>Nfkbiz</i>	0.49
m_tumor	MG7	<i>Ccl12</i>	1.50	m_tumor	MG8	<i>Stmn1</i>	2.40
m_tumor	MG7	<i>H2-Oa</i>	0.91	m_tumor	MG8	<i>Pclaf</i>	1.62
m_tumor	MG7	<i>Cst7</i>	0.79	m_tumor	MG8	<i>Hmgb2</i>	1.58
m_tumor	MG7	<i>Lgals3bp</i>	0.77	m_tumor	MG8	<i>Top2a</i>	1.55
m_tumor	MG7	<i>Gm4951</i>	0.76	m_tumor	MG8	<i>Birc5</i>	1.48
m_tumor	MG7	<i>Cd81</i>	0.67	m_tumor	MG8	<i>Hist1h2ap</i>	1.44
m_tumor	MG7	<i>Ly86</i>	0.67	m_tumor	MG8	<i>Tubb5</i>	1.39
m_tumor	MG7	<i>Lag3</i>	0.64	m_tumor	MG8	<i>Ube2c</i>	1.34
m_tumor	MG7	<i>Crybb1</i>	0.64	m_tumor	MG8	<i>Rrm2</i>	1.32
m_tumor	MG7	<i>C4b</i>	0.59	m_tumor	MG8	<i>Hmgn2</i>	1.31
m_tumor	MG7	<i>Cd180</i>	0.57	m_tumor	MG8	<i>Tuba1b</i>	1.28
m_tumor	MG7	<i>Cd9</i>	0.56	m_tumor	MG8	<i>Cks1b</i>	1.23
m_tumor	MG7	<i>Lap3</i>	0.52	m_tumor	MG8	<i>H2afz</i>	1.23
m_tumor	MG7	<i>Serpine2</i>	0.51	m_tumor	MG8	<i>H2afx</i>	1.21
m_tumor	MG7	<i>Timp2</i>	0.50	m_tumor	MG8	<i>Pbk</i>	1.18
m_tumor	MG7	<i>Ctsb</i>	0.47	m_tumor	MG8	<i>Ube2s</i>	1.16
m_tumor	MG7	<i>Spp1</i>	0.47	m_tumor	MG8	<i>Cdk1</i>	1.15
m_tumor	MG7	<i>Ctsd</i>	0.46	m_tumor	MG8	<i>Smc2</i>	1.15
m_tumor	MG7	<i>Ldhd</i>	0.43	m_tumor	MG8	<i>Nusap1</i>	1.07
m_tumor	MG7	<i>Ctsl</i>	0.43	m_tumor	MG8	<i>Smc4</i>	1.07
m_tumor	MG7	<i>Hcar2</i>	0.41	m_tumor	MG8	<i>Ccl12</i>	1.06
m_tumor	MG7	<i>Olfml3</i>	0.41	m_tumor	MG8	<i>Ngp</i>	1.05
m_tumor	MG7	<i>Tor3a</i>	0.39	m_tumor	MG8	<i>H2afv</i>	1.04
m_tumor	MG7	<i>Tmem119</i>	0.39	m_tumor	MG8	<i>Tk1</i>	0.97
m_tumor	MG7	<i>Sparc</i>	0.38	m_tumor	MG8	<i>Cst7</i>	0.97
m_tumor	MG7	<i>Gpr84</i>	0.36	m_tumor	MG8	<i>Ccnb1</i>	0.95
m_tumor	MG7	<i>Cryba4</i>	0.36	m_tumor	MG8	<i>Spc24</i>	0.95
m_tumor	MG7	<i>Ccl3</i>	0.36	m_tumor	MG8	<i>Cenpa</i>	0.93
m_tumor	MG7	<i>Bhlhe41</i>	0.35	m_tumor	MG8	<i>Cdca8</i>	0.93
m_tumor	MG7	<i>Sdf211</i>	0.35	m_tumor	MG8	<i>Cks2</i>	0.93

female control							
condition	cluster	Gene.name	avg_logFC	condition	cluster	Gene.name	avg_logFC
f_ctrl	MG1	<i>Crybb1</i>	0.26	f_ctrl	MG3	<i>Rbm15</i>	0.60
f_ctrl	MG1	<i>Cst3</i>	0.26	f_ctrl	MG3	<i>Cdk6</i>	0.60
f_ctrl	MG2	<i>Jun</i>	1.75	f_ctrl	MG3	<i>Clasp2</i>	0.49
f_ctrl	MG2	<i>Ier2</i>	1.73	f_ctrl	MG3	<i>Pdcd4</i>	0.48
f_ctrl	MG2	<i>Klf2</i>	1.62	f_ctrl	MG3	<i>Dusp3</i>	0.47
f_ctrl	MG2	<i>Egr1</i>	1.60	f_ctrl	MG3	<i>Pan3</i>	0.46
f_ctrl	MG2	<i>Fos</i>	1.57	f_ctrl	MG3	<i>Tubb5</i>	0.43
f_ctrl	MG2	<i>Dusp1</i>	1.56	f_ctrl	MG3	<i>Rpgrip1</i>	0.42
f_ctrl	MG2	<i>Btg2</i>	1.55	f_ctrl	MG3	<i>Kdm6b</i>	0.37
f_ctrl	MG2	<i>Junb</i>	1.47	f_ctrl	MG3	<i>Gm2a</i>	0.36
f_ctrl	MG2	<i>Jund</i>	1.44	f_ctrl	MG5	<i>Plp1</i>	2.38
f_ctrl	MG2	<i>Nfkbia</i>	1.26	f_ctrl	MG5	<i>Ly6a</i>	1.83
f_ctrl	MG2	<i>Atf3</i>	1.18	f_ctrl	MG5	<i>Pltp</i>	1.46
f_ctrl	MG2	<i>Ier5</i>	1.15	f_ctrl	MG5	<i>Mbp</i>	1.12
f_ctrl	MG2	<i>Zfp36</i>	1.04	f_ctrl	MG5	<i>Slc2a1</i>	1.06
f_ctrl	MG2	<i>Cited2</i>	0.91	f_ctrl	MG5	<i>Hspb1</i>	0.96
f_ctrl	MG2	<i>Klf6</i>	0.89	f_ctrl	MG5	<i>Slco1c1</i>	0.91
f_ctrl	MG2	<i>Ubc</i>	0.88	f_ctrl	MG5	<i>Gsn</i>	0.85
f_ctrl	MG2	<i>Rhob</i>	0.87	f_ctrl	MG5	<i>Cdkn1a</i>	0.80
f_ctrl	MG2	<i>Socs3</i>	0.86	f_ctrl	MG5	<i>Zbtb20</i>	0.79
f_ctrl	MG2	<i>Dnajb1</i>	0.85	f_ctrl	MG5	<i>Calm1</i>	0.77
f_ctrl	MG2	<i>Tsc22d3</i>	0.84	f_ctrl	MG5	<i>Ramp2</i>	0.77
f_ctrl	MG2	<i>Gm26532</i>	0.82	f_ctrl	MG5	<i>App</i>	0.76
f_ctrl	MG2	<i>Ppp1r15a</i>	0.79	f_ctrl	MG5	<i>Stmn1</i>	0.76
f_ctrl	MG2	<i>Gadd45g</i>	0.79	f_ctrl	MG5	<i>Rbms1</i>	0.73
f_ctrl	MG2	<i>Ccl4</i>	0.70	f_ctrl	MG5	<i>Ablim1</i>	0.73
f_ctrl	MG2	<i>H3f3b</i>	0.68	f_ctrl	MG5	<i>Sgms1</i>	0.72
f_ctrl	MG2	<i>Ptma</i>	0.63	f_ctrl	MG5	<i>Cnp</i>	0.69
f_ctrl	MG2	<i>Sertad1</i>	0.62	f_ctrl	MG5	<i>Selenow</i>	0.61
f_ctrl	MG2	<i>Clk1</i>	0.56	f_ctrl	MG5	<i>Selenom</i>	0.60
f_ctrl	MG2	<i>Sgk1</i>	0.55	f_ctrl	MG5	<i>Ywhaq</i>	0.60
f_ctrl	MG2	<i>Tob2</i>	0.54	f_ctrl	MG5	<i>Fez1</i>	0.58
f_ctrl	MG3	<i>Bmp2k</i>	1.31	f_ctrl	MG5	<i>Crip1</i>	0.56
f_ctrl	MG3	<i>Bhlhe41</i>	1.17	f_ctrl	MG5	<i>Kank3</i>	0.55
f_ctrl	MG3	<i>Slc39a1</i>	1.13	f_ctrl	MG5	<i>Gsta4</i>	0.55
f_ctrl	MG3	<i>Ncoa3</i>	1.04	f_ctrl	MG5	<i>Pecam1</i>	0.54
f_ctrl	MG3	<i>Notch2</i>	0.94	f_ctrl	MG5	<i>Cav2</i>	0.53
f_ctrl	MG3	<i>Zfp691</i>	0.94	f_ctrl	MG5	<i>Nsrp1</i>	0.48
f_ctrl	MG3	<i>Actb</i>	0.86	f_ctrl	MG5	<i>Twistnb</i>	0.47
f_ctrl	MG3	<i>Zscan26</i>	0.73	f_ctrl	MG5	<i>Bbc3</i>	0.46
f_ctrl	MG3	<i>Dpysl2</i>	0.73	f_ctrl	MG6	<i>Cd63</i>	1.13
f_ctrl	MG3	<i>Ptafr</i>	0.72	f_ctrl	MG6	<i>Gpr84</i>	0.89
f_ctrl	MG3	<i>Itpril1</i>	0.71	f_ctrl	MG6	<i>Ms4a6b</i>	0.79
f_ctrl	MG3	<i>Nfia</i>	0.71	f_ctrl	MG6	<i>Tmem119</i>	0.64
f_ctrl	MG3	<i>Cbx3</i>	0.69	f_ctrl	MG6	<i>Cd9</i>	0.64
f_ctrl	MG3	<i>Lrrc8a</i>	0.69	f_ctrl	MG6	<i>mt-Nd1</i>	0.63
f_ctrl	MG3	<i>Kdelr2</i>	0.68	f_ctrl	MG6	<i>Csf2ra</i>	0.58
f_ctrl	MG3	<i>Gm32036</i>	0.68	f_ctrl	MG6	<i>Cd79b</i>	0.58
f_ctrl	MG3	<i>Tmf1</i>	0.67	f_ctrl	MG6	<i>Lrrc8a</i>	0.55
f_ctrl	MG3	<i>C5ar2</i>	0.65	f_ctrl	MG6	<i>Ctsd</i>	0.54
f_ctrl	MG3	<i>Skil</i>	0.65	f_ctrl	MG6	<i>P2ry12</i>	0.53
f_ctrl	MG3	<i>Gnb1</i>	0.64	f_ctrl	MG6	<i>mt-Co3</i>	0.53

condition	cluster	Gene.name	avg_logFC
f_ctrl	MG6	<i>Lilra5</i>	0.47
f_ctrl	MG6	<i>Acvr11</i>	0.44
f_ctrl	MG6	<i>Hist1h2be</i>	0.44
f_ctrl	MG6	<i>Lat2</i>	0.43
f_ctrl	MG6	<i>Lgals3bp</i>	0.41
f_ctrl	MG6	<i>5031425E22Rik</i>	0.40
f_ctrl	MG6	<i>Usp15</i>	0.39
f_ctrl	MG6	<i>Nucb2</i>	0.39
f_ctrl	MG6	<i>Msmo1</i>	0.38
f_ctrl	MG6	<i>Gbp7</i>	0.38
f_ctrl	MG6	<i>Kcnn4</i>	0.38
f_ctrl	MG6	<i>Gcc2</i>	0.37
f_ctrl	MG6	<i>mt-Atp6</i>	0.37
f_ctrl	MG6	<i>Nfil3</i>	0.37
f_ctrl	MG6	<i>Pan3</i>	0.37
f_ctrl	MG6	<i>Rnase6</i>	0.35
f_ctrl	MG6	<i>Cst3</i>	0.34
f_ctrl	MG6	<i>AC160336.1</i>	0.33
f_ctrl	pre-MG	<i>Ccl12</i>	2.33
f_ctrl	pre-MG	<i>Ifit3</i>	1.99
f_ctrl	pre-MG	<i>Isg15</i>	1.61
f_ctrl	pre-MG	<i>Ccl4</i>	1.55
f_ctrl	pre-MG	<i>Lpl</i>	1.53
f_ctrl	pre-MG	<i>Ifit3b</i>	1.48
f_ctrl	pre-MG	<i>Ifitm3</i>	1.42
f_ctrl	pre-MG	<i>Rtp4</i>	1.35
f_ctrl	pre-MG	<i>Ccl3</i>	1.32
f_ctrl	pre-MG	<i>Lgals3</i>	1.15
f_ctrl	pre-MG	<i>Ifi2712a</i>	1.15
f_ctrl	pre-MG	<i>Bst2</i>	1.10
f_ctrl	pre-MG	<i>Cd63</i>	1.09
f_ctrl	pre-MG	<i>Ifi204</i>	1.08
f_ctrl	pre-MG	<i>Usp18</i>	1.06
f_ctrl	pre-MG	<i>Phf11d</i>	1.01
f_ctrl	pre-MG	<i>Irf7</i>	0.99
f_ctrl	pre-MG	<i>Ifit1</i>	0.98
f_ctrl	pre-MG	<i>Ifi206</i>	0.92
f_ctrl	pre-MG	<i>Slfn2</i>	0.91
f_ctrl	pre-MG	<i>Pkm</i>	0.85
f_ctrl	pre-MG	<i>Phf11b</i>	0.85
f_ctrl	pre-MG	<i>Ifit2</i>	0.83
f_ctrl	pre-MG	<i>Spp1</i>	0.81
f_ctrl	pre-MG	<i>Trim30a</i>	0.80
f_ctrl	pre-MG	<i>Tpi1</i>	0.79
f_ctrl	pre-MG	<i>Cd52</i>	0.78
f_ctrl	pre-MG	<i>Lgals3bp</i>	0.76
f_ctrl	pre-MG	<i>Id2</i>	0.76
f_ctrl	pre-MG	<i>Cst7</i>	0.75

female tumor							
condition	cluster	Gene.name	avg_logFC	condition	cluster	Gene.name	avg_logFC
f_tumor	MG1	<i>P2ry12</i>	1.18	f_tumor	MG7	<i>Ccl12</i>	1.36
f_tumor	MG1	<i>Fcrls</i>	1.01	f_tumor	MG7	<i>Gm4951</i>	0.72
f_tumor	MG1	<i>Tmem119</i>	0.79	f_tumor	MG7	<i>Lgals3bp</i>	0.65
f_tumor	MG1	<i>Sox4</i>	0.77	f_tumor	MG7	<i>Lag3</i>	0.63
f_tumor	MG1	<i>Bmp2k</i>	0.66	f_tumor	MG7	<i>Cd81</i>	0.61
f_tumor	MG1	<i>Bhlhe41</i>	0.65	f_tumor	MG7	<i>Ly86</i>	0.56
f_tumor	MG1	<i>Pros1</i>	0.65	f_tumor	MG7	<i>Crybb1</i>	0.55
f_tumor	MG1	<i>Syng1</i>	0.60	f_tumor	MG7	<i>H2-Oa</i>	0.49
f_tumor	MG1	<i>Ctsd</i>	0.60	f_tumor	MG7	<i>Cd180</i>	0.47
f_tumor	MG1	<i>Cd81</i>	0.58	f_tumor	MG7	<i>Serpine2</i>	0.45
f_tumor	MG1	<i>Fscn1</i>	0.56	f_tumor	MG7	<i>C4b</i>	0.44
f_tumor	MG1	<i>Crybb1</i>	0.53	f_tumor	MG7	<i>Timp2</i>	0.41
f_tumor	MG1	<i>Upk1b</i>	0.49	f_tumor	MG7	<i>Tmem119</i>	0.41
f_tumor	MG1	<i>Iji27</i>	0.48	f_tumor	MG7	<i>Ctsl</i>	0.40
f_tumor	MG1	<i>Sall1</i>	0.48	f_tumor	MG7	<i>Tor3a</i>	0.40
f_tumor	MG1	<i>Serpine2</i>	0.46	f_tumor	MG7	<i>Cd9</i>	0.39
f_tumor	MG1	<i>Serpinf1</i>	0.45	f_tumor	MG7	<i>Sdf211</i>	0.39
f_tumor	MG1	<i>Cd9</i>	0.44	f_tumor	MG7	<i>B2m</i>	0.38
f_tumor	MG1	<i>Adrb2</i>	0.42	f_tumor	MG7	<i>Ctsd</i>	0.36
f_tumor	MG1	<i>Rogdi</i>	0.41	f_tumor	MG7	<i>Cst7</i>	0.36
f_tumor	MG1	<i>Nfia</i>	0.41	f_tumor	MG7	<i>Bst2</i>	0.36
f_tumor	MG1	<i>Cadm1</i>	0.40	f_tumor	MG7	<i>Lap3</i>	0.34
f_tumor	MG1	<i>Ctsl</i>	0.37	f_tumor	MG7	<i>Spint1</i>	0.33
f_tumor	MG1	<i>Slc1a3</i>	0.37	f_tumor	MG7	<i>H2-D1</i>	0.33
f_tumor	MG1	<i>C5ar2</i>	0.35	f_tumor	MG7	<i>Gpr84</i>	0.33
f_tumor	MG1	<i>Zfp691</i>	0.34	f_tumor	MG7	<i>H2-DMa</i>	0.32
f_tumor	MG1	<i>Gusb</i>	0.31	f_tumor	MG7	<i>Ctsz</i>	0.30
f_tumor	MG1	<i>Cd34</i>	0.31	f_tumor	MG7	<i>H2-K1</i>	0.29
f_tumor	MG1	<i>Tmem176a</i>	0.30	f_tumor	MG7	<i>Cd34</i>	0.29
f_tumor	MG1	<i>Lag3</i>	0.30	f_tumor	MG7	<i>Hebp1</i>	0.27
f_tumor	MG2	<i>Jun</i>	1.98				
f_tumor	MG2	<i>Egr1</i>	1.59				
f_tumor	MG2	<i>Klf2</i>	1.55				
f_tumor	MG2	<i>Jund</i>	1.43				
f_tumor	MG2	<i>Ier2</i>	1.28				
f_tumor	MG2	<i>Btg2</i>	1.19				
f_tumor	MG2	<i>Rhob</i>	1.14				
f_tumor	MG2	<i>Ccl4</i>	1.13				
f_tumor	MG2	<i>Fos</i>	1.12				
f_tumor	MG2	<i>Dusp1</i>	1.10				
f_tumor	MG2	<i>Junb</i>	0.98				
f_tumor	MG2	<i>Cited2</i>	0.97				
f_tumor	MG2	<i>Ccl3</i>	0.95				
f_tumor	MG2	<i>Atf3</i>	0.95				
f_tumor	MG2	<i>Nfkbia</i>	0.95				
f_tumor	MG2	<i>Dnajb1</i>	0.83				
f_tumor	MG2	<i>Zfp36</i>	0.80				
f_tumor	MG2	<i>Klf6</i>	0.76				
f_tumor	MG2	<i>Cst7</i>	0.74				
f_tumor	MG2	<i>Tsc22d3</i>	0.69				
f_tumor	MG2	<i>Ppp1r15a</i>	0.68				
f_tumor	MG2	<i>Il1a</i>	0.66				
f_tumor	MG2	<i>Sgk1</i>	0.59				
f_tumor	MG2	<i>Gm26532</i>	0.55				
f_tumor	MG2	<i>Ctsl</i>	0.54				
f_tumor	MG2	<i>Cd9</i>	0.50				
f_tumor	MG2	<i>Gadd45g</i>	0.50				
f_tumor	MG2	<i>Icam1</i>	0.48				
f_tumor	MG2	<i>Ccl12</i>	0.46				
f_tumor	MG2	<i>Ctsd</i>	0.46				